Politecnico di Torino

ScuDo
Scuola di Dottorato ~ Doctoral School
WHAT YOU ARE, TAKES YOU FAR

Doctoral Dissertation
Doctoral Program in Energy Engineering (36^{th}cycle)

3D multi-physics modeling for the DC characterization of high-temperature superconducting Conductor-On-Round-Core cables

By

Sofia Viarengo

******

Supervisors:
Prof. Laura Savoldi, Supervisor
Prof. Fabio Freschi, Supervisor

Doctoral Examination Committee:
Prof. Naoyuki Amemiya, Referee, Kyoto University
Dr.ssa Francesca Cau, Referee, Fusion for Energy
Prof.ssa Luisa Chiesa, Tufts University
Dr.ssa Stefania Farinon, INFN Genova
Prof. Mohammad Yazdani-Asrami, University of Glasgow

Politecnico di Torino
2024

Declaration

I hereby declare that, the contents and organization of this dissertation constitute my own original work and does not compromise in any way the rights of third parties, including those relating to the security of personal data.

Sofia Viarengo
2024

* This dissertation is presented in partial fulfillment of the requirements for **Ph.D. degree** in the Graduate School of Politecnico di Torino (ScuDo).

To my family.

Acknowledgements

During this journey, I haven't been alone. This Ph.D. was only possible thanks to the research environment and the many great people I had chance to work with. This space is dedicated to them, for the important professional and human support I received from all of you.

I would like to start with my Ph.D. supervisor Professor Laura Savoldi. My guide and mentor who introduced me to the world of research and superconductivity. Since my Master studies, you had already discovered something about me that even I didn't know yet: your trust and continued motivation allowed me to grow personally and as an independent researcher. Thank you for granting me the opportunity to start a Ph.D. with you. A deep thanks to my Ph.D. supervisor Professor Fabio Freschi for the constant support and help, always accompanied by a bit of sarcasm giving some lightness even in the hardest moments. Your invaluable advice and your supervision have had a fundamental impact on my research and on the way I do research. It is no coincidence that you are in the world's top 2% of researchers.

An affectionate thank to all the MAHTEP Group: thank you for the joyful and stimulating environment in which we constantly work. Thank you for all the laughter, the jokes, the big discussions and the help that all of you gave me. Best luck for your Ph.D. works!

Especially, I want to thank Gianvito and Matteo for your human support in the most critical moment and the deep discussions. A special thanks to Rosa, with whom I started the Ph.D. journey. Colleague and close friends, so different, but so similar. Thank you for your strength and for your kindness, for your strong opinions and for your empathy. I wish you the best for the upcoming future!

Andrea, my problem-solver. I'm grateful to have met you from the beginning of this path: you guided me whenever I needed it and listened whenever I had doubts. Your constant and fundamental presence has made me learn, grow, and feel more confident in my career. Profoundly different, but complementary, related from a

strong and solid friendship. Simply, thank you for being there and continuing to be there.

My Californian period was a turning point in my carrier: I learned to make mistakes and to ask for help, which was never lacking. I thank Dr. Soren Prestemon to have given me the chance to spend almost the whole year at the LBNL. Thank you to Dr. Paolo Ferracin, my advisor at the LBNL, for your smiling presence and your motivation. Our meetings and discussions were crucial to consider the work and adjust the focus on the main objectives. I thank Dr. Lucas Brouwer for the helpful discussion about numerical modeling and for the constant support. Dr. Xiaorong Wang for sharing knowledge about CORC® cables and your availability for any clarification or discussion. I learned a lot from you all. I thank Dr. Christian Messe, my modeler mate, thanks to which "we no longer worked alone". The very long discussions in your office, our break walks on the sun or the beer in the evening made my work easier and lighter. I thank all the awesome people from the LBL: Jean-Francois, Rob, Geon, Phil, Reed, Liz, Claudia, Rob, Tengming, Chris, Laura, Mariusz, and Daniel. I deeply appreciate your warm welcome which made my staying more and more pleasant.

Some special words need to be dedicated to Josè Luis, not only a colleague, but a sincere friend. Thank you for being there since the first day, thank you for your laugh (especially about my bad luck), thank you for the long talks on the sun in front of the amazing view of the bay, thank you for never making me feel alone. Despite my bad luck, I feel thankful to have work with you, and I wish that our careers bring us close again. Best luck for everything!

Nico, cucciolo di Gin. How randomly did our interaction start? Behind two screens, miles and miles away from each other. Nonetheless, our work meetings became more frequent and more distracted. From numerical models and ideas, we start sharing thoughts and everyday life events. Our working harmony was suddenly transferred to our personal lives. Our first encounter was in Hawaii. Unforgettable trip. Thank you for all that I have learned from you, for involving me in crazy new experiences, and most importantly, for believing so deeply in me. I'm so grateful that our lives have intertwined workwise and beyond. I'm looking forward for doing great things with you! Finally, thank you for the important emotional and psychological support on a daily basis.

Fabrizio, my time abroad wouldn't have been the same without you. I deeply appreciate your spontaneity, your lightness, and your depth of soul. Thank you for

all the amazing trips, the laughter and the crying, for the White Horse, the burritos, the walks in San Francisco and for singing at the top of your lungs in the car. Useless to say that our experiences made that period memorable. I thank also all our friends who were part of it. My most sincere thanks for being my support in the most difficult moments.
Tizzo e Fala, with whom we shared the same journey. Thank you for our friendship, for all the funny Turin night, for the music, for the dinners and for the symbiotic life led during covid. I couldn't ask more than friends as you two are.
Lollino e Pingue, thank you for always being on my side, for the long road trips singing our favorite music, and for listening to all my dramas.
Bobbi, voice of my conscience. Thank you for understanding my distractions and for being there for me in all circumstances.
Elsu, you're my person. Thank you for your enthralling energy, for your optimism and for the fundamental emotional support.
Gioggi, my first friend ever. Thank you for always being with me and for your unconditional friendship.
Luca, who stands by my side. Thank you for your patience, for supporting the vivacity and passion that characterize my person. Thank you for listening to me, advising me, and making my life happier.
Finally, to my family, my mum, my dad, and my brother. Thank you for your support, your trust and for continuously believing in me, transmitting to me the strength and determination that made me the person I am today.

Abstract

High-Temperature Superconductors (HTS) can be the game changers in the next magnet generation for nuclear fusion and particle accelerators. They could also enable further improvements in cancer treatment devices and in technologies for future means of transportation and lossless power transmission. In perspective of $20+$ T field magnets (impossible target for the low-temperature superconductor counterparts) and more compact layouts for fusion reactors, which can make them marketable, the HTS are the alternative which can allow high transport current at very high field, guaranteeing at the same time a higher stability. Among them, the Rare-Earth Barium Copper Oxide (ReBCO) coated conductors seem to be a very promising option due to their high critical temperature and the extremely high critical current density. They are flat ceramic multilayer materials in which a $1-2$ μm of superconducting layer is coated by a copper stabilizer and mechanically supported by a metal substrate. Combining the high mechanical strength of the substrate, to withstand axial tensile stress, and the elasticity of ReBCO layer, to resist to compressive strain, the Conductor-on-Round-Core (CORC®) cable conductor has been introduced in 2009. It is composed of multiple tapes wounded in layers alternatively clockwise and counterclockwise around a central copper core. It is the only round conductor made of flat HTS tape: this solution guarantees a higher mechanical and electrical isotropy. High-performance cables are essential for a correct operation of magnets, safe operating conditions and high field quality. The critical current I_c, the maximum current which can be transported without transitioning to the normal state, is a key indicator of the cable/coil performances. I_c is strongly affected by production process and operating conditions: deformation, temperature, and magnetic field. The characterization of CORC® mostly occurs with dedicated experimental campaigns, but sufficient data are still missing. Development of ad-hoc numerical models should proceed in parallel to reproduce and, in perspective, predict the cable behavior. Here, a novel full-3D finite-element numerical multiphysics thermal and electromagnetic

model for CORC® -like conductors is presented, aiming at the characterization of the critical current. The model is implemented in COMSOL Multiphysics®. The I_c strain degradation, due to winding and bending, has been accounted with a simplified evaluation of the strain map, based on pure geometrical assumptions and from data available in the literature. The thermal model accounts for Joule losses (if any), conduction among overlapping tapes and an active convective cooling of the fluid, and it is coupled to the electromagnetic module. The electromagnetic model is based on the $T-A$ formulation: leveraging on the high aspect ratio of the thin ReBCO tapes, the superconducting domain is assumed as a thin shell. The current distribution among tapes and layers is guaranteed by using a set of self-consistent boundary conditions adopted for the first time in this kind of simulations. The new boundary conditions allow current re-distribution if any thermal or magnetic perturbation suddenly happens in a tape. The model is verified and benchmarked against other well-established formulations on a set of test cases. Starting from a tape model, the validation has been extended to simplified cases ($2-$tapes $1-$layer CORC®) to more complex geometries ($6-$tapes $3-$layers CORC® , straight and bended, and $12-$tapes $6-$layers CORC®). This work has been carried out in collaboration with the Lawrence Berkeley National Laboratory (LBNL), which provided test and data for the validation. The comparison of the computed $V-I$ curve of cables with available experimental data shows that the main physics features of the cable are well captured by the model, including performance degradation due to cable tapering at the terminations, and sets starting points for further improvements for the numerical model and the cable design.

Keyworks: High-temperature superconductors, hybrid formulation, CORC® cables, ReBCO tapes, critical current, numerical models, multiphysics.

Sommario

I superconduttori ad alta temperatura (HTS) rappresentano un possibile fattore di svolta per la prossima generazione di magneti per lo sviluppo di tecnologie come reattori a fusione nucleare e acceleratori di particelle, nonchè nel miglioramento di dispositivi medici per il trattamento del cancro, dei futuri mezzi di trasporto e della trasmissione di potenza elettrica senza perdite. Nella prospettiva di costruire magneti a $20+$ T, limite irraggiunbile dai superconduttori a bassa temperatura, e reattori a fusione più compatti, tanto da poterli rendere commercializzabili, gli HTS sono l'alternativa che permette di avere un'alta corrente di trasporto a campi molto elevati, garantendo allo stesso tempo un'elevata stabilità termica. I nastri conduttivi a base di terre rare, Rare-Earth Barium Copper Oxide (ReBCO), risultano tra le opzioni più promettenti, grazie alla loro alta temperatura critica e densità di corrente critica. I ReBCO sono dei sottili materiali ceramici, in cui lo strato superconduttivo di $1-2$ μm è ricoperto dallo stabilizzatore in rame e supportato meccanicamente da un substrato di metallo. Combinando la durezza del substrato, in grado di resistere agli sforzi assiali, e l'elasticità del ReBCO , resistente alla compressione, nel 2009 è stato introdotto il design di cavo chiamato Conductor-on-Round-Core (CORC®). Il cavo è costituito da più nastri di ReBCO avvolti intorno ad un stabilizzatore centrale di rame, cambiando alternativamente la direzione di avvolgimento. È l'unico cavo di forma circolare composto da nastri HTS, che consente una migliore isotropia meccanica ed elettrica. I cavi ad alte prestazioni sono essenziali per il corretto funzionamento dei magneti, per operare in sicurezza e per avere una buona qualità di campo. La corrente critica I_c, che è la corrente massima trasportabile da un superconduttore prima che transisca allo stato normale, è un indicatore chiave delle prestazioni di cavi e di bobine. La I_c si degrada fortemente a causa del processo di produzione e delle condizioni operative come lo stato di deformazione, la temperatura ed il campo magnetico. La caratterizzazione dei CORC® avviene principalmente attraverso campagne sperimentali, ma in letteratura c'è ancora una carenza di questi dati. Lo

sviluppo di modelli numerici, sviluppati ad-hoc, dovrebbe procedere in parallelo per riprodurre e, in prospettiva, predire il comportamento del cavo. In questo lavoro di tesi è presentato un modello numerico multifisico ad elementi finiti per i conduttori di tipo CORC® per la caratterizzazione della corrente critica. Il modello è sviluppato in COMSOL Multiphysics®. La degradazione della I_c dovuta all'avvolgimento intorno allo stabilizzatore e alla curvatura, nel caso in cui il cavo sia piegato, è tenuta in conto attraverso una valutazione semplificata della deformazione basata su pure assunzioni geometriche e di dati disponibili in letteratura. Il modello termico tiene conto delle perdite per effetto Joule (se presenti), della conduzione tra nastri sovrapposti e della convezione naturale del fluido. Inoltre, è accoppiato con il modello elettromagnetico. Quest'ultimo è basato sulla formulazione $T-A$: sfruttando l'alto rapporto d'aspetto del nastro ReBCO , il dominio superconduttivo è assunto come guscio sottile. La distribuzione di corrente tra i nastri e gli strati del cavo è garantita attraverso l'implementazione di una condizione al contorno autoconsistente, adottata per la prima volta in questo tipo di simulazioni. La nuova condizione al contorno permette la ridistribuzione di corrente in caso di un'improvvisa perturbazione termica o magnetica in uno dei nastri. Il modello è verificato con altre formulazioni, ben consolidate in letteratura, in diversi casi-studio. Partendo da un modello del singolo tape, la validazione è stata estesa da casi più semplificati di CORC® ($2-$tapes $1-$layer) a geometrie più complesse ($6-$tapes $3-$layers CORC® , dritto e piegato, e $12-$tapes $6-$layers CORC®). Questa attività è stata condotta in collaborazione con il Lawrence Berkeley National Laboratory (LBNL), che ha fornito i dati dei test per la validazione. Il confronto tra le curve tensione-corrente con i dati disponibili ha dimostrato che le principali caratteristiche fisiche del cavo sono ben rappresentate dal modello, inclusa la degradazione che avviene nelle terminazioni (dove i tape si aprono e si allontano dallo stabilizzatore), fissando inoltre dei punti di partenza per ulteriori miglioramenti, non solo del modello numerico, ma anche per il design del cavo.

Parole-chiave: Superconduttori ad alta temperatura, formulazioni ibride, cavi CORC® , nastri di ReBCO , corrente critica, multifisica.

Contents

Nomenclature

Roman Symbols

ΔL	Elongation
$\dot{q}$	Heat source
A	Cross section
A	Magnetic vector potential
app	Applied
B	Magnetic flux density
b	Fitting parameter J_c scaling law (3.30)
B_0	Fitting parameter J_c scaling law (3.29)
B_c	Fitting parameter J_c scaling law (3.30)
C_p	Specific heat at constant pressure
D	Electric flux density
d	Diameter
g	Gravity acceleration
H	Magnetic field
h	Heat transfer coefficient
I	Electric current

J	Current density
J_e	Engineering critical current density
J_{c0}	Critical current density at 0 K and 0 T
k	Fitting parameter J_c scaling law (3.30)
L	Length
L_0	Initial length
L_c	Characteristic length
m	Fitting parameter J_c scaling law (3.29)
n	Normal versor
p	Fitting parameter J_c scaling law (3.31)
R	Cylindrical R-coordinate
r_b	Bending radius
S	Surface
sub	Substrate
T	Current vector potential
t	Time
th	Thickenss
V	Voltage
V_t	Total volume of the tape
w	Tape width
x	Cartesian x-coordinate
y	Cartesian y-coordinate
z	Cartesian z-coordinate

Greek Symbols

α	Winding angle
α_f	Thermal diffusivity
$\bar{\theta}$	Average temperature
β	Fitting parameter J_c scaling law (3.31)
β_f	Volumetric thermal expansion coefficient
χ_ω	Anisotropy angular factor
δ	Distance between to adiacent CORC® layers
γ	Electron mass anisotropy
λ	Thermal conductivity
μ	Magnetic permeability
μ_0	Vacuum permeability
ν	Dynamic viscosity
ω	Angle between the magnetic field and the tape surface
ϕ	Magnetic scalar potential
ψ	Critical current degradation due to strain
ρ	Mass density
ρ_c	Electric charge density
σ	Electric conducivity
θ	Temperature
θ^*	Characteristic temperature related to pinning forces for J_c scaling law (3.35)
θ_∞	Enviromental temperature
ε	Strain

Superscripts

N	Power law exponent
s	Characteristic exponent for J_c scaling law (3.34)

Subscripts

$\perp$	Perpendicular component
abs	Absolute value
ave	Average
b	Bending
c	Critical
core	Central core
cu	Copper
curve	Bended cable
eq	Equivalent
ext	External
f	Fluid
fin	Final
i	i-th layer
in	Innermost
init	Initial
j	j-th CORC® layer
l	Layer
main	Main cable
min	Minimum

op Operating condition

out Outermost

$pitch$ Twist pitch of the cable

s Shrinkage

str Straight cable

$term$ Terminations

tot Total

w Tape width

wet Wetted

Other Symbols

$\nabla\cdot$ Divergence

$\nabla\times$ Curl

∇ Gradient

∂ Partial derivative

Acronyms / Abbreviations

CORC® Conductor-On-Round-Core

ABAD Alternating Beam Assisted Deposition

AC Alternating current

ACT Advanced Conductor Technologies

BRAST Braided Stacks of Tapes

BSCCO Bismuth strontium calcium copper oxide

CCT Canted-Cosine Theta

CICC Cable-in-Conduit-Conductors

CroCo Cross conductor

DC Direct current

DEMO DEMOnstration Fusion Power Reactor

DoFs Degree of Freedom

ENEA Ente per le nuove tecnologie, l'energia e l'ambiente

H4C Cryogenic Circuit Conductor and Coil for High temperature SC

HTS High Temperature Superconductors

IBAD Ion Beam Assisted Deposition

ISD Inclined Surface Deposition

ITER International Thermonuclear Experimental Reactor

JackPot Jacket Potential

KIT Karlsruhe Institute of Technology

LBNL Lawrence Berkeley National Laboratory

LTS Low Temperature Superconductors

MIT Massachusetts Institute of Technology

MOCVD Metal Organic Chemical Vapor Deposition

MOD Metal Organic Deposition

MQS Magnetp Quasi-static

NHMFL National High Magnetic Field Laboratory

NIFS National Institute for Fusion Science

OPENSC^2 OPEN Super Conducting Cables

PDE Partial Derivatives Equations

PDL Pulsed Laser Decomposition

RABiTS Rolling Assisted Biaxially Textured Substrate

RCE Reactive Co-Evaporation

ReBCO Rare-Earth Bario Copper Oxide

SC Superconductor

STARS Stacked Tapes Assembled in Rigid Structure

THEA Thermal Hydraulic and Electric Analysis

THELMA Thermal-Hydraulic ELectro-MAgnetic

TSTC Twisted Stacked-Tape Cable

VIPER Vacuum pressure impregnated, insulated, partially transposed, extruded, and roll-formed

Chapter 1

Introduction

This thesis concerns the development and the validation of a multiphysics numerical model for the characterization of the critical current of high temperature superconducting based on Rare-Earth Barium Copper Oxide (ReBCO) coated conductors arranged in Conductor-on-Round-Core (CORC®) conductors. The electromagnetic model is coupled to a thermal module to reproduce, and in perspective, predict the cable performance under different operating conditions. This chapter gives a background and context regarding the materials and cables treated in this research activity, starting from a brief introduction on superconductivity, with particular focus to high temperature superconducting materials and possible cable configurations, along with the scope, the structure and the outline of the thesis. Portions of the present chapter were already published in the following scientific papers:

- S. Viarengo, F. Freschi, D. Placido and L. Savoldi, "Current Distribution Modeling in the Open-Source OPENSC2 Tool for the Multi-Physics Analysis of HTS and LTS Cables," in IEEE Transactions on Applied Superconductivity, vol. 32, no. 6, pp. 1-5, Sept. 2022, Art no. 4802405, doi: 10.1109/TASC.2022.3158309, [1];
- S. Viarengo, L. Brouwer, P. Ferracin, F. Freschi, N.Riva, L. Savoldi, X. Wang, "A New Coupled Electrodynamic T – A and Thermal Model for the Critical Current Characterization of High-Temperature Superconducting Tapes and Cables," in IEEE Access, vol. 11, pp. 107548-107561, 2023, doi: 10.1109/ACCESS.2023.3321194, [2].

1.1 Superconductivity

Superconductivity is a combination of electric and magnetic properties observed for the first time in 1911 by Kamerlingh Onnes [3]. Those materials show a sharp transition to zero electrical resistivity when they are cooled below a critical temperature. The zero-resistance means that there is no voltage drop along the material when a current is flowing through it, and no power loss in direct current. That properties make superconductors highly relevant for high-current or high-field applications, and the only option in some cases (e.g., fusion technologies [4]). Superconductors (SC) also experiences the so-called Meissner–Ochsenfeld effect [5], the complete expulsion of the magnetic flux acting as a perfect diamagnetic when in the superconducting state. The superconducting state is maintained according three quantities: carried current density, magnetic field and temperature, which are strongly correlated and together define the critical surface, see Fig. 1.1. The difference among the Type-I and Type-II is due to the magnetic behaviour to an external magnetic field B_{ext} [6]. The superconductors Type-I lose the Meissner effect when $B_{ext} < B_c$ (where B_c is the critical field), while Type-II a mixed phase for $B_{c1} < B_{ext} < B_{c2}$. In that region, the material is still in the superconductive state with the co-existence of some resistive regions. The superconductivity is completely lost for $B_{ext} > B_{c2}$. In real application, superconductors Type-II are the most used mainly for two reasons:

- $B_{c2} > B_c$ of a Type-I superconductor;
- when under superconducting state (thus Meissner effect exists, $B = 0$), Type-I superconductors can't carry any current (since $\nabla \times B = \mu_0 I$).

Superconductors can still be categorized in Low Temperature Superconductors (LTS) and High Temperature Superconductors (HTS), depending on a critical temperature respectively lower or higher than 30 K [7]. Superconducting wires, cables, and tapes have some practical applications mostly in energy and research field (as magnets for particle accelerators, superconducting fault current limiters, power transmission, permanent magnets, electric motors, nuclear fusion), but also for the health care devices as the ones for cancer treatment. The most common superconductors are reported Table 1.1. in along with they properties and characterization.

Table 1.1 Key properties of the most common used LTS and HTS materials [8, 9] (Iron-based superconductors are not reported here).

Type	Material	$T_c(0\,T, 0\,A)$ K	B_c or $B_{c2}(0\,T, 0\,A)$ T	Characteristic
I	Al	1.2	0.01	Ductile
	Pb	7.2	0.08	Ductile
II-LTS	NbTi	9.3	14.6	Ductile
	Nb_3Sn	18.3	24-28	Brittle
II-HTS	MgB_2	39	16	Brittle
	ReBCO	93	>100	Brittle
	Bi2212	85	>100	Brittle
	Bi2223	110	>100	Brittle

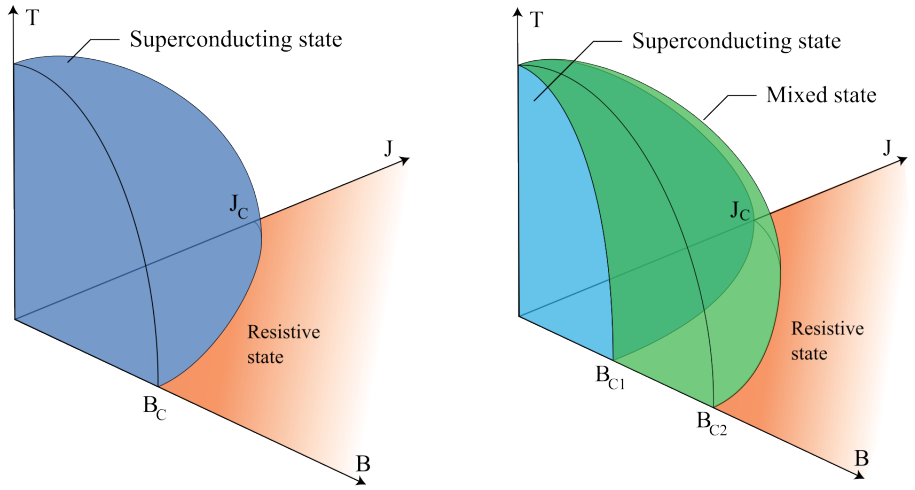

(a) (b)

Fig. 1.1 The critical surface of (a) type-I superconductors, delimiting the superconducting and normal states, and of (b) type-II superconductors, delimiting the superconducting, mixed and normal states.

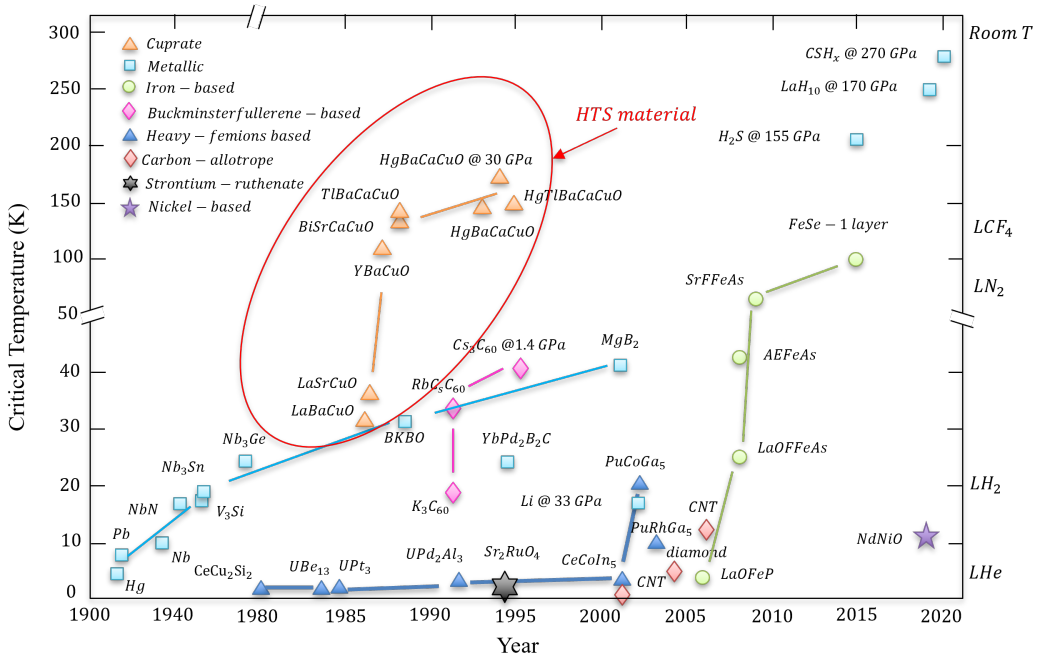

Fig. 1.2 Superconductors discovers timeline (adapted from [11]).

1.2 High-Temperature Superconductor for large magnet system

The HTS, first discovered in 1986 [7] (see Fig. 1.2), constitute the most viable option towards the development of high field magnets satisfying the requirements of high operating currents, high current densities, and compact coil layouts [10]. One of the biggest advantage of HTS is that they can work at higher temperature than LTS materials: often, they have a critical temperature T_c higher than 77 K, so they can be cooled with liquid nitrogen or helium gas. They also have excellent performances at low temperature reaching very high fields [12]. At low temperature, from 4.2 K to 20 K, they can generate magnetic flux density up to 20 T and above, demonstrated at the National High Magnetic Field Laboratory (NHMFL) of Tallahassee with a 32 T/34 mm bore hybrid LTS/HTS solenoid [13], an impossible target for just LTS-based magnets [14], see Table 1.1. In addition, HTS materials have a higher electric and thermal stability than LTS [15]. Operating at low temperature, e.g. 5 K, allows them to work closer to J_c with a high temperature margin. That also means that a higher accumulation of energy is required to reach an abrupt transition from superconducting to normal state (so-called "quench"). If the HTS quenchs,

the propagation of the high temperature (normal) zone and the voltage arise have a very low speed. When the quench will be detected based on that signal, the hot-spot temperature can already exceed the maximum allowed value. Due to the high thermal stability, the storage energy may reach many GJ, need to be dumped in the cold-mass of the magnet. A proper amount of stabilizing material (e.g., copper, aluminum, silver) increases the heat capacity and the thermal conductivity of the magnet/cable and it can help in preventing such situations. HTS materials have also a strongly anisotropic crystal structure (the unit cell is composed of parallel atomic ab planes, the c-axis is the direction perpendicular to ab [16], see Fig. 2.1) with a consequent high dependence of the critical current density J_c on the angle orientation of the magnetic field B. For a given magnetic field, the lowest value of J_c is typically at when B is normal to the ab plane (along the c-axis), see Fig. 2.4. Differently from LTS, they are mostly ceramic and brittle materials: manufacture can be more complicated and expensive. At present, three cuprate materials are considered suitable for large scale applications: two bismuth strontium calcium copper oxide compounds [17], $Bi_2Sr_2CaCu_2O_{8+x}$ (Bi2212) and $Bi_2Sr_2Ca_2Cu_3O_{10+x}$ (Bi2223) , and a rare-earth barium copper oxide compound [18], $ReBa_2Cu_3O_{7-x}$ (ReBCO), where Re stands for Rare Earth, typically yttrium (Y) or gadolinium (Gd). Bi2212 are made similarly to LTS in isotropic multifilamentary round wire, see Fig. 1.3a. The superconducting filaments, ≈ 15 μm diameter, are embedded in a silver matrix and a heat treatment at very high pressure can significantly increase the performance of the cable, the J_c, [12]. Bi2223 an d ReBCO are both available in thin flat tapes with $1-2$ μm of superconducting layer coated by a metallic substrate via chemical deposition [16], see Fig. 1.3b and Fig. 1.3c. We will mostly focus on ReBCO material in section 2.1.

1.3 Coated conductor cables

In real applications, ReBCO tapes are combined together in HTS cables to build large scale magnets. Moreover, the anisotropy of ReBCO properties implies the angular anisotropy of the critical current is an additional complexity to the design of cable and magnets. The thin flat geometry of ReBCO adds some difficulties in achieving isotropic properties for cables: conventionally, round wire geometry are preferred in cabling, and that requires new design and layouts. Three main concepts, see Fig. 1.4,

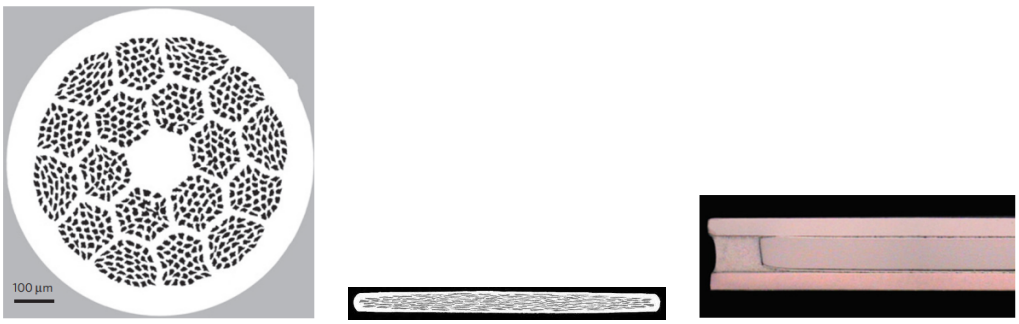

(a) (b) (c)

Fig. 1.3 HTS material cross sections: (a) Bi2212, reproduced from [12]. All Rights Reserved. (b) Bi2223, reproduced from [19] (c) ReBCO cross section, reproduced from [20]. All Rights Reserved.

have been developed for manufacturing ReBCO cable to enhance properties and stability of the single tape: Twisted Stacked-Tape Cable (TSTC) [21], Roebel Cable [22] and Conductor-on-Round-Core (CORC®) Cable [23].

1.3.1 Twisted Stacked-Tape Cable

The twisted stacked-tape conductor was proposed at (MIT) in 2011 [21], as main application the power transmission. In this concept, tapes are stacked along the c-axis, to increase the critical current, and is twisted along their longitudinal axis, eventually to reduce the losses, see Fig. 1.5. The minimum twist pitch is limited to the stack degradation due to strain, since twisting a stack of tapes is equivalent to twist of a single tape: there's no gain in flexibility, therefore relatively long pitches are required ($>$ 100 mm [21]). Nonetheless, since AC losses are depending on the magnetic field orientation to the wide side of the tape [24], the twisting reduces the losses by averaging the local magnetic on the cross section. This shape is also beneficial for self-field and coupling losses, effectively reducing eddy current losses and inductive currents [21]. The absence of former materials allows a high critical current density [25]. For those reasons, high-current conductors DC applications, low frequency high field magnets and power transmission cables are the most suitable applications [21]. Nonetheless, this configuration leads to different cable layouts inserting the stack of tapes in grooves of a stabilizer core (usually made of aluminum or copper), which increases the resilience and the robustness [25] and makes them suitable for

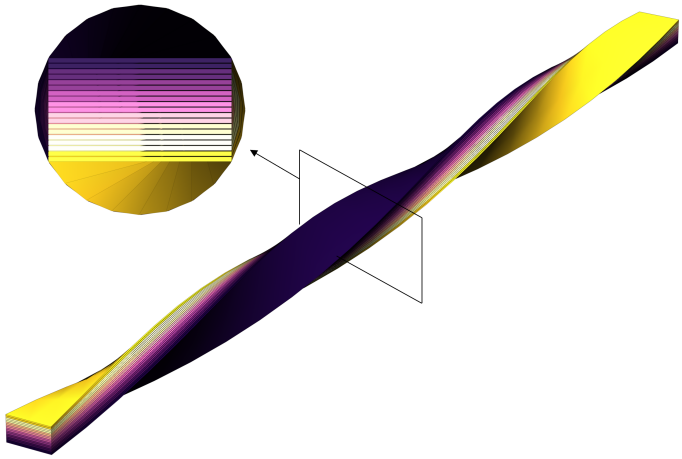

(a)

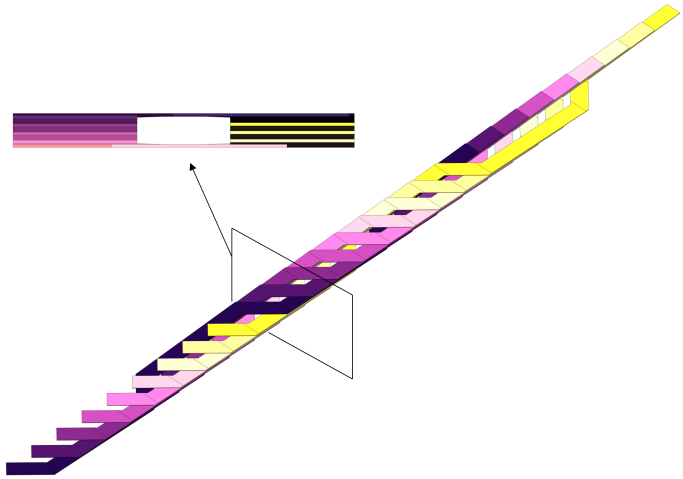

(b)

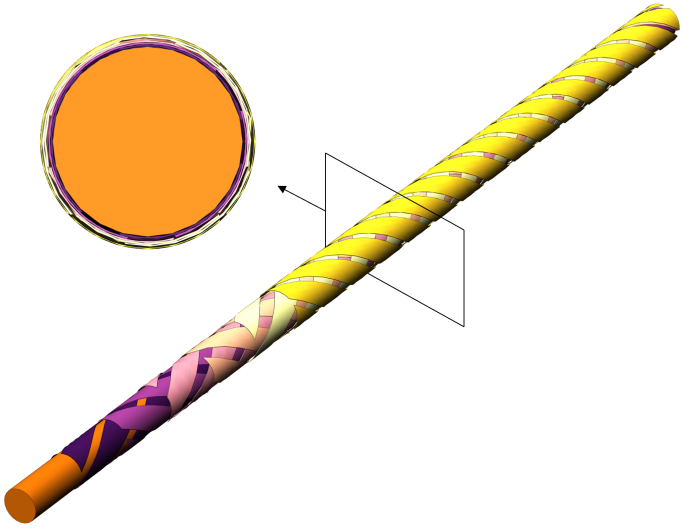

(c)

Fig. 1.4 Illustration of the three main HTS cable design: (a) Twisted stacked-tape cable; (b) Roebel cable; (c) Conductor-on-Round-Core cable.

Fig. 1.5 Picture of twisted stack of ReBCO tapes. ®2013 IEEE. Reprinted, with permission, from [26].

high-field and high-current magnets for fusion reactors. Different conductors have been designed based on TSTC principle:

- the ENEA twisted-stack slotted-core conductor [27] and its further improvement BRaided Stack of Tapes (BRAST) cable [28];
- the soldered stack in a copper profile at Swiss Plasma Center [29];
- the HTS Stacked Tapes Assembled in Rigid Structure (STARS) conductor from National Institute for Fusion Science (NIFS) [30];
- the cross-conductor (CroCo) concept from Karlsruhe Institute of Technology (KIT) [31];
- the quasi-isotropic strand at North China Electric Power University [32];
- the Vacuum Pressure Impregnated, insulated, partially transposed, Extruded, and Roll-formed (VIPER) VIPER cable from MIT [33].

1.3.2 Roebel Cable

The Roebel cable concept was born from the necessity of the reduction of the AC losses for electric power generator applications [34] and the first ReBCO Roebel cable was built in KIT [35]. ReBCO tapes are arrange in a meandering shape, see Fig. 1.6a, achieved by cutting out undesired region for a 12 mm width tape, see Fig. 1.6b. The full transposition of the tapes allows a homogeneous current distribution and improved and an alignment of the c-axis along the conductor [36]. Consequently, it is possible to achieved almost perfect alignment with the magnetic field to enhance the conductor's in-field performance: this layout has been

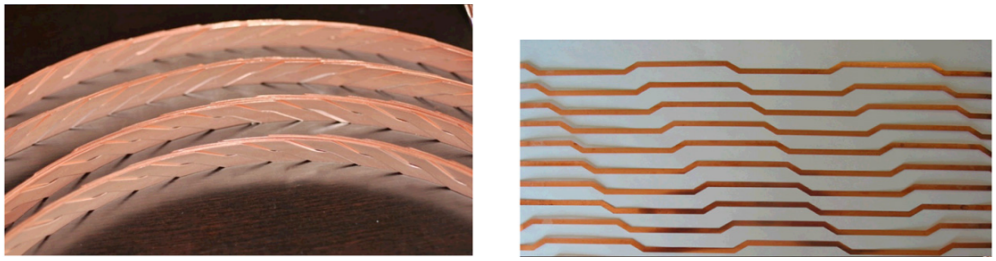

(a) (b)

Fig. 1.6 ReBCO Roebel cable: (a) after and (b) before cable assembly. ®2007 IEEE. Reprinted, with permission, from [22].

implemented for designing HTS accelerator magnet [37]. The transposition allows the reduction of the AC losses by exposing each tapes to similar magnetic field, minimizing hysteresis and coupling losses. As a drawback, the bending in the hard direction is more complex and the stress tends to concentrate due to the crossovers along the cable [25].

1.3.3 Conductor-on-Round-Core Cable

The concept of CORC® cable was introduced by Danko Van der Laan in 2009 [38] and it's the main focus of the thesis, to which section 2.2 is devoted. It is composed of several layers of HTS tapes helically wounded on a copper core with opposite winding direction for each layer and they are commercially available from Advanced Conductor Technologies (ACT). This cabling guarantees a high isotropic flexibility and mechanical strength [39], and reduction of AC losses [40, 41]. The helical pattern allows the minimization of the perpendicular component of the magnetic field, reducing the AC losses, nonetheless some losses occur due to magnetic field components along the tape width. The core diameter is typically in the order of few millimeters and the winding angle against the cable cross section is around 40 degrees. Nonetheless, the high superconductor to stabilizer ratio, due to the copper core, results in a lower current density with respect Roebel and TSTC cable. Even though no part of the tapes is cut away, as in Roebel, the CORC® uses the 30% more of HTS material then the TSTC due to the spiraling, [9]. The CORC® -like conductors, see Fig. 1.7, are divided in:

- CORC® wire: characterized by a inner diameter lower than 4 mm [42, 39], tipically no more than 30 tapes. The wire is more flexible and allows smaller

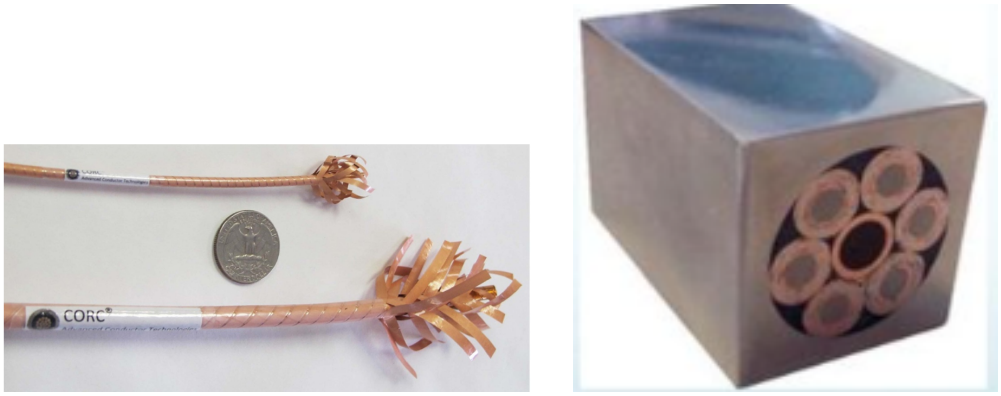

(a) (b)

Fig. 1.7 (a) Picture of CORC® wire (on the top) and CORC® cable (on the bottom), reproduced from [45]. All Rights Reserved. (b) Picture of a CORC® CICC, reproduced from [46].

bending radii (> 50 mm), applicable for particle accelerator applications [43]. The CORC® wire uses a 2 mm width tape with a thickness of ≈ 45 μm, and they can reach a current density of ≈ 300 A/mm^2 at 4.2 K and 20 T.

- CORC® cable: characterized by a inner diameter in the range of 4 and 8 mm, realized with tapes of 4 mm width, [42], usually no more than 50 tapes. The low current density of the standalone cable makes them suitable for power transmission applications (≈ 150 A/mm^2 at 4.2 K).
- CORC® Cable-In-Conduit-Conductors: CORC® cables or wires can be arranged in a bundle encapsulated in a metal jacket [44]. They can have a bending radius about 1 m.The design critical current is 100 kA at 4.5 K and 10 T specifically intended to be used for high-current bus-bars for fusion applications and large detector-type magnets.

1.4 Numerical models for ReBCO conductors

Over the last decades, several tools have been implemented for describing the electromagnetic and thermal behaviour of the well-established LTS technology. The THEA code [47] is characterized by a set of semi-continuum circuital equations both for LTS and HTS, however, thermal-hydraulic models such as [48, 49] are not always suitable for HTS stacked conductors due to the high Biot Number of the

stacks, which can result in an average strand temperature as computed by THEA not representative of the actual hot spot temperature within the stack during fast transients [50]. The THELMA code [51] exploits a distributed parameter circuital approach for LTS, while the 4C code [52] foresees a simple lumped parameter model based on current partition between SC and stabilizer. The JackPot software [53] is structured as an electrical network of SC elements and resistors, including the interaction between strands through contact resistance and the connection with the joints. More recently, the H4C code [54] has been developed for HTS cables based on a distributed parameter model and a weak coupling with the thermal-hydraulic model. Similarly to THEA and THELMA, an integral formulation of the quasi-static approximation of Maxwell's equations is adopted in the electric model [1] of *OPENSC*^{2} [55], meant to be applicable for both LTS and HTS components. The mathematical model is based on lumped element equivalent circuit that considers the interactions between the current carrying elements through longitudinal electrical resistances, self and mutual inductances and transverse conductances between the different strands or tapes, according to the cable layout.

The time constants and characteristic lengths characterizing the development of the main physical phenomena occurring in HTS tapes, stacks, conductors and magnets are typically derived and compared to those typical of LTS wires, cables and coils. Regarding the BSCCO, some of those tools can relatively adapted according to some scaling law and adding current sharing where is not present. However, there are differences related to the different and strongly anisotropic material properties, to the thin shape of tape, and to wire or conductor architecture of ReBCO coated conductors. The differences in time constants and length scales between LTS and HTS conductors refer to both the development of solely electromagnetic or thermal transients and to the evolution of coupled thermal – electrical phenomena, such as quench. Furthermore, the peculiar mechanical properties of the anisotropic HTS tapes require a different approach in dealing with the limit stresses inside superconducting magnets, which in several cases represent the main limitation to the maximum reachable magnetic field. Some new paradigms are emerging for HTS magnets: new cable configurations and cooling systems, higher operating temperature ($\geq$ 20 K), thus higher energy efficiency, higher heat capacity of solids and lower cryogen inventory.

ReBCO tapes exhibit different magnetization current pattern with respect to LTS wires. In LTS wires, filaments magnetization currents in filament coupling $3-50$ mm.

In II generation HTS tapes, the currents flow over the whole tape width. While, the current transfer between HTS tapes in a cable or coil normally occurs over lengths and times longer than between strands of LTS cables. Measured contact resistances between HTS tapes span over many orders of magnitude (depending on the application). Therefore, there are new challenges and different behaviour which required new methods and numerical tools to properly describe HTS components [56]. The development of first numerical models for HTS began since the 1990s. Initially, they were focused on understanding the basic electromagnetic properties of HTS materials, as magnetization and field penetration[57], critical state [58], flux pinning [59], and critical currents [60]. More sophisticated models where exploited to simulate AC losses [61], magnetic field distributions [62, 63], and the behavior of HTS tapes and wires in practical applications. Progress in Finite Element Modeling (FEM) techniques allowed more detailed simulations of whole HTS devices: model start to be comprehensive of the anisotropic properties of HTS materials and coupling the effects of multiple physics (thermal conduction, electromagnetism, mechanics). In literature, there are 2D transient tools which help in maintaining low computational cost and memory occupation, for AC losses computation [64–66], magnetization losses [67, 68] and for simplified quench simulation [69]. Most of the quench analysis are three-dimensional simulation [70–72], but to deal with the high computational time, lately a simplified 1D electric model coupled to a lumped thermal model has been developed [73]. Few 3D models are present in literature which consider the ReBCO surface [37, 74–77]. As regards tools devoted to the evaluation and prediction of critical current, there are simplified 2D self-consistent steady state models, [78, 79], but the twisting of the cable, which may also affect the I_c, is not considered.

1.5 Scope of the thesis

The CORC® cable is gaining interested for the development of next future colliders, which are targeting to 20 T field [14]. Moreover, arranged in Cable-in-Conduit Conductor (CICC), they can possibly be used for fusion and detector magnet application [80]. Dedicated experimental characterization of the critical current I_c is necessary to quantify, firstly the quality of the cable, and then the degradation due to the winding process and operating conditions. The development of reliable numerical models

capable to reproduce and predict the cable performances should proceed in parallel along with testing. The determination of critical current under self-field conditions is employed to evaluate the quality of the superconducting material itself, which may undergo various technological processes altering the wire's overall structure [81]. In such assessments, it is initially assumed that the critical current density can be obtained by simply dividing the measured critical current by the cross-sectional area. However, the critical current density is depending on the magnetic field, and its orientation along the tape, and temperature [82]. The self-field generated is not uniform along the cross section with a consequent non-uniformity of the transport current, and therefore of the I_c, along the tape cross section, see Fig. 1.8. The magnetic field penetrates from the edges of the conductor, see Fig. 1.8 (a),(c),(e), where also the current density is larger, due to the *skin effect*, see Fig. 1.8 (b),(d),(f). Moreover, multiple conductors configuration improved the shielding to protect the tapes:

- The TSTC has the highest penetration depth and presents a symmetric behavior along the edges, where the field is perpendicular to the tape surface;
- the Roebel cable has a specular behaviour with a lower field penetration on the innermost side, and higher on the outermost;
- the CORC® has a strong non uniform current distribution: the round geometry allows a good shielding of the innermost layers and reduced the degradation due to the transversal component of the magnetic field.

Thus, the critical current is affected by shape and dimensions of the wire. A numerical model comprehensive of the full 3D geometry of a CORC® cable, the I_c dependence on the temperature and on the magnetic field for the cable prediction of the I_c is missing in literature, which is the topic of this work. In this framework, the development and implementation on Comsol Multiphysics® of a new multiphysics numerical model, based on the $T-A$ formulation and finite element method, is main objective of this thesis, aiming to the characterization of tapes and CORC® cables I_c. The $T-A$ formulation has been used leveraging the high aspect ratio of tapes, suitably coupled with a conduction thermal model which for the first time properly accounts for the cable convective cooling. The model developed can accurately simulate the thermal, electric and magnetic behaviors and the current sharing among tapes by using a set of self-consistent boundary conditions adopted for the first time

in this kind of simulations. The model is verified and benchmarked against other well-established formulations on a set of test cases. The comparison of the computed $V-I$ characteristic of the straight cable and bended to available experimental data shows that the main physics features of the cable are well captured by the model, including performance degradation due to cable tapering at the terminations. The thesis is structured as following:

- Chapter 2 presents a detailed description of ReBCO materials and how it lead to the development of CORC® cable, their performances and the main challenges;
- Chapter 3 is devoted to the description of constitutive laws and main formulations widely applied for HTS components, with particular focus to the model developed in this research;
- Chapter 4 reports the main results of the model along with its verification and validation ;
- Chapter 5 discusses the outcomes of the research activity and sets the basis for future developments for numerical modeling for CORC® -like conductors.

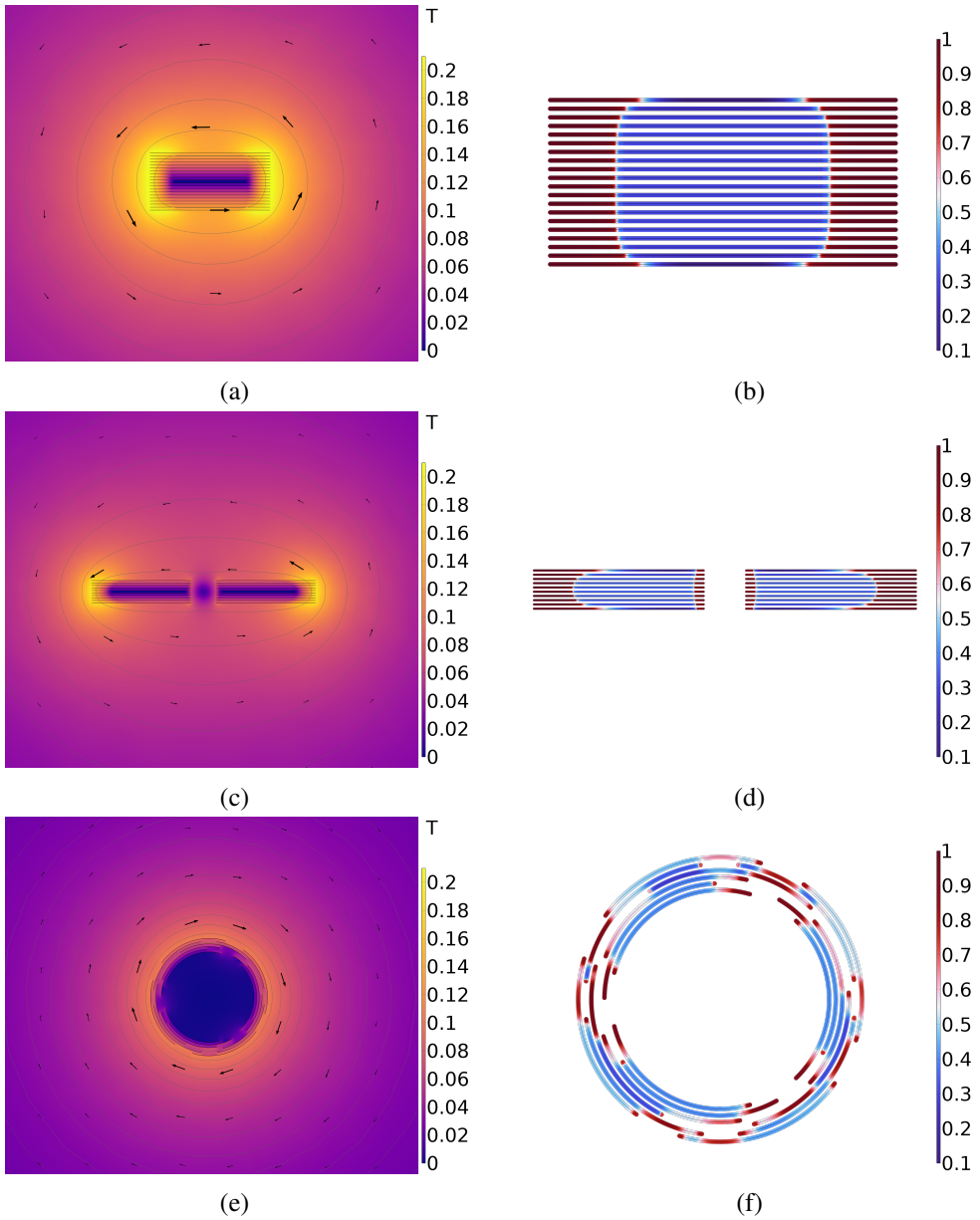

Fig. 1.8 Simplified 2D models for representation of self-field generated from 20 tapes and I/I_c distribution in (a)-(b) TSTC, (c)-(d) Roebel and (e)-(f) CORC® cables.

Chapter 2

Conductor-on-Round-Core cables from ReBCO coated conductors

2.1 ReBCO tapes

ReBCO compounds are a family of ceramic superconducting materials of chemical compositions based on a rare-earth element, barium and copper oxide $ReBa_2Cu_3O_{7-x}$. The most common element used is the Yttrium (Y), which can be interchanged with other RE, as Gadolinium (Gd), without significant impact on the superconducting properties. The standard ReBCO is commercially available from 4 to 12 mm width tapes, and thickness which varies from 40 to 100 μm, according the metallic substrate, see Fig. 2.1). The superconductor layer is coated by a copper stabilizer and silver, and it is separated from the metal substrate with a buffer. The substrate, usually made of Nickel alloy, stainless steel or Hastelloy, is the thickest layer intended to improve the mechanical stability and properties of the tape. The thicker the substrate thickness the stronger the tape, that is easier to handle, but with a consequent reduction of the superconductor cross section fraction, thus in the engineering current density J_e (defined as the ratio of the critical current over the entire cross section of the tape I_c/A_{tape}). The buffer zone, composed of multiple layers, is interposed between the ReBCO and the substrate to avoid chemical diffusion which can corrupt the superconducting properties and to prepare the surface for the ReBCO deposition. Finally, the $1-2$ μm of silver protect the ReBCO from any possible reaction with the copper stabilizer.

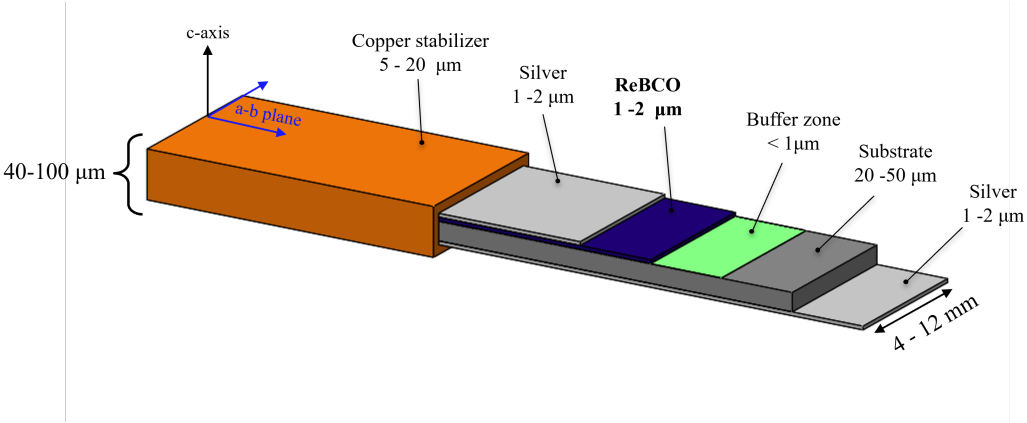

Fig. 2.1 Generic structure of a multilayer ReBCO coated conductor (not in scale).

2.1.1 Tapes manufacturing

The flat geometry of tapes cannot be achieved using conventional metallurgic techniques, but thin film deposition techniques. The ReBCO layer is typically deposited through epitaxial growth to achieve precise alignment of the crystal structure, otherwise the grains bound misorientation creates a resistive barrier to the current flow, with significant impact on the the critical current [83, 84]. Pre-texturing techniques on the substrate tapes ensures the alignment and the growth of the buffer and ReBCO zones. The main texturing methods *Ion Beam Assisted Deposition* (IBAD) [85] and the *Rolling Assisted Biaxially Textured Substrate* (RABiTS) [86]. In the former, textured ceramic biaxially buffers are deposited on top of the substrate preparing a suitable surface for the ReBCO layer aligned through an ion beam [87]. The technique is a relatively low cost and allows scalability, which makes them appealing for the industrial manufacturer; on the other hand, it shows a slow film growth rate (≈ 0.1 nm $\cdot$ s). A variation of it, it is the deposition on *Inclined Surface Deposition* (ISD) [88] and the *Alternating Beam Assisted Deposition* (ABAD), where an alternating beam is applied [89]. The RABiTS technology is based on rolling the substrate and recrystallized through a heat treatment to achieved a cube-metal structure with a controlled orientation [90]. The recrystallization is completed along with buffer layers to protect the ReBCO from chemical interaction with the substrate. As a drawback, Nickel-alloys risk to become ferromagnetic and increases hysteresis losses in AC operations. Then, the epitaxial growth of the superconducting layer happens via chemical or physical processes. Among chemical processes, the most widely used is the *Metal Organic Chemical Vapor Deposition* (MOCVD) [91] and

Metal Organic Deposition (MOD) [92], where the tape is coated by a high purity gas, in the former case, and by a liquid thin film, in the latter, which through chemical reaction with added gas forms the ReBCO . Those methods have a fast deposition rates, but they required a precise stoichiometry and safety procedure to deal with toxic chemical vapors involved. One of the possible physical method is the *Pulsed Laser Decomposition* (PLD): in a vacuum chamber the material vaporizes due to a high-power pulsed laser and it is deposited on the substrate [93]. This process has a high quality of deposition, but high cost compared to the growth rate of production of the layer. A more recent physical procedure is the *Reactive Co-Evaporation* (RCE) where, again in a vacuum chamber, each element individually is evaporated and then deposited [94]. Finally, the tape is coated with silver, which is inert with ReBCO , and electroplated with copper (one side, both sides or fully surrounded): the latter protects the material from oxidation, offering at the same time a parallel path for the heat and current flows. Thus, it increases the stabilization of the conductor. At the time of the writing, more than ten industrial manufacturers are active and use different procedures and methods for the realization of a tape, which leads to different performances and critical current [81, 95].

2.1.2 Tapes performances

The first interest in ReBCO derived from the outstanding performances and extremely high J_c, see Fig. 2.2. The ReBCO has the highest critical current density ever reached among any known superconducting material. From Fig. 2.2, it possible to notice that above 25 T, all LTS materials have reached the normal state, and only BSCCO and ReBCO are still superconductive. For those reason, ReBCO is the most promising materials for the realization of next generation of high-field magnets. Nevertheless, the critical current is strongly related to the manufacturing process. In [96], ReBCO samples from seven manufacturers have been investigated at 4.2 K and 18 T perpendicular field, reporting a non-negligible difference in terms of I_c, see Fig. 2.3. Performances can be improved through:

- Artificial doping: which implies to add impurities as Zirconium, which helps to increase pinning centers [97];
- Reduction of the substrate thickness: beneficial for high field application, losing part of the mechanical strength [98].

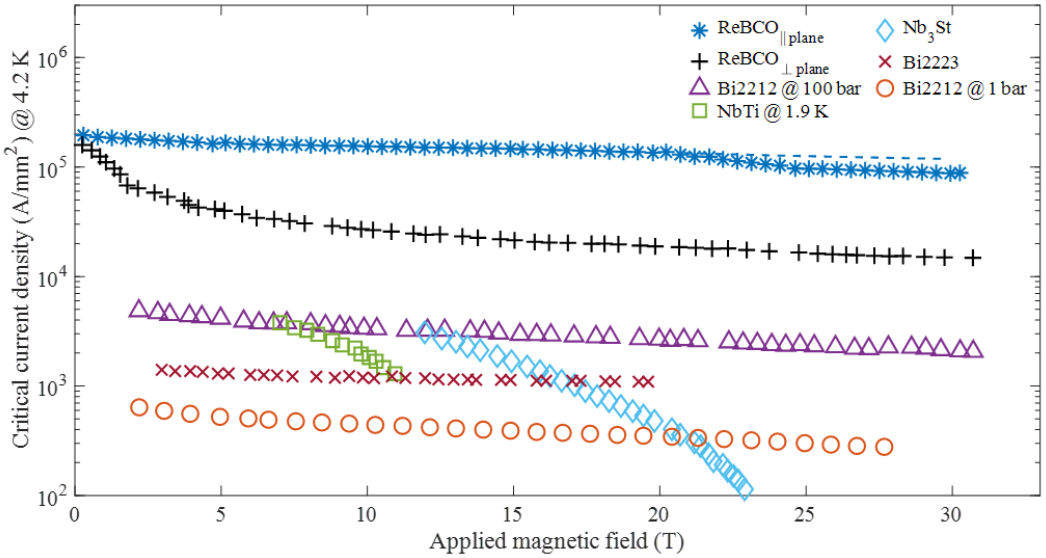

Fig. 2.2 Critical current I_c vs magnetic field applied B of II-type superconductor @ 4.2 K adapted from [12].

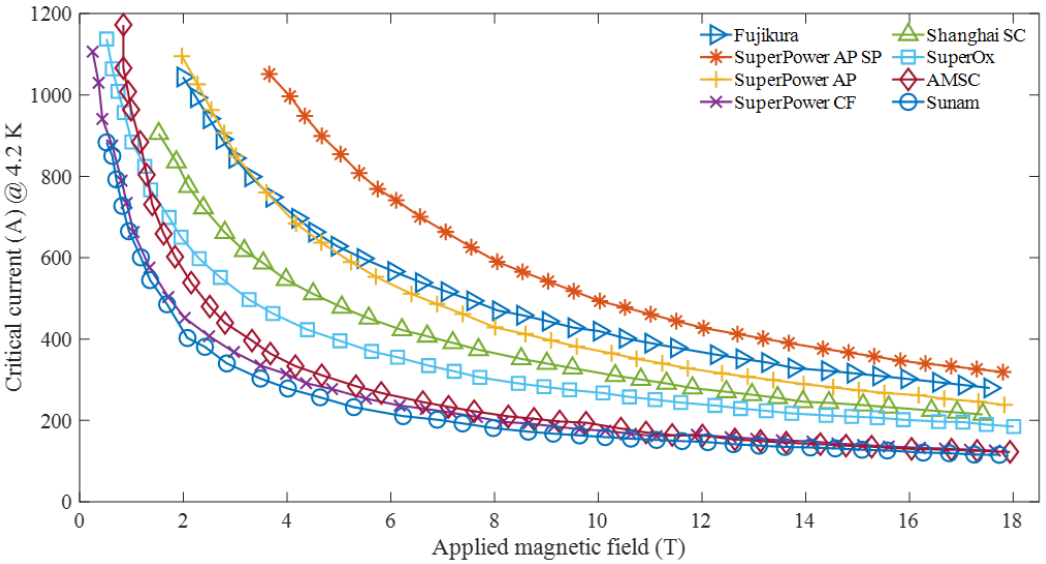

Fig. 2.3 Critical current I_c vs magnetic field applied B @ 4.2 K of 4 mm-width ReBCO tapes from different manufacturers adapted from [96] and all data referred to 2017. For SuperPower there are three methods: CF, non-doped tapes; AP (=Advance Pinning) adding Zr; and AP SP(=Special) characterized by a thinner substrate of 30 μm.

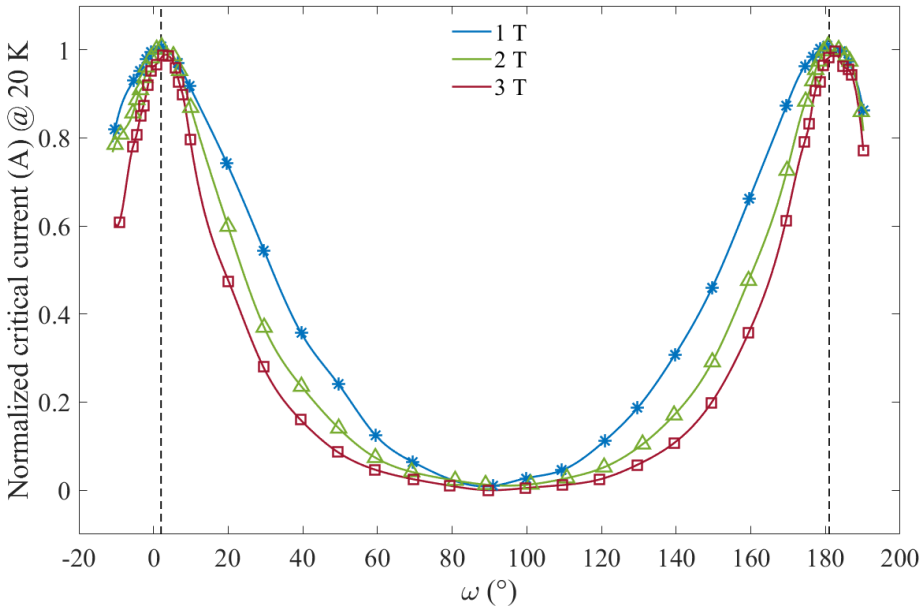

Fig. 2.4 Critical current I_c vs orientation of the magnetic field applied @ 20 K and at three different magnetic field amplitude, adapted from [107]. When the angle ω is equal to 0 degree and 180 degree, the magnetic field is applied along the c-axis, thus perpendicular to the tape surface. The critical current is normalized respect to the minimum and the maximum critical current of each case.

Another optimization of ReBCO tapes is the reduction of the tape with or the engraving of striation on the tape surface [99–101] to reduce the AC losses and increase the flexibility when twisted on an core, i.e. on CORC® wires [102–106]. In addition, as anticipate in 1.2, ReBCO coated conductors show a strong anisotropy of which the I_c doesn't only depend on the amplitude of the magnetic field, but also from its orientation, see Fig. 2.4. The HTS tapes best perform when the magnetic field is parallel to the ab-plane, and strongly degrade when it is parallel to the c-axis. The angular anisotropy of the critical current introduces an additional complexity for the designing of magnets and devices. Roebel and TSTC cables has the advantage to experience the same magnetic field along the length, which can be direct in the preferable orientation. While in CORC® cables, the orientation of the magnetic field changes along the pitch. Therefore, the tape-to-tape contact firmly impacts on the current sharing among them to possibly improve the performance of the entire cable. This anisotropy is considered in this work through Equation (3.30), reported in Section 3.2.1.

2.1.3 Tapes mechanical properties

Initially, ReBCO coated conductors have been developed for power transmission application due to their high critical temperature ($T_c = 93$ K), to potentially use of liquid nitrogen (77 K at 1 bar) as coolant [108]. Nonetheless, their very high mechanical strength lead to demonstrate the successful application for high-field magnets, which has become the main driving force of ReBCO development [81]. The metallic substrate, acting as mechanical support, increases the resistance on the tensile efforts along the longitudinal direction. Moreover, the other mechanical properties as Young modulus and elastic limit constraint of the whole tapes result to be very close to the one of the substrate [95]. As ceramic material, micro-cracks on the thin ReBCO layer may inflict a reduction of I_c [109]. Due to the strong dependence of the critical current on the strain, such material are called strain-sensitive. The dependence is approximately parabolic for ReBCO coated conductors, but it results linear when fabricated through Inclined Substrate Deposition (ISD) [110], see Section 2.1.1. The degradation due to the axial strain also depend on the thickness of the stabilizer [111] and of the substrate [112]. In literature, there are multiple study based on experimental campaign for evaluation of the dependence of the critical current under uni-axial strain [113, 114, 20, 115, 116]. From measurements, it comes out that compression state allows much lower bending radii than the tensile state [117, 118], where the tape is weaker, see Fig. 2.5. Tapes can resist at least till -1.25% of compressive straing before mechanical degradation occurs irreversibly. The limit of the tensile strain is given from the substrate yields, which varies from 0.4% to 0.7% according the metal composition and thickness [119]. In [120], authors applied a compressive stress perpendicular to tapes surface to the I_c degradation. They found out that they can resist till 300 MPa without significant reduction of performances. While, transverse tensile stress has a strong impact on the critical current after 15 MPa, before delamination (the tensile stress at which the ceramic layers delaminate from one another) for weak conductors [20]. Since the ReBCO layer is usually above the neutral axis of the tapes, see Fig. 2.6, in configuration on CORC® cable, it is wounded facing inwards (facing the former), thus it is under compressive state [121]. Therefore, the transverse load in CORC® is mainly due to the bending and the Lorentz forces. Thinner substrates allow smaller bending radii along with the reduction of the minimum core diameter of a CORC® . At the same time, the engineering current density (the one considered on the whole tape area) also increases, as stated in Section 2.1.2, making

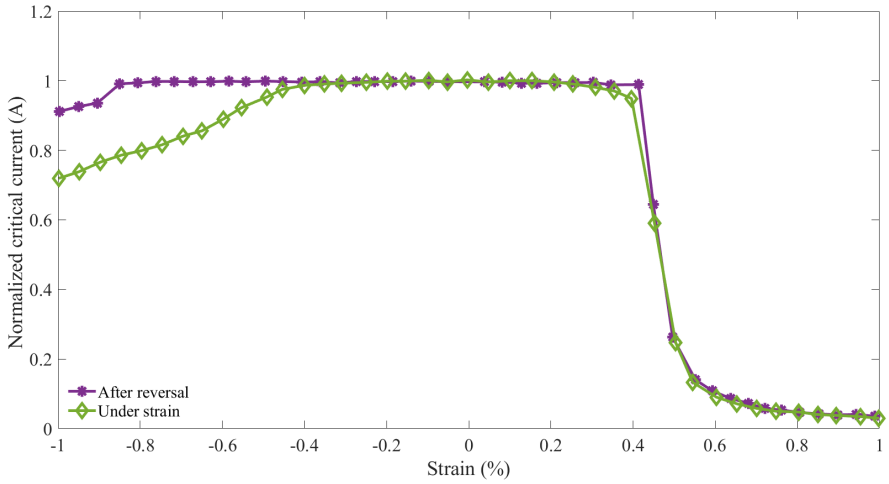

Fig. 2.5 Normalized critical current $I_c/I_{c@\varepsilon=0}$ as function of bending for a for SuperPower 100 mm-width thick substrate tape @ 77 K, from [117].

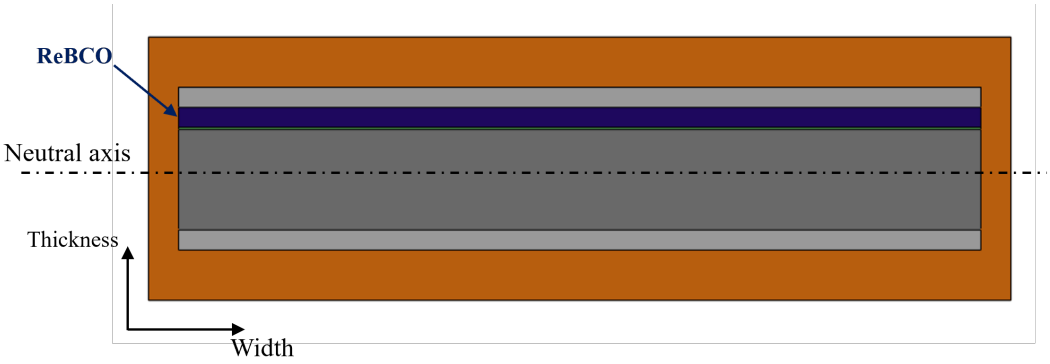

Fig. 2.6 Sketch of a typical commercial ReBCO tape cross section (not in scale). The neutral plane lies approximately at the center of the substrate. The ReBCO layer is above the neutral axis.

CORC® wires suitable for high-field magnets. The strain effect on the critical current has been taken into account in this work through simplified evaluation of the strain, based on pure geometrical assumptions. The strain map allows to determine the I_c degradation due to the deformation on the entire domain under study, see Section 3.3.4.

2.1.4 Drawbacks

Beyond the excellent performances of ReBCO coated conductors, there are some drawbacks to take into account for the design a coil:

- The flat shape: as discusses in Section 1.3, this new concept required new cable layout, impossible to bend in the hard way.
- The material cost: even though, the latest improvements of ReBCO , especially with very critical current at high-field, it starting to be comparable with LTS [122].
- The quench propagation velocity: the quench is a sudden phenomenon, happening for defect or unexpected deposition of heat, during which the temperature of the conductors rise and the critical current decrease. Due to the low thermal diffusivity of ReBCO , the dissipation of that release of heat is 1 to 10 mm/s [123] around $1-3$ order of magnitude slower than LTS 1 to 100 m/s [124]. The main risk is the *hot-spot* temperature which may cause an irreversible damage of the device.
- The angular anisotropy of the critical current on the magnetic field.

The realization of next-generation magnets based on ReBCO technology requires new concepts and methods able to deal with the limits of such material.

2.2 Conductor-on-Round-core (CORC®) state-of-art

The concept of CORC® cable born from the combination of the high mechanical strength of the metallic substrate, able to withstand axial tensile stress, and the

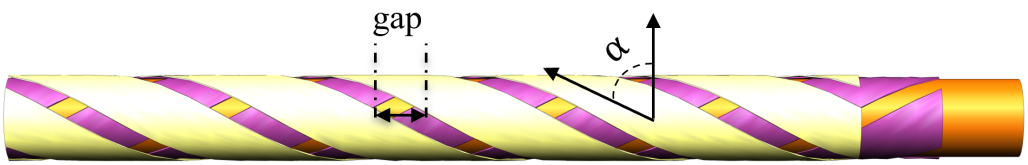

Fig. 2.7 Schematic illustration of the winding angle and gap space among ReBCO tapes in a 2-layers CORC® cable.

elasticity of ReBCO , capable to resist to compressive strains. The first proof-of-concept was demonstrated in 2009 by Danko Van der Laan [38] who wound a single tape composed of 50 μm thick substrate and 20 μm thick copper plate stabilizer on a former of 3.2 mm for different winding angles. It is the first round cable configuration of HTS tapes: wounded inwards onto small formers in multiple layers, alternative clockwise and counter-clockwise, to reach mechanical and electromagnetic isotropy. The spiral shape helps in reducing the AC losses and the high flexibility is due to the tapes sliding which may occur during bending [39].

2.2.1 Fabrication and performances

A key parameter that allow for the development of CORC® is the mechanical behaviour of ReBCO tapes with respect the other HTS materials. The ReBCO allows much smaller former diameter [38]: Bi2223 required former of 40 mm diameter to safely work from far for the irreversible strains ($0.2-0.4\%$ in tensile mode, and 0.1% under compression [125, 126]). Smaller former will increase the superconductor over stabilizer fraction, with a consequent increase of the engineering current density (J_e). A record of $J_e = 344$ A/mm^2 at 17 T and 4.2 K has been reached in 2016 in a CORC® wire composed of 30 μm substrate and 1.6 μm ReBCO layer doped with 7.5% Zr and 2.4 mm core diameter [127]. The second fundamental parameter to consider for cable performance is the winding angle, see Fig. 2.7. The CORC® geometry exploits at the best the reversible anisotropy of the strain with respect the angle [110]. Even though, winding process can drastically affects the I_c of tapes, the reversible strain effect almost disappears when the strain is applied at 45 degree [42]. Therefore, winding tapes with a 45 degree angle in CORC® can prevent degradation of the I_c, as long the irreversible strain is not exceeded. Another

issue to consider and optimize is the gap space among tapes lying on the same layer. Too narrow gaps makes problematic bending the cable, but larger distances would decrease the J_e, see Fig. 2.7. Moreover, limiting the gap space can avoid tape buckling (a sudden change of shape due to a compression strain). During the bending process, a too loose tape, when sliding, can be pressured between two tapes if the gap is too large [128]. A buckler tape may experience a total reduction of the critical current reaching the irreversible strain. Smaller gaps, higher winding tension and lubrication, to facilitate the sliding, can eventually reduce the risk of buckling. The gap space should be optimized according the application to find the best compromise among flexibility to bend the cable without degradation, high J_e and buckling prevention. From [9], the minimum space among tapes can be estimated as function of the bending radius r_b and CORC® diameter d_{core}:

$$gap_{min} = \frac{d_{core}}{r_b - d_{core}} \cdot \frac{w}{cos(\alpha)} \tag{2.1}$$

where w is the tape width, α is the winding angle. The production process consists in pulling the former core through a machine which wind, layer by layer, ReBCO tapes around it, see Fig. 2.8a. Finally, it is usually covered by a polyethilene insulation to keep tapes together and limit their movements. The complexity is mostly due to the tensile load during production. If the pre-load is too high, it may cause microfractures on the tape surface compromising the performances of the cable. On the other hand, a too weak tensile winding load could lead to loosen tapes and buckling. The substrate thickness impacts on the level of pre-load that the cable can handle. The cable length is mainly limited by the amount of tape available and the length of the machine.

2.2.2 Current injection into CORC®

Guaranteeing a homogeneous injection of current into CORC® cables and wires is a determining factor for the conductor performances. Due to the large number of tape and the overlapping geometry, the use of low-resistance termination to improve the current distribution is not trivial. This is still subject of studies and research for their optimization [9, 130, 131]. The non-homogeneous current distribution has a strong impact on the critical current of each tape, since it is function of the transport current, with a consequence risk of early quenches and higher voltage drops. The ACT has

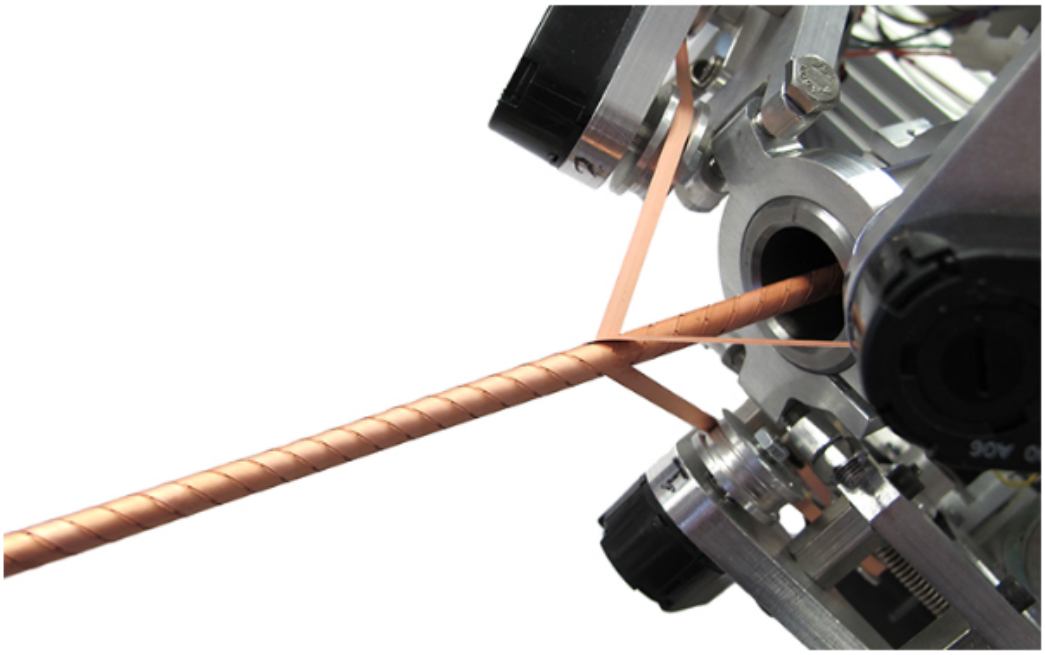

(a)

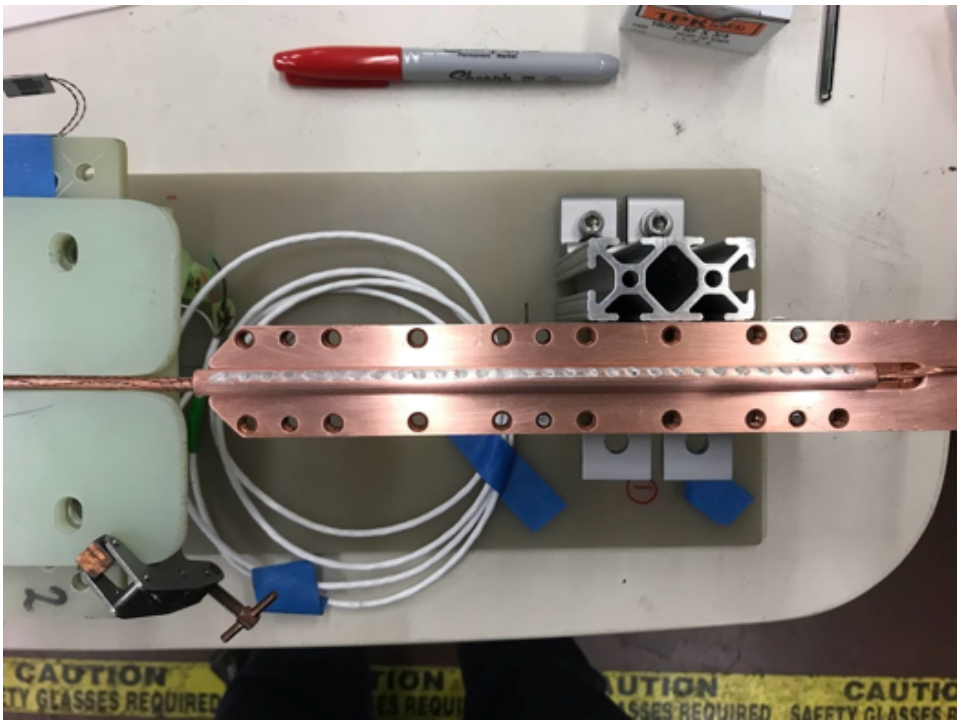

(b)

Fig. 2.8 (a) CORC® cable production cable machine from [129]. (b) Picture of CORC® cable termination (courtesy of LBNL).

patented a method in [132] according to which the cable ends are trimmed and each tapes is exposed to the termination. When the plastic coverage is removed, tapes tends to expand radially, see Fig. 1.7 and Fig. 2.8b. This tapering is exploited to directly imposed current in each tape, improving the homogeneity. Nonetheless, in short samples due to the complexity to guarantee enough accurate measures, this can affect the inductance of the system, and therefore the conductor electric behaviour. In Section 4.4, it is shown how terminations strongly affect the cable performances.

2.2.3 Drawbacks

Beyond the flexibility and potentially high critical current achievable, there are some drawbacks in CORC® concept:

- Use of material: the spiraling required an higher amount of material for a smaller length. The amount depends on the winding angle and vary in each conductor.
- Cable cost: strictly related to the use of material.
- Conductor efficiency: defined as the ratio of conductor length over tape length per tape. It is variable for CORC® between $0.6 - 0.9$ [9]. As comparison, the Roebel cable has the lowest, since part of the HTS material is cut away, and the TSTC has the maximum, equal to 1.
- Delicate production process and mechanical stability: see Section 2.2.1.
- Termination resistance and current injection: see Section 2.2.2.

The improvements for the conductor optimization is focusing in thinner ReBCO tapes which can allow smaller core diameter [42].

2.2.4 High field applications

CORC® cables and wires are developed for wide applications from power transmission [133], fault current limiter [134], high-field magnet [80, 135]. Here, we mostly focus on fusion magnets and particle accelerators.

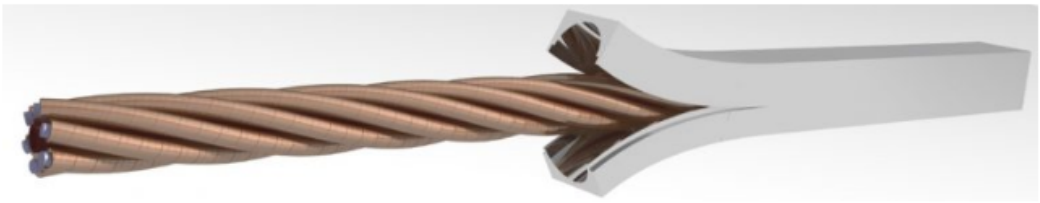

Fig. 2.9 CORC® for fusion from [129].

CORC® for fusion

The next generation of fusion reactors are relying on HTS material to reach more compact layout, until 4 times than the previuous design fully based on LTS [136], and higher fields. CORC® cables and wires are not sufficient themselves to provide enough current needed for fusion machines. Therefore, a possible candidate would be a combination of CORC® wire in the well-established layout of Cable-in-Conduit-Cable (CICC) [80], see Fig. 2.9. The European DEMO project, mostly based on the ITER project, is exploring the HTS and hybrid solutions for the central solenoid of the machine [137], to safely operate at 46.5 kA, 20 T, and 4.5 K [28]. CORC® -CICC are one of the possible cables layouts options for this design, as well for the China Fusion Engineering Test Reactor [41]. Also CERN has shown interests in CORC® -CICC for the development of high-current detector conductors and bus lines [9]. CORC® -CICC are composed from 6 (the so-called 6-around-1 design) to 20 CORC® wires twisted among a central hole, in which forced-flow coolant would flow through. The bundle is encapsulated in a stainless steel jacket. The twist pitch of CORC® -CICC ($100 - 300$ mm [42]) is the key point of maintain enough flexibility to easy bend the cable prevent irreversible degradation. The mechanical decoupling of CORC® strands is a further improvement for the flexibility of the CICC. The decoupling limits the accumulation of stress on CORC® wires, and at the same time allows them for easier sliding.

CORC® for particle accelerators

The target for future colliders is reaching 20 T level field. One of the main challenges of the high field superconductor magnet is withstanding the Lorentz forces generated within the magnet. Within this framework, the Canted-Cosine Theta (CCT) magnet

concept, proposed in 1970 [138], turns out to be particularly promising for strain-sensitive superconductors, such as ReBCO . The CCT is based on a cable wound in superposed layers of oppositely tilted solenoids such that the current distribution generates a pure harmonic field: in this configuration, the transverse field components will sum up, and the solenoidal will cancel out, see Fig. 2.10. Within a single layer, the cable, assembled with standard conductors or SC wires or tapes, is contained within the grooves of a mandrel, avoiding the summation of electromagnetic forces [139]. In this contest, the CORC® wires and cables are a viable options for dipole magnet [140]. The Lawrence Berkeley National Laboratory (LBNL) is mostly leading the implementation of CORC® based CCT [141]. In collaboration of LBNL, my research activity took place for the development of a reliable numerical model able to reproduced, and predict the behaviour of the CORC® cable conductor and of an entire coil in perspective.

2.2.5 Numerical model for CORC® cables and wires

This section is dedicated to a brief literature review about numerical models developed for CORC® cables. Portions of the present chapter were already published in the following scientific papers:

- S. Viarengo, L. Brouwer, P. Ferracin, F. Freschi, N.Riva, L. Savoldi, X. Wang, "A New Coupled Electrodynamic T – A and Thermal Model for the Critical Current Characterization of High-Temperature Superconducting Tapes and Cables," in IEEE Access, vol. 11, pp. 107548-107561, 2023, doi: 10.1109/ACCESS.2023.3321194, [2];
- S. Viarengo, F. Freschi and L. Savoldi, "CORC Cables: Numerical Characterization of the Critical Current After Bending," in IEEE Transactions on Applied Superconductivity, vol. 34, no. 5, pp. 1-5, Aug. 2024, Art no. 4801605, doi: 10.1109/TASC.2023.334809, [142].

CORC® layout has geometry and shape tricky to reproduced correctly and study with numerical tools. Different electromagnetic formulations can be applied for simulations, see Section 3.1, and the computation cost is usually really high when the entire volume is considered. In 2016, a thin shell solutions has been introduced by [143] to reduce the simulation time. One of the main aspect about CORC® is

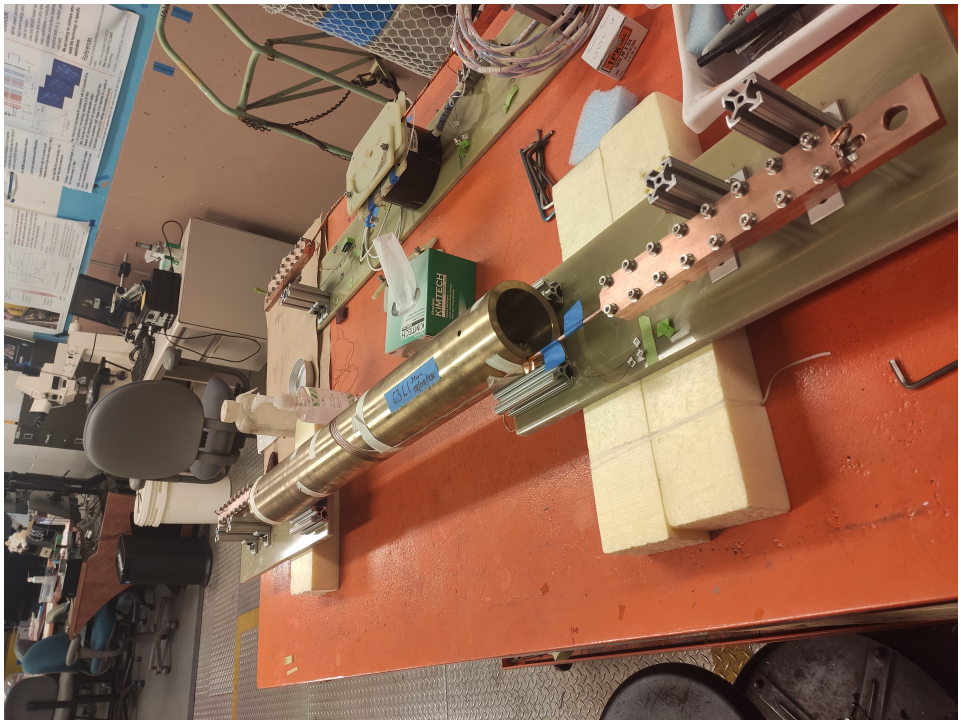

(a)

(b)

Fig. 2.10 CORC® for particle accelerators wounded on mandrel's grooves for Canted-Cosine Theta (CCT) application, from LBNL.

the reduction of AC losses, and multiple models have been implemented for that [144–148]. In this work, the aim of the research is the characterization of I_c, thus under DC operations. Section 2.2.5 and Section 2.2.5 report the status of numerical models focused to correct current distributions among tapes and local strain map, respectively.

Current distribution among tapes and layers

One of the crucial aspects for the CORC® is the proper computation of the current distribution among tapes and the possible re-distribution due to external disturbance. Some simplified approaches simulate the current distribution on CORC® by an equivalent network model [149] or represent the 2D cross-section of cables where the helical structure is neglected [150–153]. However, due to the peculiar geometry, those simplifications do not allow to properly reproduce the actual cable behavior and the accurate evaluation of losses, which mostly occur on CORC® edges [153, 154]. Therefore, 3D models are widely used especially focus on AC losses evaluation and magnetization. The well-known H-formulation is currently applied in such models [155, 156, 147, 157, 144] and it is usually considered as reference to verify other formulations [150, 152]. The T-formulation, based on current vector potential, is also often used for AC losses evaluation as in [158], the significant effects of gaps in spiraled coated conductors [159]. In [74], the T is also coupled to Biot-Savart's law for computing the current distribution along the tape width and the localized ac loss distribution. Note that in those model, only the superconducting domain is discretized and solve. Nonetheless this model is very ill-conditioned, in [160] an algebraic multigrid preconditioning is proposed to stabilized the solution. The method currently used to impose a transport current in the $T-A$ formulation doesn't guarantee any self-consistent current distribution (or redistribution) among tapes. In [161] an equivalent circuit model, applied also in [162], is proposed to compute the current redistribution during a quench, depending on the equivalent resistance of each tape and on self and mutual inductance. The model is coupled with the T formulation: the resistance is evaluated in the T module and the electric network gives back the current distribution. This procedure requires the implementation and the coupling with a third lumped circuit module, creating additional issues on the convergence and stability of the solution. In [152] a Neumann boundary condition, which allows a coupling effect between the T and the A, is presented. It is demon-

strated in the paper that the current redistribution is affected by **A** through the electric field **E** across the boundary and **B** inside the tape. The condition is given in a weak form, and it allows a non-uniform redistribution of the current in the cable. However, this condition increases the complexity of the problem along with the risk that the current is not conserved.

Mechanical analyses

Numerical models capable to predict the cable performance should proceed along with experimental characterization. Some analytical solution for the strain prediction on a tape are present in literature: in [121], a curvature-based model provided analytical formulas for strain computation for different bending modes, without taking into account local deformation due to the Poisson's effect. In [163], a parametric analysis for different bending radii were performed numerical and analytically based on Flexure formula. In [164, 165] and [166], structural finite element analyses were used to investigate the mechanical strain generated in tapes with different winding angles: the studies showed that compression decreases towards the edge along the tape width. A combined tension and torsion analysis is carried out in [167]. Regarding the CORC® cable, in [168] a 3D mechanical simulation computed the strain distribution on tapes, after winding and bending processes, to compare results with critical current and AC losses measurements on a 6-layer CORC® coil built from authors. In [169] a detailed parametric analysis, validated through experiments, aimed at defining the stress-strain state for the determination of the critical strain that may cause the breakage of the YBCO layer, considering the bending of the cable. In [170] and in [171], electromechanical simulations, based on $T-A$ formulation, were performed to predict the strain state and the critical current degradation for straight CORC® cables.

Proposed multiphysics numerical model

This work presents a full 3D multiphysics model, specifically proposed for CORC® -like conductors, which tries to answer some questions: how does the current distribute among tapes within the cable? How much do temperature and magnetic field influence the maximum allowable current of the conductor? Which is the strain

status, and how much does it degrade the cable performances? The $T-A$ formulation has been used, leveraging the high aspect ratio of tapes. It is suitably coupled with a conduction thermal model which, for the first time, properly accounts for the cable convective cooling. The I_c scaling law in each tape accounts for the local strain through a pure geometrical strain evaluation on the tape surface, which allow to account for the punctual degradation of I_c, as an input for the multi-physics model. The capability to compute and redistribute the current without any external circuital network, according to possible disturbance or defect on each tape (i.e., hot spot temperature or electromagnetic difference) is one of the main novelty. A new boundary condition is proposed in the strong form: the redistribution of the current in the cable is guaranteed imposing, among two subsequent boundaries, the current vector potential $\mathbf{T}$ to be uniform and equal, see Section 3.3.2. The model aimed to the characterization for of the critical current of CORC® cables and wires, needed as first step for the prediction of an entire coil behaviour. The model relies on a multiscale approach starting from the homogenization of the tape properties that are then applied to the CORC® cable. The model has been verified and benchmarked against the well-established electromagnetic formulations, under different conditions, and it has been able to reproduce the $V-I$ characteristic curve and validated with respect experimental data obtained at Lawrence Berkeley National Laboratory (LBNL). The model has been proved under a series of test cases, different configurations and operating conditions, demonstrating its stability and reliability to properly reproduce the described physics and replicate the critical current, albeit not fully capturing the entire behavior of the cable.

Chapter 3

Numerical modeling for HTS tapes and cables

This section is dedicated to the description of the proposed model for ReBCO tapes and CORC® cables, starting from the most common formulations widely exploited for HTS components simulations, the constituive laws and tape homogenization. Portions of the present chapter were already published in the following scientific papers:

- S. Viarengo, L. Brouwer, P. Ferracin, F. Freschi, N.Riva, L. Savoldi, X. Wang, "A New Coupled Electrodynamic T – A and Thermal Model for the Critical Current Characterization of High-Temperature Superconducting Tapes and Cables," in IEEE Access, vol. 11, pp. 107548-107561, 2023, doi: 10.1109/ACCESS.2023.3321194, [2];
- C. Messe, N. Riva, S. Viarengo, G. Giard, and F. Sirois, "Belfem: a special purpose finite element code for the magnetodynamic modeling of high-temperature superconducting tapes", Superconductor Science and Technology, vol. 36, Nov. 2023, [172];
- F. Freschi, L. Savoldi and S. Viarengo, "Nonlinear Magneto-Quasistatic Simulation of Superconducting Tapes With $a - \phi$ Algebraic Formulation," in IEEE Transactions on Magnetics, vol. 60, no. 3, pp. 1-4, March 2024, Art no. 9000204, doi: 10.1109/TMAG.2023.3315474, [173];

- S. Viarengo, F. Freschi and L. Savoldi, "CORC Cables: Numerical Characterization of the Critical Current After Bending," in IEEE Transactions on Applied Superconductivity, vol. 34, no. 5, pp. 1-5, Aug. 2024, Art no. 4801605, doi: 10.1109/TASC.2023.334809, [142].

The method can be used for general-purpose, e.g. for evaluation of AC losses, estimation of the produced magnetic field, and for current density distribution and for different geometries of superconductors. However, we pose the particular focus to the model based on the T-A formulation proposed for the characterization of the critical current of tapes and CORC® cables: the model has been first verified and validated for a single tape with a 2D magnetostatic model and measurements; then, extended to more complex geometries (CORC® from 1 to 6 layers) verified with respect the well-known H-formulation and experimental results (when available).

3.1 Electromagnetic formulations

Numerical models for superconductor are commonly base on Finite Element Methods (FEM) and all of them use Maxwell's equations, under the magneto quasi-static (MQS) approximation [174], written in different forms with a different state variable. In differential form and SI units, Maxwell's equations can be written as:

$$\nabla \cdot \mathbf{D} = \rho_c \tag{3.1}$$

$$\nabla \cdot \mathbf{B} = 0 \tag{3.2}$$

$$\nabla \times \mathbf{E} = -\frac{\partial \mathbf{B}}{\partial t} \tag{3.3}$$

$$\nabla \times \mathbf{H} = \mathbf{J} + \frac{\partial \mathbf{D}}{\partial t} \tag{3.4}$$

considering the following constitutive laws:

$$\mathbf{B} = \mu \mathbf{H} \tag{3.5}$$

$$\mathbf{D} = \varepsilon \mathbf{E} \tag{3.6}$$

$$\mathbf{J} = \sigma \mathbf{E} \tag{3.7}$$

Where D is the electric flux density, E is the electric field, ρ_c is the electric charge density, B is the magnetic flux, H is the magnetic field, J is the current density, ε is the magnetic permittivity of the medium, μ the magnetic permeability and σ is the electric conductivity. In the case of hard superconductors, we usually neglect the effect of Meissner currents and we consider just the vacuum permeability $\mu = \mu_0$. The Gauss's law (3.1) defines relationship between an electric field and electric charges, proportionally with the permittivity of free space. Under the assumption of MQS, this equation can be neglected. The Gauss's law for magnetism (3.2) states that electric charges don't have magnetic monopoles, but the magnetic field attributed to a dipole and the net outflow through a closed surface is zero. Therefore, the magnetic field induced in the air forms loops or extends to the infinity. The Faraday's law (3.3) describes the curl of an electric field correspondent to a time-varying magnetic field (electromagnetic induction). Finally, the Ampère-Maxwell's law (3.4) relates the magnetic field to electric currents and displacement currents. The MQS approximation means that displacement currents are negligible than conduction currents in the medium [174]. Consequently, we can reduce it as:

$$\nabla \times \mathbf{H} = \mathbf{J} \tag{3.8}$$

where H is the magnetic field. Aiming to reducing the computational cost, guaranteeing the highest accuracy, the most commonly used formulations are reported in the following sections.

3.1.1 Magnetostatic model

The magnetostatic 2D model, describe in [79], allows the characterization of the critical current in a infinite non-twisted tape/cable. The model solves a magnetostatic problem based on A-formulation finding the distribution of the vector potential A such that inside the superconductor the current density is $J = J_c$ everywhere.The magnetic vector potential $\mathbf{A}$ is defined as:

$$\mathbf{B} = \nabla \times \mathbf{A} \tag{3.9}$$

where B is the magnetic flux density. The electric field can be re-written:

$$\mathbf{E} = -\frac{\partial \mathbf{A}}{\partial t} \tag{3.10}$$

Based on Ampère's law (3.8) and Ohm's law (3.7):

$$\nabla \times \left(\frac{1}{\mu} \nabla \times \mathbf{A} \right) = -\sigma \frac{\partial \mathbf{A}}{\partial t} \tag{3.11}$$

where μ is the magnetic permeability and J is the electrical current density. The wire is assumed infinite in the axial direction, so that the magnetic vector potential and the current density have only z-components. The critical current of the 2D cross section is determined by integrating the critical current density distribution obtained from the model over the stack cross section.

3.1.2 H-formulation

The H-formulation is the most established and largely adopted formulation for simulating HTS material, and it is usually used as reference for the development of other formulations [155, 156]. The formulation used the magnetic field H as the state variable, and the final governing equations is obtained merging the Ampère's law (3.8) with the Faraday's law (3.3):

$$\nabla \times \left[\frac{1}{\sigma_{eq}} \nabla \times \mathbf{H} \right] = -\mu \frac{\partial \mathbf{H}}{\partial t} \tag{3.12}$$

The electric field is defined as:

$$\mathbf{E} = \frac{1}{\sigma_{eq}} (\nabla \times \mathbf{H}) \tag{3.13}$$

The second Gauss's law (3.2) is used as boundary condition of the air domain, if any external field is applied:

$$\frac{\partial}{\partial t} (\nabla \cdot \mathbf{H}) = 0 \tag{3.14}$$

The transport current can be imposed integrating the current density over the cross-section of the superconductor:

$$I = \int_S \mathbf{J} \cdot \mathbf{dS} \tag{3.15}$$

3.1.3 $H - \phi$ formulation

Pursuing the aim of reduction of the computational cost, mixed formulations are particularly attractive since they combine the benefits of each formulation making the model more efficient. One of the possible hybrid formulations exploits the H state variable for the conducting domain and the magnetic scalar potential ϕ in the non-conducting domain (air). The scalar potential ϕ is a quantity which the magnetic field where there is no free current, and it can be expressed as the negative gradient of H:

$$\mathbf{H} = -\nabla\phi \tag{3.16}$$

The formulation derived from a weak formulation of the Gauss's law for magnetism (3.2), or directly from Faraday's law (3.3) exploiting the fact that the curl of a gradient is zero [175]. The advantage of using ϕ is the reduction of unknowns degrees of freedoms of the problem, therefore of the number of unknowns [176]. The current constraint is imposed using cohomology cuts [177] to ensure that circulations of the magnetic field around conducting domains are equal to the net current, while any external field can be applied as a non-homogeneous Neumann condition on the boundary. More information about numerical stability can be found in [178] and detailed explanations on domain interfaces between the conducting and non-conducting regions are [179]. Moreover, due to the high aspect ratio of the HTS ReBCO tapes, the thin-shell simplification, either in 2D and 3D, can give the opportunity of more efficient simulations for more complex geometries, as CORC® cable [172].

3.1.4 T-A formulation

The main focus of this work is the mixed formulation called $T - A$ formulation [143], based on the introduction of two potentials: the current vector potential $\mathbf{T}$ for the conducting domain, and the magnetic vector potential $\mathbf{A}$ for the whole domain (both conducting and non-conducting domain), see Fig. 3.1b. Under the thin shell assumptions, this formulation is is gaining interest in view of the saving in terms of computational time [150, 152, 146, 148, 162, 154]. While macroscopic quantities (i.e., magnetization and AC losses) can be properly calculated assuming an infinitely thin SC films, the local distribution of current density in AC cannot reliably computed

inside the SC tape [144]. Assuming that:

$$\nabla \cdot \mathbf{J} = 0 \tag{3.17}$$

the state variable $\mathbf{T}$ is solved for the HTS tapes has the curl of the current density:

$$\mathbf{J} = \nabla \times \mathbf{T} \tag{3.18}$$

From Ampere's law (3.4):

$$\nabla \times \mathbf{H} = \nabla \times \mathbf{T} \tag{3.19}$$

Leveraging of the identity principle for which $\nabla \times (\nabla \phi) = 0$, from the previous equation we can write:

$$\mathbf{H} = \mathbf{T} - \nabla \phi \tag{3.20}$$

Finally, from Ohm's law (3.7):

$$\nabla \times \left[\frac{1}{\sigma} \nabla \times \mathbf{T} \right] \cdot \mathbf{n} = -\mu \frac{\partial}{\partial t} (\mathbf{T} - \nabla \phi) \tag{3.21}$$

Since the current flows in thin sheets, it can only goes along the tangential direction of the tape and it is supposed to be uniform along the width, neglecting the component orthogonal to the surface. Hence, $\mathbf{T}$ is considered always perpendicular to the shell surface, see Fig. 3.1a. Therefore, $\mathbf{T}$ can be re-written as scalar $T \cdot \mathbf{n}$:

$$\mathbf{T} = T \cdot \mathbf{n} = T \begin{bmatrix} n_x \\ n_y \\ n_z \end{bmatrix} \tag{3.22}$$

where T is the magnitude of the current vector potential and $\mathbf{n}$ is the unit vector orthogonal to the tape surface. The current density can be expressed as:

$$\mathbf{J} = \begin{bmatrix} J_x \\ J_y \\ J_z \end{bmatrix} = \begin{bmatrix} \frac{\partial (T \cdot n_z)}{\partial y} - \frac{\partial \left(T \cdot n_y \right)}{\partial z} \\ \frac{\partial (T \cdot n_x)}{\partial z} - \frac{\partial (T \cdot n_z)}{\partial x} \\ \frac{\partial \left(T \cdot n_y \right)}{\partial x} - \frac{\partial (T \cdot n_x)}{\partial y} \end{bmatrix} \tag{3.23}$$

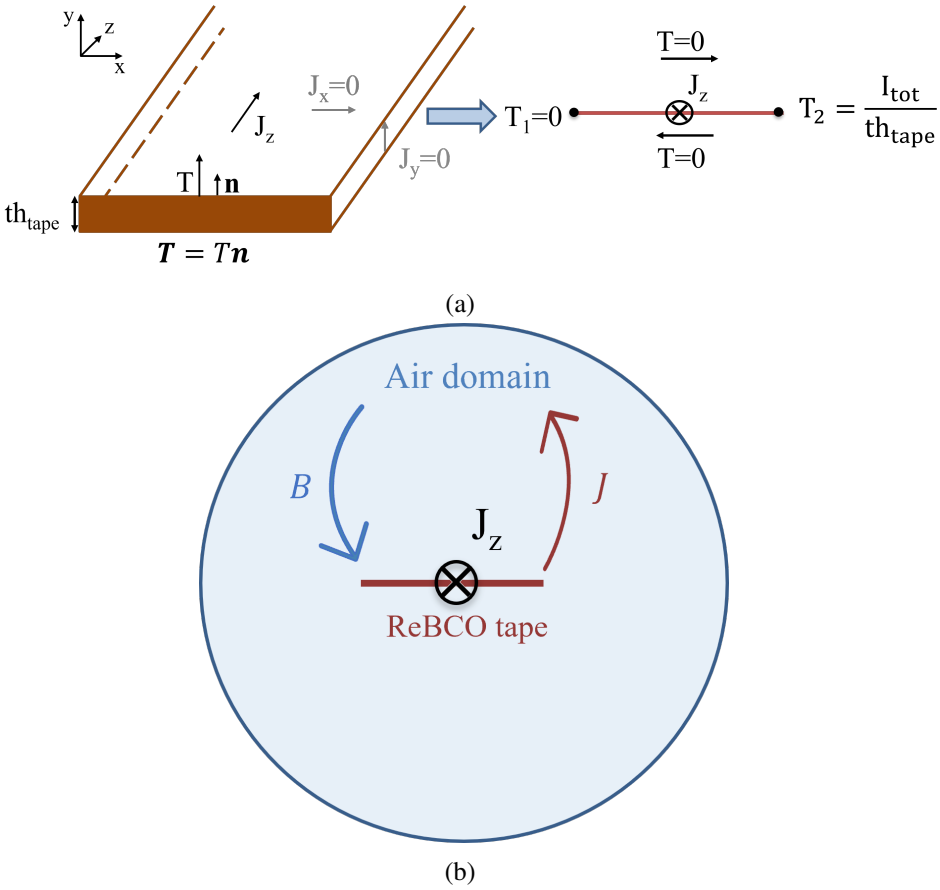

Fig. 3.1 (a) Sketch of thin approximation for T formulation and boundary condition in the case of transport current. T is always perpendicular to the tape surface, T_1 and T_2 are the values of T at the left and right edges, respectively, and th_{tape} is the tape thickness, ®2022 IEEE. Reprinted, with permission, from [2]. (b) Sketch of T-A formulation in 2D for a ReBCO tape assumed as thin shell.

Under the hypothesis of the uniform current density along the thickness and the width, the J_z is the only component considered:

$$J_z = \frac{\partial (T \cdot n_y)}{\partial x} - \frac{\partial (T \cdot n_x)}{\partial y} \tag{3.24}$$

A is defined over the entire computational domain, and the magnetic flux density **B** is computed as (3.9), and coupled with Ampere's law, the governing equation is (3.11). Finally, the governing equation, based on Faraday's law (3.3) is:

$$\nabla \times \left[\frac{1}{\sigma} \nabla \times T\mathbf{n} \right] \cdot \mathbf{n} = -\frac{\partial \mathbf{B}}{\partial t} \cdot \mathbf{n} \tag{3.25}$$

The model is fully coupled: the two variables **T** and **A** are solved simultaneously. **J** is the driver for the A formulation, while the variation of **B** with respect to time is the source in the T equation (3.25). In the T formulation, the transport current I on the tape is imposed through a Dirichlet boundary condition, obtained integrating the **J** over the tape cross-section **S** [158, 143]:

$$I = \int \mathbf{J} \cdot \mathrm{d}\mathbf{S} = \int (\nabla \times T\mathbf{n}) \cdot \mathrm{d}\mathbf{S} = (T_1 - T_2)\, th_{tape} \tag{3.26}$$

where T_1 and T_2 are the value of T on the HTS edges and th_{tape} is the tape thickness, see Fig. 3.1a.

$A - \phi$ formulation

An $A - \phi$ formulation is proposed in [173] based on the cell method [180], capable to deal with thin shell approximations and the strong non-linearity of the superconductor. The vector potential A is solved for the whole domain, while ϕ is described just for the conducting domain. The coupling ϕ and A requires to express the current through dual faces ~i in terms of ϕ and the magnetic flux through the dual faces b~ in terms of A.

3.2 Constitutive laws

The performance of a superconductor is determine by the steepness of the transition from the superconductive to the normal state, and it can be generally described as function of the critical current.

3.2.1 Power law and critical current density scaling

The strong non-linear behaviour of superconducting materials depends on the magnetic field, transport current and temperature, see Fig. 1.1 and strain. Numerically, the electrical field E is computed by a power law relationship:

$$E = E_c \left(\frac{|\mathbf{J}|}{J_c} \right)^N \tag{3.27}$$

where E_c is the electric field criterion, n is the exponent of the power law, $\mathbf{J}$ is the current density in the superconductor, and J_c is the critical current density. The E_c is conventionally set to 1 μV/cm, while the N is the exponent, which indicates the steepness of the characteristic, see Fig. 3.2, is usually given by the manufacturer or calibrated on the measurements, and for HTS material ranges from 25 to 35 [181] (and 40 to 50 for LTS [182]). Moreover, it is dependent on the temperature and on the magnetic field, but it is considered constant in the proposed model. The critical current density J_c is maximum current density a superconductor can carry, and it requires a proper scaling for modeling. This parameter is strongly related to operation conditions: considering J_{c0} the critical current density at 0 T and 0 K (usually given by the manufacturer), it degrades as effect of the temperature, the magnetic field and strain.

Magnetic field dependence

The most commonly used scalings of J_c are [183]:

- **Critical-state model**
  This is the most approximated where the critical current is supposed to be constant and equal to the one given by the manufacturer, and magnetic field

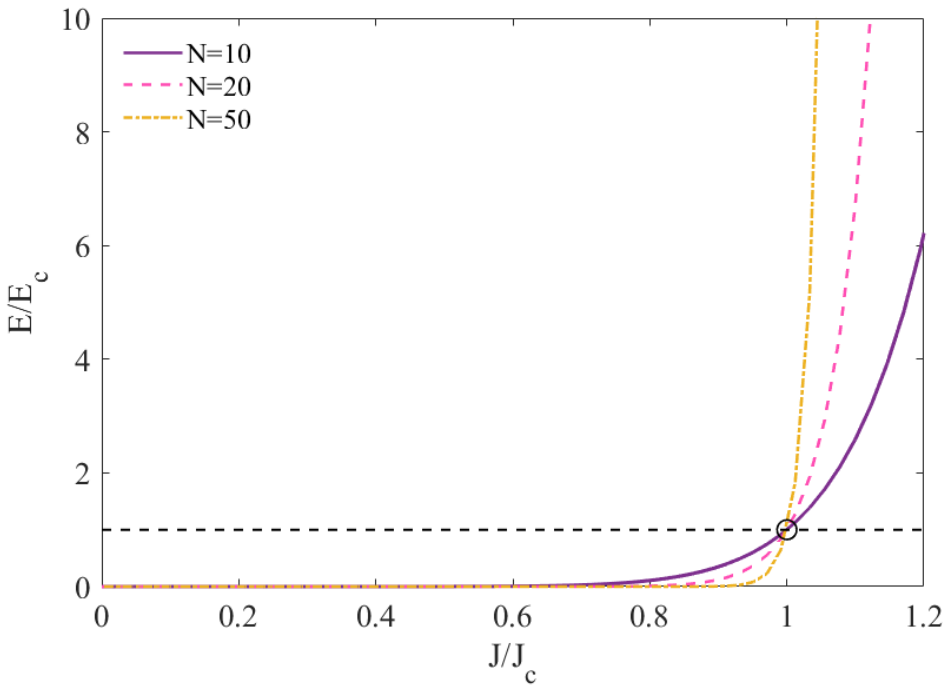

Fig. 3.2 Power Law at evaluate at different n-value. The higher the n-value, the steeper the curve, the higher performance of the conductor.

and temperature dependence are neglected [184].

$$J_c = J_{c0} \tag{3.28}$$

The main physics is captured by the model, but the homogeneity of the electric properties cannot be guarantee practically.

- **Kim model**
  The magnetic field degradation is considered as follow [82]:

$$J_c(B) = J_{c0} \frac{1}{\left(1 + \frac{|\mathbf{B}|}{B_0}\right)^m} \tag{3.29}$$

  Where the fitting parameters B_0 and α depends on the material and usually calibrated on V-I measurements [183], and $|\mathbf{B}|$ is the magnetic flux density experience in the superconductor.

- **Kim-like model**
  Taking into account the strong anisotropic properties of the HTS tapes, the Kim-like model considered explicitly the perpendicular $B_\perp$ and parallel $B_\parallel$ contribution to the tape surface as follow [185]:

$$J_c\left(B_\parallel, B_\perp\right) = J_{c0} \frac{1}{\left[1 + \frac{\sqrt{\left(kB_\parallel\right)^2 + B_\perp^2}}{B_c}\right]^b} \tag{3.30}$$

  Where the fitting parameters B_c, k, and b depends on the material and usually calibrated on V-I measurements.

- **Magneto-Angular anisotropy model**
  The anisotropic properties of HTS is expressed as an angular dependence [186]:

$$J_c(B, \chi_\omega) = J_{c0} \frac{1}{\left(1 + \chi_\omega \left(\frac{|\mathbf{B}|}{B_0}\right)^\beta\right)^p} \tag{3.31}$$

  where angular anisotropy factor χ is computed from the angle between the magnetic field and the tape surface ω as:

$$\chi_\omega = \sqrt{\gamma^{-1}(sin^2(\omega) + cos^2(\omega))} \tag{3.32}$$

The fitting parameters B_0, β, α, and electron mass anisotropy ratio γ are depending on the material.

Fig. 3.3 shows how the field penetration changes according the scaling laws: the critical state model is the most simplified and the Kim-like model the most conservative.

Temperature dependence

In order to avoid ambiguities with the current vector potential T, the temperature is identified as θ. The most common scaling for J_c:

- **Linear dependence**
  It is the most approximated, see Fig. 3.4, but it sufficiently reproduces the degradation due to the temperature rise:

$$J_c = J_{c0} \cdot \frac{\theta_c - \theta}{\theta_c - \theta_{op}} \tag{3.33}$$

  where θ_c is the critical temperature of the HTS material, θ is the actual temperature of the superconductor, and θ_{op} is the operational temperature of the application.

- **Associate to the pinning mechanism**
  According to [187] the temperature dependence of the J_c is associated to the pinning mechanism

$$J_c = J_{c0} \cdot \left(1 - \frac{\theta}{\theta_c}\right)^s \tag{3.34}$$

  where the characteristic exponent s varies from 1.9 to 2.6 in a magnetic-field range of $1-5$ T [188].

- **Exponential decrease**
  Other studies fitted from measurements an exponential scaling

$$J_c = J_{c0} \exp \frac{\theta}{\theta^*} \tag{3.35}$$

  where the $\theta*$ again related to the pinning mechanics [81]. θ^* may vary according to the manufacturer and the background magnetic field. This scaling

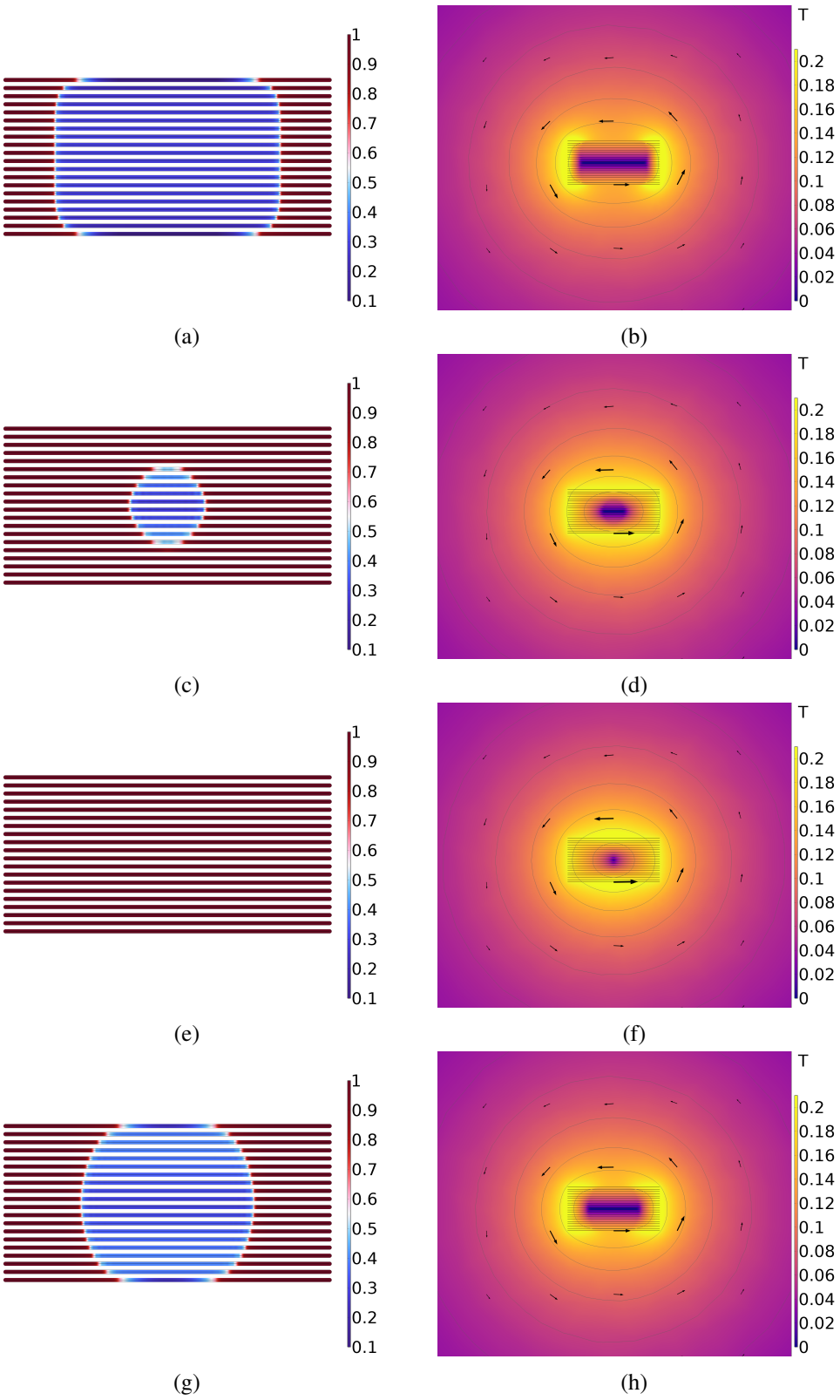

Fig. 3.3 Simplified 2D models for representation of I/I_c distribution in a 20-tapes stack and self-field generated according the critical state model (a)-(b), Kim model (c)-(d), Kim-like model (e)-(f) and the angular dependence model (g)-(h). Due to the *skin effect* current tends to concentrate on conductor edges, where the maximum transport current flows (I_c).

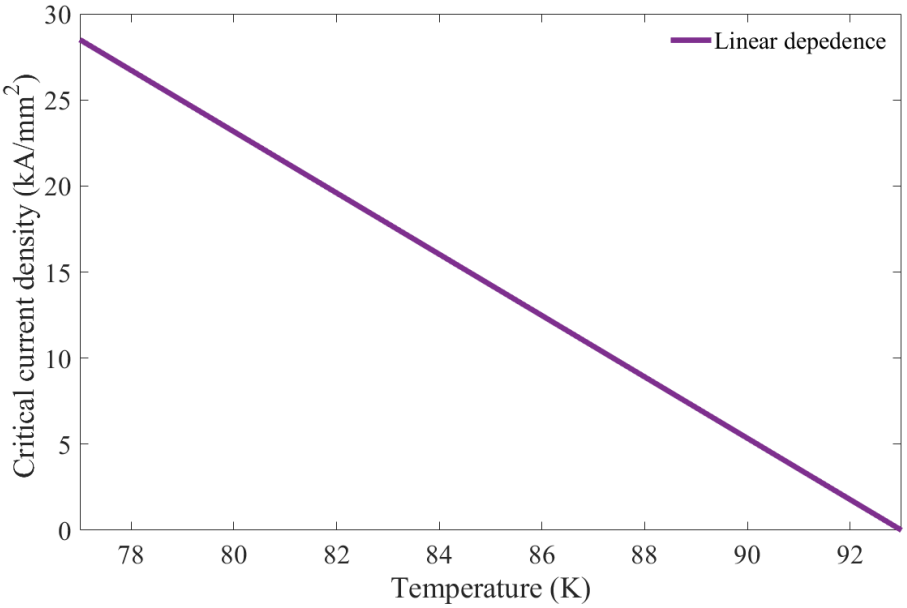

Fig. 3.4 Linear temperature dependence of the critical current density.

law, depending on the magnetic field orientation, holds up till 50 K. Thus, it's not applicable for our cases.

The scaling law affects the accuracy of the results with a significant impact on the convergence and computational cost of the simulations. Therefore, for the model proposed in Section 3.3, the Kim-like model (Eq. 3.30) for the magnetic field dependence, to be conservative, and the linear dependence on temperature (Eq. 3.33), since all simulations are carried at 77 K, have been implemented.

3.3 Development of a multiphysics model for ReBCO tapes and CORC® cables

In this section is devoted to the model developed in the framework of PhD activity. A multi-physics model for a CORC® wound with homogenized ReBCO tapes is proposed, see Fig. 3.5. It is based on $T-A$ formulation, leveraging the high aspect ratio of tapes, suitably coupled with a conduction thermal model which for the first time properly accounts for the cable convective cooling. The model can simulate the thermal, electric and magnetic behaviors and the current sharing among tapes

Table 3.1 YBCO layer material properties at 77 K from [190].

Material	λ (W/m/K)	ρ (kg/m^3)	C_p (J/kg/K)	σ (S/m)
YBCO	5.914	6,390	88.69	Eq. (3.27)
Silver	530.4	10,630	161.4	3.17×10^8
Copper	431.2	8,960	218.1	3.47×10^8
Hastelloy	7.801	8,890	163.5	8.40×10^5
Homog.	204.1	8,936	185.2	Eq. (3.41)

adopting a set of self-consistent boundary conditions, aiming to the critical current prediction. More informations about the model implementation are reported in APPENDIX A.

3.3.1 Tape homogenization

The HTS tape is a multilayer material characterized a extremely thin thickness (around few micrometers) and the width in the order of millimeters (some common dimensions are reported in Fig. 2.1). The YBCO coated conductor tapes are the ones considered in this study. They are characterized by a high critical temperature, $\theta_{c0} = 93$ K, and they are able to transport high current densities at very high fields. The superconductor layer (around $1-2$ μm) is coated by a copper stabilizer, and a metal substrate, made of Hastelloy, functiong as a mechanical support to axial and bending stresses. Due to the high aspect ratio of the tape, it can be assumed as a thin sheet, for which a proper homogenization is required. In this work, the thermo-physical properties of all materials are considered dependent on the residual resistivity ratio ($RRR \approx 40$ for SuperPower tapes [189]), which is an index of the purity of the material defined as the ratio between the resistivity at room temperature and that at 0 K (for any material) or at the transition temperature (for SC), and temperature. The thermo-physical properties of the tape, from [190] at 77 K are summarized in Table 3.1. In detail, the homogenization has been obtained weighting the density ρ with the cross section, while the specific heat at constant pressure c_p with the mass. The thermal conductivity λ is strongly anisotropic: along the direction parallel to the tape surface, thermal resistances are arranged in parallel, whereas along the perpendicular direction, resistances are arranged in series. Therefore, the equivalent thermal conductivities λ_{eq} and $\lambda_{\perp}$ are accordingly evaluated and weighted

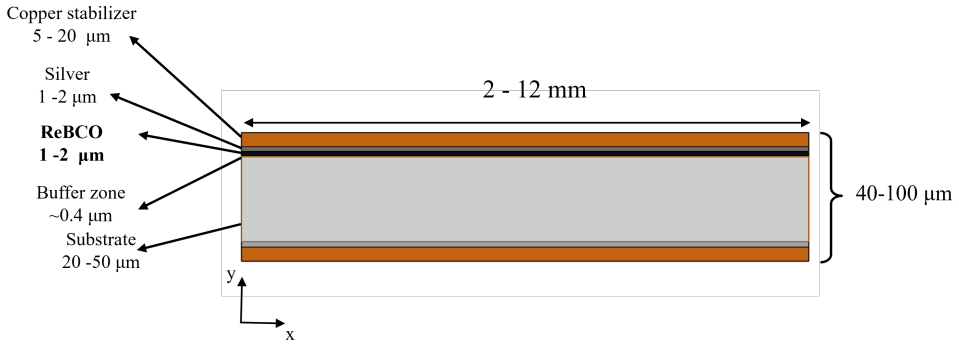

(a)

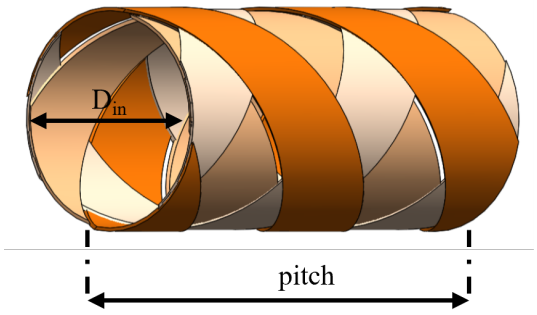

(b)

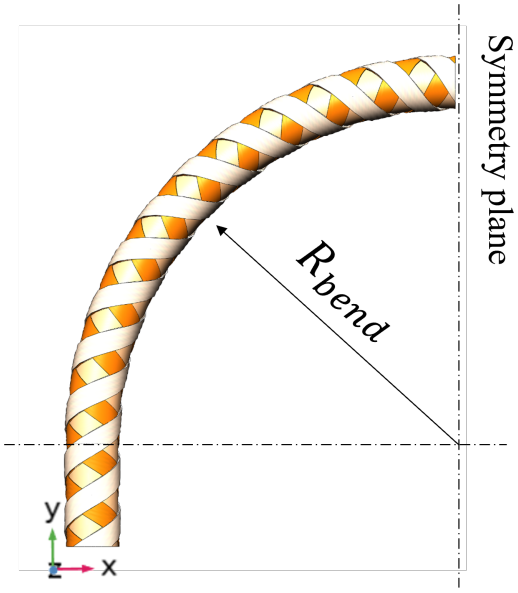

(c)

Fig. 3.5 (a) YBCO tape cross section and tape layers' thicknesses (not in scale). (b) Sketch of the straight CORC® cable investigated here (copper core not represented here) (both reproduced from ®2022 IEEE. Reprinted, with permission, from [2]). (c) Sketch of the bended CORC® cable investigated here (copper core not represented here), ®2024 IEEE. Reprinted, with permission, from [142].

on the cross section:

$$\lambda_{eq} = \frac{\sum_{i=1}^{N_l} \lambda_i A_i}{\sum_{i=1}^{N_l} A_i} \tag{3.36}$$

$$\frac{1}{\lambda_\perp} = \frac{\sum_{i=1}^{N_l} \frac{1}{\lambda_i} A_i}{\sum_{i=1}^{N_l} A_i} \tag{3.37}$$

where A is the cross section of the ith layer and N_l is the number of layers.
Regarding the electrical properties, the electrical conductivity σ of all but the YBCO layer, are temperature dependent, from [190], and the ones at 77 K are summarized in Table 3.1. For the SC layer, σ_{YBCO} is computed through the nonlinear power law, expressed in terms of electric conductivity:

$$\sigma_{YBCO} = \frac{J_c\left(B_\parallel, B_\perp, \theta\right)}{E_0} \left(\frac{|\mathbf{J}|}{J_c\left(B_\parallel, B_\perp, \theta\right)} \right)^{1-N} \tag{3.38}$$

where E_c is the critical field (conventionally set to 1 μV/cm, N is the exponent of the power law, and $\mathbf{J}$ is the current density in the superconductor. The critical current density J_c characterization is based on Kim-like model [183, 191], see Section 3.2.1, and it is dependent on the magnetic flux densities parallel, $B_\parallel$, and normal, $B_\perp$, to the tape surface and on temperature θ:

$$J_c\left(B_\parallel, B_\perp, \theta\right) = \psi \frac{I_{c0}}{A_{sc}} \frac{\theta_{c0} - \theta}{\theta_{c0} - \theta_{op}} \frac{1}{\left[1 + \frac{\sqrt{\left(kB_\parallel\right)^2 + B_\perp^2}}{B_c}\right]^b} \tag{3.39}$$

where I_{c0} is the critical current at zero-field applied, A_{sc} is the SC cross section, θ_{c0} is the critical temperature at zero applied field, θ_0 is nominal operating temperature, θ is the actual tape temperature. k, B_c and b are fitting parameters that allow to weight the contributions due to θ, $B_\parallel$ and $B_\perp$. ψ represents the critical current density degradation expressed as I_c/I_{c0} due to the strain which the tape is subject to. Conservatively, the maximum compression strain in % along the the YBCO tape width wound on the core can be evaluated, from [42], as follows:

$$\varepsilon_{max} = \frac{-th_{sub}}{th_{sub} + d_{core} + 2th_{cu}} \tag{3.40}$$

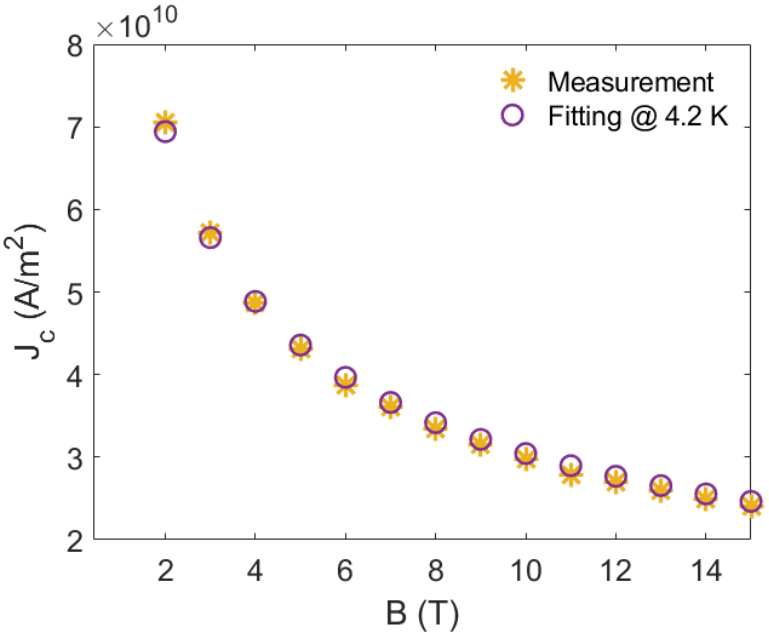

Fig. 3.6 Critical current density fitted vs experimental data.

where th_{sub} is the substrate thickness, d_{core} is the copper core diameter and th_{cu} is the copper layer thickness. The strain is evaluated on the mid plane of the tape. From [42], the degradation due to the winding is extrapolated from the graph in Fig. 3.8. The scaling of the critical current density, evaluated as expressed in (3.39), has been computed by best-fitting the parameters β, k, B_c and b to the measurement data at LBNL on a 8 mm-long tape [192], see Fig. 3.6). All other parameters are reported in Table 3.2.

Finally, the homogenization of the tape electrical properties has been achieved considering the electric parallel among layers, defining an equivalent electrical conductivity σ_{eq}, weighted on cross sections:

$$\sigma_{eq} = \frac{\sum_{i=1}^{N_l} \sigma_i A_i}{\sum_{i=1}^{N_l} A_i} \tag{3.41}$$

where σ_i is the electrical conductivity of the ith layer.

Note that the buffer zone has been neglected in the homogenization of tape materials, because the material is nonconducting.

Table 3.2 J_c characterization: fitting parameters for a single tape.

Parameters	Value		Units
θ_{op}	4.2	77	K
I_{c0}	2197	85	A
θ_{c0}	93		K
β	1		–
k	0.275		–
B_c	100		mT
b	0.525	0.25	–
ψ	see Fig. 3.8		–

3.3.2 Electromagnetic model

The T formulation has been properly implemented for the conducting domain in COMSOL Multiphysics® through *General Form Boundary PDE* module, while for the A formulation, the built-in *Magnetic Fields* module has been exploited using finite elements.

Current sharing condition

The state-of-art of numerical models devoted to the computation of the current distribution on CORC® cables is reported in Section 2.2.5. The current distribution and re-distribution in the cable is guaranteed imposing a new boundary condition, that we'd called the *current sharing condition*, is proposed in the strong form: among two subsequent boundaries, the current vector potential **T** to be uniform and equal. The model capability to compute and redistribute the current without any external circuital network, according to possible disturbance or defect on each tape (i.e., hot spot temperature or electromagnetic difference) is the the main novelty of the work. In case of multiple tapes, to guarantee the correct current split among the tapes, the vector potential T is imposed to be 0 along the first boundary, equal to the total current I_{tot} along the last boundary, and to be uniform and equal among two subsequent boundaries, see Fig. 3.7 and in APPENDIX A. The uniformity along the edge guarantees that no current would leak from that edge, while the equality

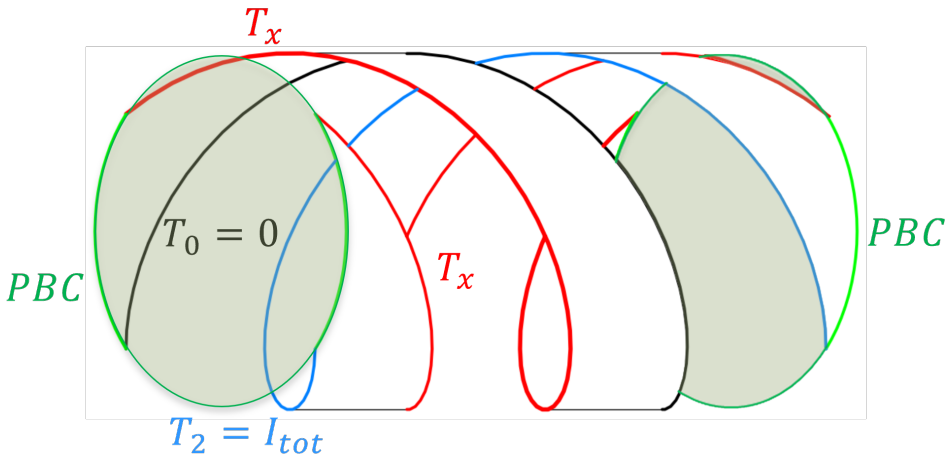

Fig. 3.7 Sketch of the boundary conditions on 2 tapes CORC® : periodic boundary conditions (PBC) are highlighted in green, and in red the new boundary condition is presented. In the first boundary, T has been set equal to zero as a reference, and the total current is imposed in the last boundary (blue line), ®2022 IEEE. Reprinted, with permission, from [2].

is required to fulfill (3.26) including all tapes. When a CORC® cable is modelled, to exploit the minimum computational domain, just a pitch has been simulated and proper periodic boundary conditions are imposed, both in the SC and air domains, to avoid edge-effects, see Fig. 3.7. In presence of an external magnetic field $\mathbf{B}_{app}$, it is applied as a boundary condition on the air domain: a suitable impressed magnetic vector potential $\mathbf{A}_{app}$, whose curl provides the three components of $\mathbf{B}_{app}$, (3.9), is imposed on the boundary edges of the computational domain.

3.3.3 Thermal model

The energy conservation law is solved only for the SC domain:

$$\rho_{eq} c_{eq} \frac{\partial \theta}{\partial t} = -\nabla \cdot \left(\lambda_{eq}(\theta) \nabla \theta \right) + \dot{q}(\theta) \tag{3.42}$$

where θ is the temperature, ρ_{eq} is the homogenized density, C_{eq} is the homogenized specific heat, λ_{eq} is the homogenized thermal conductivity along the parallel direction (see (3.36)), and finally $\dot{q}$ is the source term (see next sections for details). The solution has been obtained using the built-in *Heat Transfer in Shells* COMSOL module. The application of CORC® cables has been considered in a cryogenic bath:

Table 3.3 Liquid nitrogen properties at 77 K from NIST.

Parameters	Value	Units
β_f	0.013	$1/\mathrm{K}$
λ_f	0.147	$\mathrm{W/m/K}$
ρ_f	809.9	$\mathrm{kg/m^3}$
$C_{p,f}$	2030	$\mathrm{J/kg/K}$
ν_f	2.04	$\mathrm{m^2/s}$
α_f	8.91×10^{-8}	$\mathrm{m^2/s}$

the fluid is not simulated here, but the convective heat transfer is taken into account through an external heat sink.

Single tape

For the single tape model, the source term is given by the sum of two contributions:

$$\dot{q}(\theta) = \dot{q}_j + \dot{q}_f(\theta) \tag{3.43}$$

where $\dot{q}_j$ is the dissipated power by Joule effect and $\dot{q}_f$ is the cooling power due to the liquid nitrogen bath. The Joule power is computed considering the equivalent conductivity:

$$\dot{q}_j = \frac{|J|^2}{\sigma_{eq}} \tag{3.44}$$

Where J is the current flowing in the SC domain. The heat sink due to the refrigeration is computed as:

$$\dot{q}_f(\theta) = \frac{h_f A_{wet}\left(\theta_f - \theta\right)}{V_t} \tag{3.45}$$

where A_{wet} is the tape wetted area (equal to the tape surface), V_t is the tape volume, θ_f is the bath temperature, and θ is the actual tape temperature. The heat transfer coefficient h_f is evaluated starting from Nusselt number Nu, the tape characteristic length L_c and nitrogen thermal conductivity λ_f:

$$h_f = \frac{\lambda_f Nu}{L_c} \tag{3.46}$$

The Nusselt number has been computed through a proper correlation for horizontal plate in free convection for laminar flows from Rayleigh number [193]:

$$Nu = 0.54\,Ra^{\frac{1}{4}} \tag{3.47}$$

The Rayleigh number Ra is given as:

$$Ra = \frac{g\beta_f\,(\theta - \theta_\infty)\,L_c^3}{\nu_f \alpha_f} \tag{3.48}$$

where g is the gravity acceleration, β_f is the volumetric thermal expansion coefficient, ν_f is the dynamic viscosity, α_f is the thermal diffusivity, θ_∞ is the environment temperature (equal to the bath temperature), θ is the tape temperature, and L_c is the characteristic length of the geometry (defined as the ratio between the heat transfer area and the perimeter of the geometry). The pedix f is referred to the refrigerant fluid.

CORC® cable

For the CORC® model, the source term has one more contribution:

$$\dot{q} = \dot{q}_j + \dot{q}_f + \dot{q}_l \tag{3.49}$$

where $\dot{q}_l$ is the conductive contribution among adjacent layers computed as:

$$\dot{q}_l = \frac{\lambda_\perp}{\delta}\left(\bar{\theta}_i - \bar{\theta}_j\right)\frac{A_{contact}}{V_t} \tag{3.50}$$

where $\lambda_\perp$ is the homogenized transversal thermal conductivity (see Eq. (3.37)), δ and $A_{contact}$ are the distance and the contact area between two adjacent layers, respectively, $\bar{\theta}_i$ and $\bar{\theta}_i$ are mean temperature of the layers i and j (with $i \neq j$). The Joule effect and the cooling power are evaluated as reported in the previous section, but the Nusselt number has a different form: the cable has been approximated as a long horizontal cylinder and Nu is depending on the Rayleigh number Ra and in the

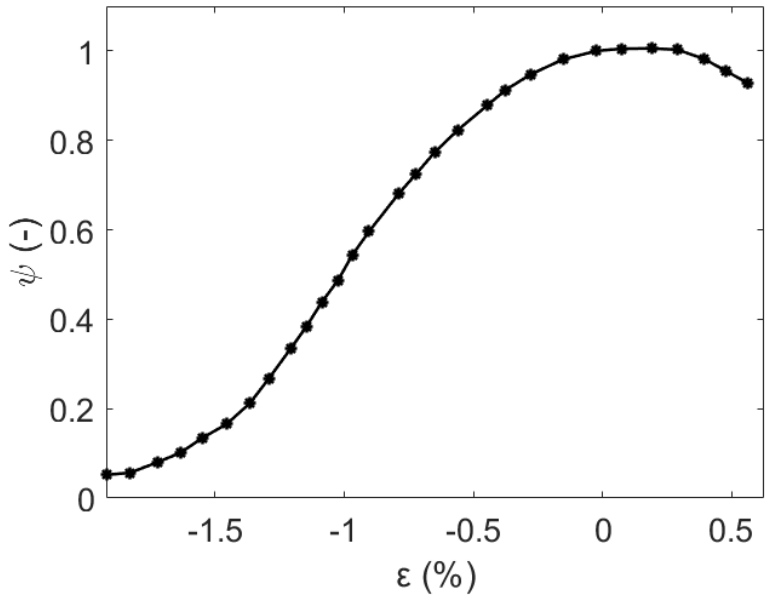

Fig. 3.8 Critical current degradation ψ with respect to strain ε for YBCO tape in the midplane from [42], ®2022 IEEE. Reprinted, with permission, from [2].

Prandtl number Pr [193] as follows:

$$Nu = \left(0.6 + \frac{0.387\, Ra^{\frac{1}{6}}}{\left[1 + \left(\frac{0.559}{Pr} \right)^{\frac{9}{16}} \right]^{\frac{8}{27}}} \right)^2 \tag{3.51}$$

3.3.4 Mechanical consideration

The mechanical strain can significantly degrade the CORC® performances [42, 109, 194], since the ReBCO is strain-sensitive. From [42], the ψ degradation factor can be extrapolate from Fig. 3.8, once the strain is computed (see 3.3.4), and scaled the J_c accordingly:

$$J_c = \psi J_{c0} \tag{3.52}$$

For a general characterization of the critical current density, the electromagnetic models can be coupled along with the thermal, to obtain a comprehensive scaling as a function of the operating conditions of B and θ [81, 195, 196], see (3.39) in

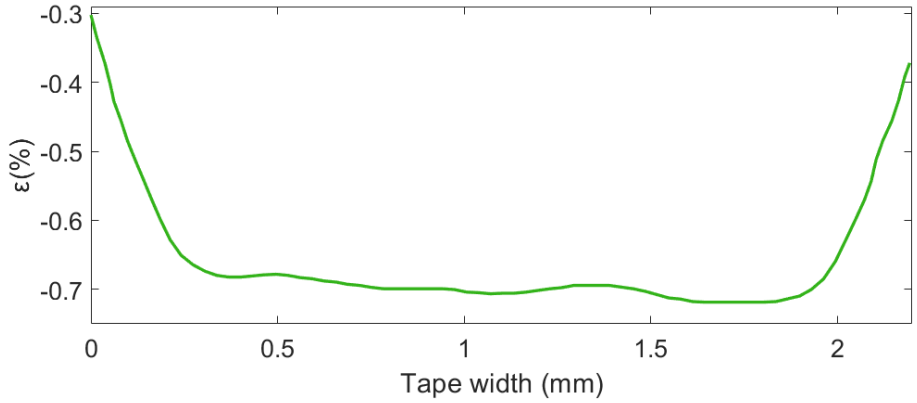

Fig. 3.9 Intrinsic strain distribution of the tape from [165] and final total distributions along the width at the cable center cross section.

3.3.1. The state-of-art of numerical models for the evaluation of mechanical state in CORC® cables is reported in Section 2.2.5. The current was imposed without any possibility of redistributing, if necessary, due to uneven strain in different tapes. In this work, a simplified evaluation of the strain, based on pure geometrical assumptions, is proposed. The strain map allows to determine the I_c degradation due to the deformation in each element of the computational domain. The map of strain has been extrapolated both from literature, when possible, and from some computed starting from definition of strain (the ratio among the elongation ΔL and the initial length L_0). Three strain contributions have been considered:

- intrinsic strain due to the winding of the tape on the copper core ε_w;
- strain due to the bending ε_b;
- shrinkage of the tape due to the bending ε_s.

Curvilinear coordinates have been adopted to respect the helical pattern of the twisting tapes and to proper compute the strain along the CORC® , see APPENDIX A.

Winding of an individual tape

In the CORC® cable design, tapes are helically wound around the central copper core inducing local deformation. The ReBCO layer is above the neutral plane, so it

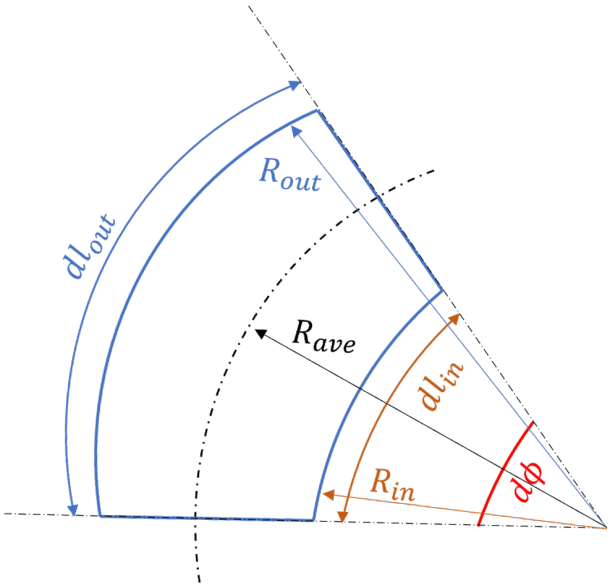

Fig. 3.10 Sketch of an element after bending, for analytical strain evaluation.

will be in compression state [121]. The non-uniform longitudinal strain distribution along the width ε_w, computed in [165], has been imposed on each tape, see Fig. 3.9.

Cable bending

After the bending process, part of the cable above the neutral radius R_{ave} is in tension state, while the one below it is in compression (see Fig. 3.11a). Based on strain definition:

$$\varepsilon = \frac{\Delta L}{L_0} \tag{3.53}$$

$$\varepsilon_{out} = \frac{R_{out} - R_{ave}}{R_{ave}} \tag{3.54}$$

$$\varepsilon_{in} = \frac{R_{in} - R_{ave}}{R_{ave}} \tag{3.55}$$

where subscripts *out* and *in* are referred to the part above and below the neutral radius, respectively. Generalizing, the strain along all the cable is computed as:

$$\varepsilon_b = \frac{R - R_{ave}}{R_{ave}} \tag{3.56}$$

Where R is the cylindrical coordinate, see Fig. 3.10.

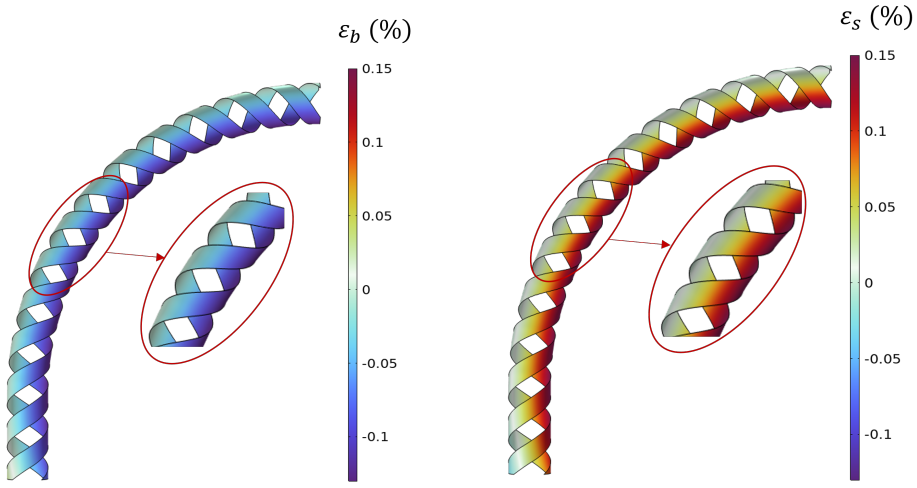

(a) (b)

Fig. 3.11 (a) Tension-compression strain map and (b) shrinkage strain map due to the bending process, ®2022 IEEE. Reprinted, with permission, from [142].

Tape shrinkage due to bending

The tension state led to a shrinkage of the tape, that has been considered in this study, see Fig. 3.11b. Based on the volume conservation, the final thickness is computed as:

$$V_{tape} = R_{ave}^2 \cdot \phi \cdot th \tag{3.57}$$

$$th_{fin} = \frac{V_{tape}}{R_{ave} \cdot R \cdot \phi} \tag{3.58}$$

Where V_{tape} is the tape volume, ϕ is the angular coordinate of the cylindrical system (see Fig. 3.10), th is the thickness, and the subscript $_{fin}$ is referred to after bending process. Therefore, the strain ε_s is:

$$\varepsilon_s = \frac{th_{fin} - th_{init}}{th_{init}} \tag{3.59}$$

Where th_{init} is the initial thickness of the tape.

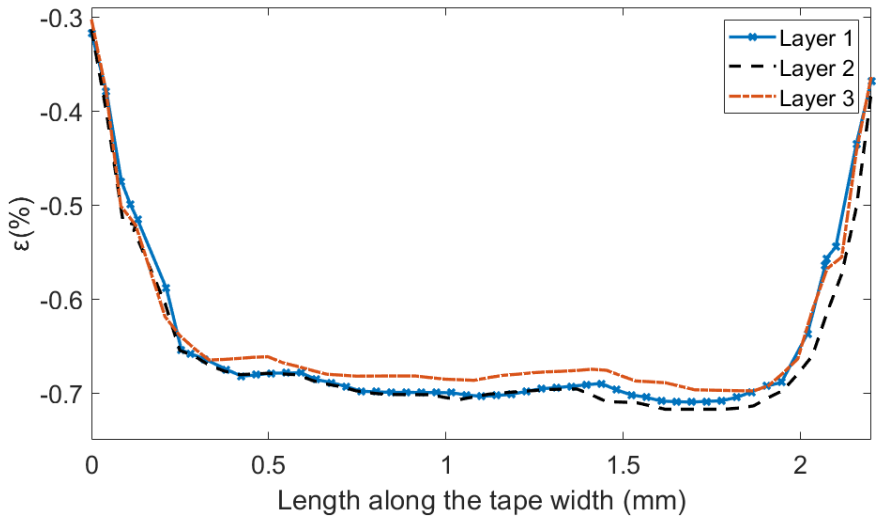

Fig. 3.12 Total strain distribution along the tape width on the three layers.

Total strain

The total strain ε is computed by the superposition principle:

$$\varepsilon_{tot} = \varepsilon_w + \varepsilon_b + \varepsilon_s \tag{3.60}$$

Fig. 3.9 shows the strain distribution along the tape width of the three layers. Fig. 3.13a and Fig. 3.13b report the total strain map and distribution along the tape edges. From Fig. 3.13b, it possible to notice the increase of the average strain value from the straight part of the cable to the bended one, and the periodic behaviour among subsequent pitches. The percentage of degradation $\psi(\varepsilon)$ of the tape critical current density due to the strain state has been extrapolated from [42].

3.3.5 Element order

From literature has been stated that the element order of the utilized bases function for the finite element, the discretization of the A-domain should always be one order higher than that of T-domain [197]. In [198] and [199] it is reported that, under sub-critical region, some oscillations can occur in the computed current density J, with first or second order Lagrange elements for both T and A. Therefore, all simulations have been carried out using first order linear element for the T formulation and

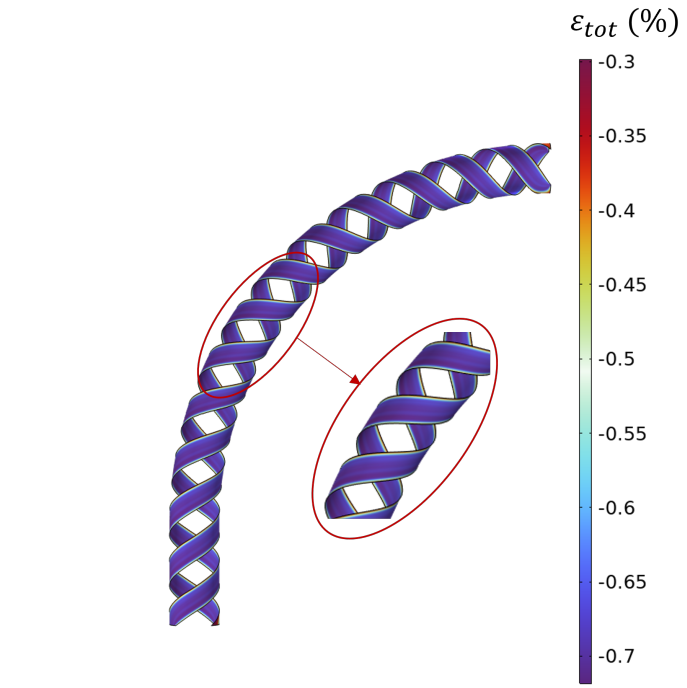

(a)

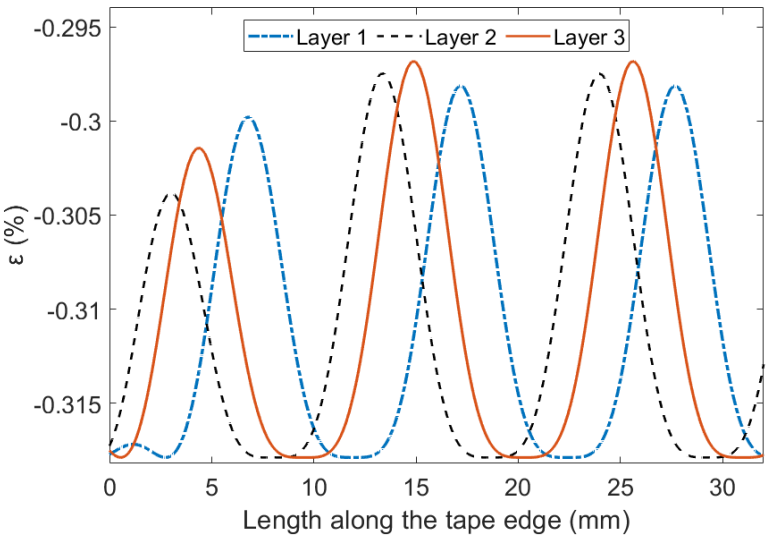

(b)

Fig. 3.13 (a) Total strain map. (b) Total strain distributions along the first 32 mm of the tape edges (3 subsequent pitches), ®2022 IEEE. Reprinted, with permission, from [142].

second order quadratic element for the A formulation. Quadratic elements have been also used for the thermal module. The problem is fully coupled, therefore coupling effects and losses are automatically taken into account by the COMSOL.

Chapter 4

Model verification and validation

This section is devoted to the verification and validation of the model illustrated in Section 3.3. Portions of the present chapter were already published in the following scientific papers:

- S. Viarengo, L. Brouwer, P. Ferracin, F. Freschi, N.Riva, L. Savoldi, X. Wang, "A New Coupled Electrodynamic T – A and Thermal Model for the Critical Current Characterization of High-Temperature Superconducting Tapes and Cables," in IEEE Access, vol. 11, pp. 107548-107561, 2023, doi: 10.1109/ACCESS.2023.3321194, [2];
- C. Messe, N. Riva, S. Viarengo, G. Giard, and F. Sirois, "Belfem: a special purpose finite element code for the magnetodynamic modeling of high-temperature superconducting tapes", Superconductor Science and Technology, vol. 36, Nov. 2023, [172];
- S. Viarengo, F. Freschi and L. Savoldi, "CORC Cables: Numerical Characterization of the Critical Current After Bending," in IEEE Transactions on Applied Superconductivity, vol. 34, no. 5, pp. 1-5, Aug. 2024, Art no. 4801605, doi: 10.1109/TASC.2023.334809, [142].

A step-by-step approach has been followed: the 3D single tape model has been verified and benchmarked against the 2D magnetostatic model 3.1.1 and measurements. The same model has been used for the prediction of the electric field-current ($E-I$) curves at different external magnetic fields, perpendicularly applied

Table 4.1 AC conditions for a single tape: set of simulations.

Model	AC transport current	AC background field
$T-A$ formulation	x	x
H formulation	x	x
$A-H$ formulation	x	-
$H-A$ts* formulation	x	-

*ts means *thin sheets.*

Table 4.2 DC condition and $V-I$ curves: Test cases and set of simulations.

Model	Single tape	2-tapes	6-tapes	12-tapes	Bended
$T-A$ formulation	x	x	x	x	x
H formulation	-	x	-	-	-
2D magnetostatic	x	-	-	-	-
Measurements	x	-	x	x	x

to the tape surface. Extending the model to CORC® cables, a 2-tapes (1 layer) CORC® subject to the thermal perturbation has been simulated and crosschecked with the $H-$formulation 3.1.2. Finally, a computed $V-I$ curve of 6-tapes CORC® (3 layers) and 12-tapes CORC® (6 layers) are compared with experimental data. The critical current degradation and the entire $V-I$ are mainly affected by strain distribution, the self-field and the termination resistances: this model would replicate those effects to reproduce and predict cables behavior. A first test-case of a bended 6-tapes CORC® has been also explored. The set of tests cases is summarized in Table 4.2. The single tape model tested the model capability to deal with the strong non-linearity of the problem. The 2D tape model has been benchmark both in AC and DC conditions. Then, the 2D and a full 3D tape model had been exploited for the characterization of the critical current in DC conditions with respect the 2D magnetostatic model and the measurements from LBNL.

4.1 Single tape model: benchmark in AC

This section is dedicated to the AC benchmarks of the proposed $T-A$ model with H-formulation, $H-A$ formulation and $H-A$ thin shell formulation, for a single tape. The benchmarks tackle single tape under applied alternating current and field

Table 4.3 Material properties for the AC condition benchmarks.

Parameter	Value	Units
J_c	47.5	kA/mm^2
E_c	1	-
n-value	35	-

to compared the current distribution and the heat losses. In case of transport current, the predicted heat loads have also been compared to the well-established analytic model of Norris [200]. In COMSOL, H and $A-H$ formulations and the recently developed thin-shell $A-H$ formulation [201]. A tape geometry with a width of 4 mm and a thickness of 1 μm has been studied. Based on the material properties in [96], an $I_c = 190$ A at 77 K considered, see Table 4.3. For sake of simplicity, the critical state model has been assumed (no temperature or field dependence on J_c), see Section 3.2.1. Those simulations also had the purpose of validation and comparison for a new finite element code for the magnetodynamic modeling of high temperature superconducting tapes based on $H-\phi$-formulation with thin-shell simplification: the Berkeley Lab Finite Element Framework (BELFEM), [172].

4.1.1 Simulation set-up

In the first benchmark, the tape is subjected at a sinusoidal alternating currents varying from 60 to 180 A at a frequency of $f = 50$ K for one period ($P = 1/f =$ 20 ms). The second benchmark for the single tape consists on the application of a sinusoidal magnetic field ranging from 3.5 mT to 52.5 mT, perpendicular to the tape surface.

4.1.2 Meshes

The 1D tape domain is immersed in a 2D air domain of 6 cm radius, see Fig. 4.1. The tape has 160 nodes, more dense towards the edges to catch well the field penetration (skin effect), while the air domain is discretized with unstructured triangular mesh for a total number of $\approx 12.5k$ of Degrees of Freedom (DoFs). The entire simulation runs in ≈ 30 min.

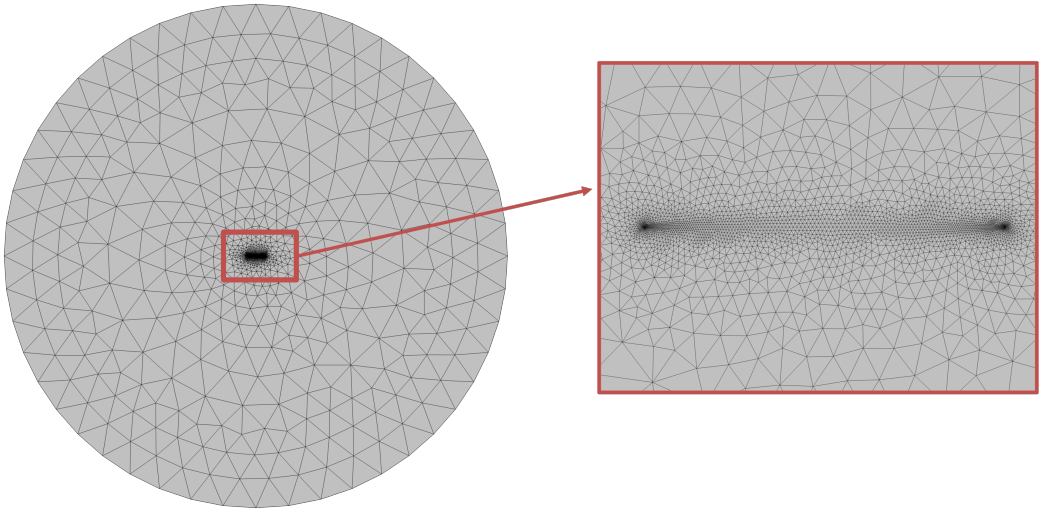

Fig. 4.1 Illustration of the 2D meshed air domain and 1D tape mesh used for the solution in COMSOL for the tape model in AC conditions solved by the $T-A$ formulation.

4.1.3 Results

The current distributions for $I = 60$ A and $I = 140$ A at 5 ms and 15 ms (at $1/4$ and $3/4$ of the period, respectively). The model shows good agreement with all the other formulation, except for a smaller overestimation of the skin effect on the edges of the tapes in high current. The heat loss Q per cycle are computed as:

$$Q = 2\int_{\frac{P}{2}}^{P}\int_{V} E \cdot J \mathrm{d}V \mathrm{d}t \tag{4.1}$$

Expressed in $J/m/cycle$. The $T-A$ solution is in very good agreement with references, see Fig. 4.3. The $T-A$ model has an average error of 1.1% with analytic solution of Norris model: the losses are slightly overestimated at higher current. Fig. 4.4 shows the current distribution along the tape width for a magnetic field amplitude of 7 mT and 42 mT at 5 ms and 15 ms (at $1/4$ and $3/4$ of the period, respectively). The $T-A$ is compared to the H-formulation. The current is polarized and denser along the edges (where the ratio $I/I_c = \pm 1$). Moreover, the higher the magnetic field, the higher penetration depth on the tape width. At higher frequency, the $T-A$ has some oscillations, but the average behavior is well captured.

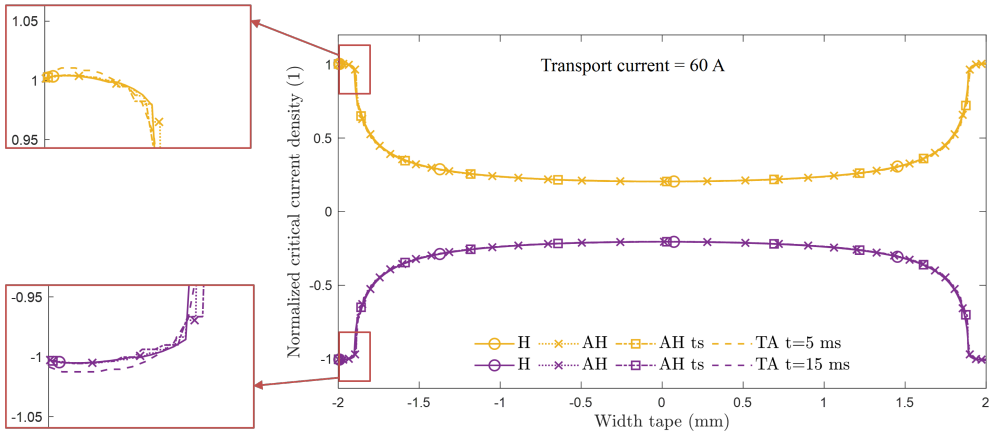

(a)

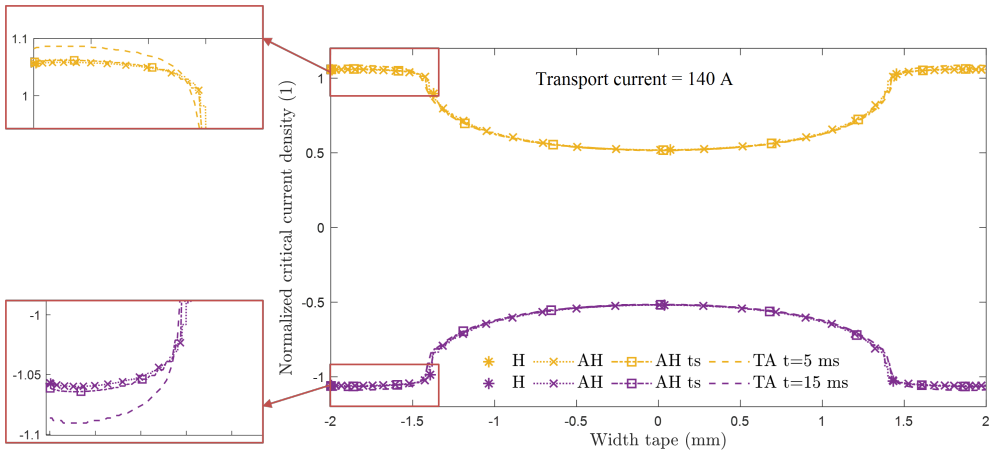

(b)

Fig. 4.2 Current distribution on single tape in AC-case study under a sinusoidal transport current of (a) 60 A and (b) 140 A. The yellow curves are related to time equal to 5 ms and the violet curve to 15 ms. The insert shows a smaller overestimation of the $T-A$ on the edges of the tapes in high current.

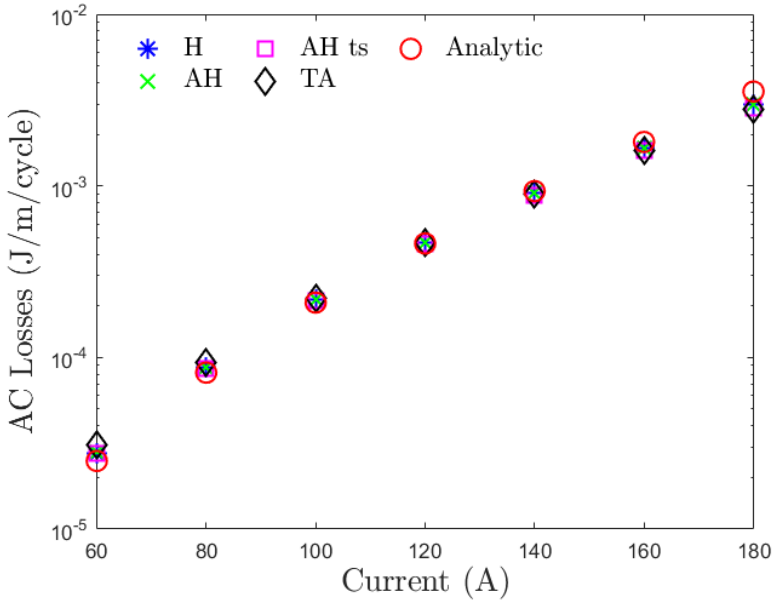

Fig. 4.3 Comparison of the AC losses of the 4 formulations and the Norris analytical formulae.

Table 4.4 Tape thicknesses for $V-I$ curve prediction of single tape model.

Layer	Thickness	Units
YBCO	1.6	μm
Silver	1.6	μm
Copper	20	μm
Hastelloy	50	μm
Tape	95.2	μm

4.2 Single tape model: V-I prediction

A fully 3D model has been used for a straight 8 mm-long and 4 mm-wide tape [192], and validated with measurements. The problem has translational symmetry and can suitably be studied with a 2D model. The 3D model, necessary for more complex geometries like the CORC® configuration, is here used to verify the capability of reproducing the 2D results. The model has been first verified through a grid independence, and then I_c values have been compared to the 2D magnetostatic model. Table 4.4 reports the geometric parameter of the SC tape.

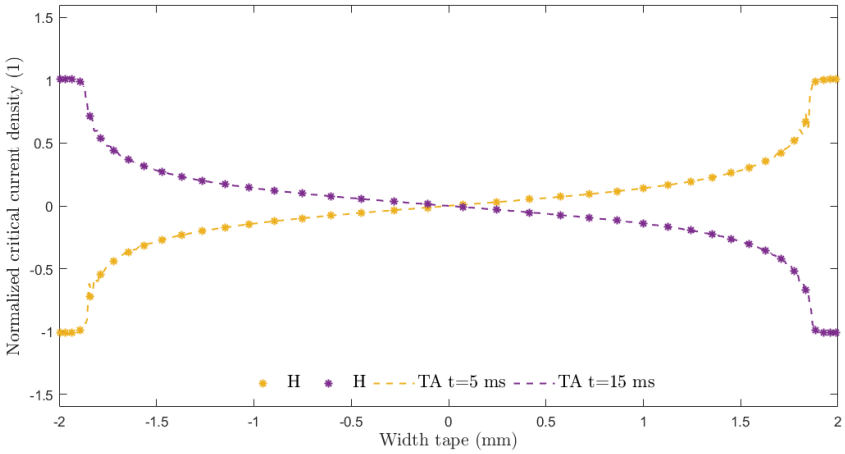

(a)

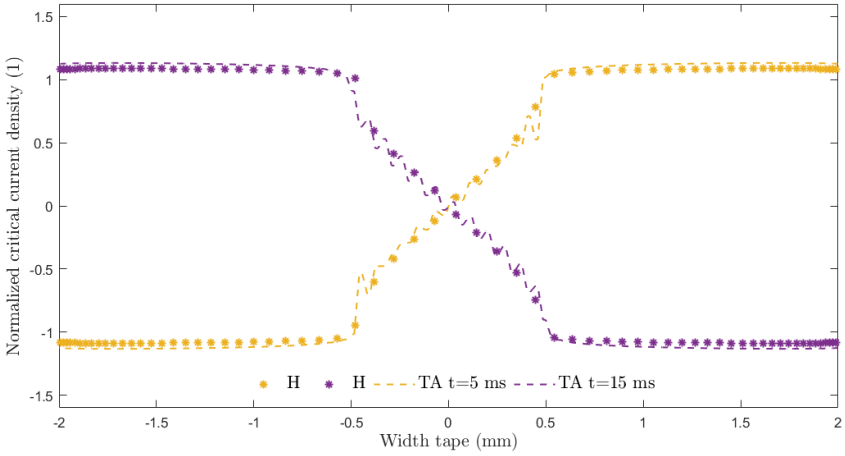

(b)

Fig. 4.4 Current distribution on single tape in AC-case study under a sinusoidal magnetic field of a) 7 mT and b) 42 mT . The yellow curves are related to time equal to 5 ms and the violet curve to 15 ms.

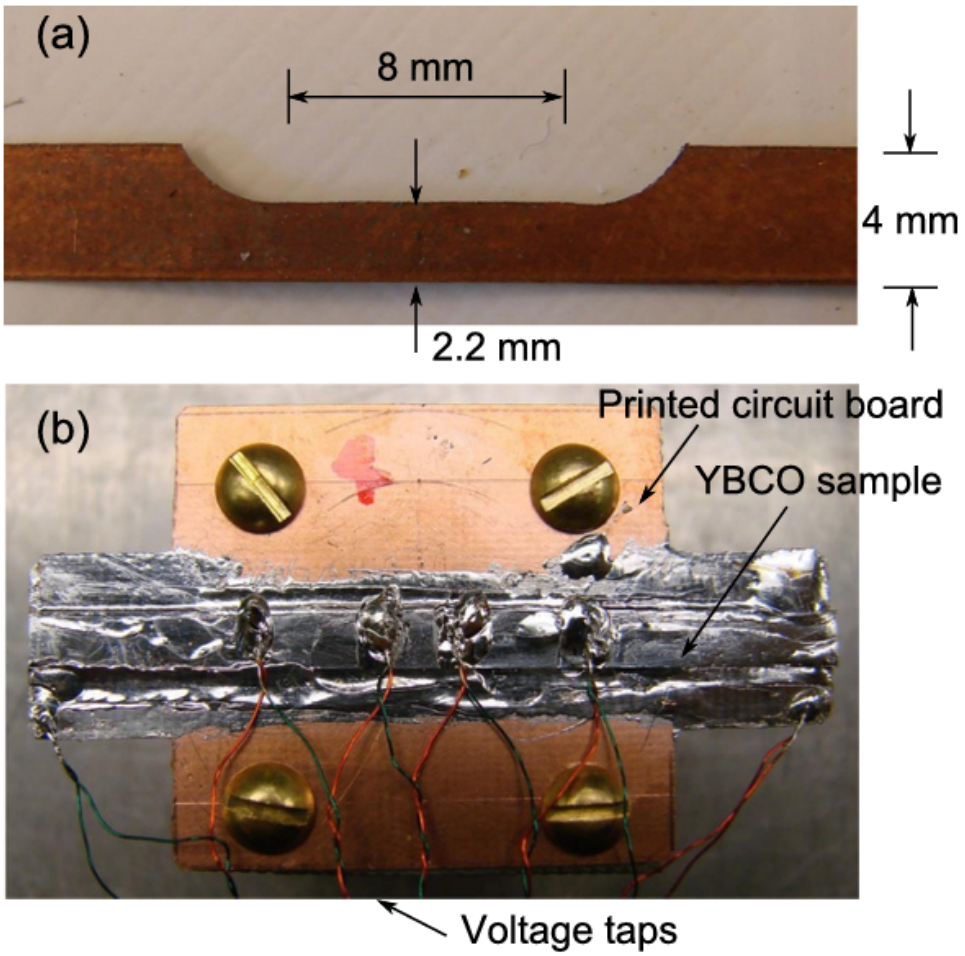

Fig. 4.5 Single tape experimental set-up for $V - I$ curve measurements in LBNL from [192]. All Rights Reserved.

4.2.1 Experimental set-up

A YBCO tape has been tested in the bath a liquid helium at 4.2 K and in a liquid nitrogen bath at 77 K. The sample has been soldered to a printed circuit board and the voltage has been measured using voltage taps at a distance of 5 mm (more details in [192]), see Fig. 4.5.

4.2.2 Simulation set-up

The current is ramped up in 0.1 s and then wait for the stationary conditions, reproducing the experiments. The initial temperature condition is set a 77 K, the bath

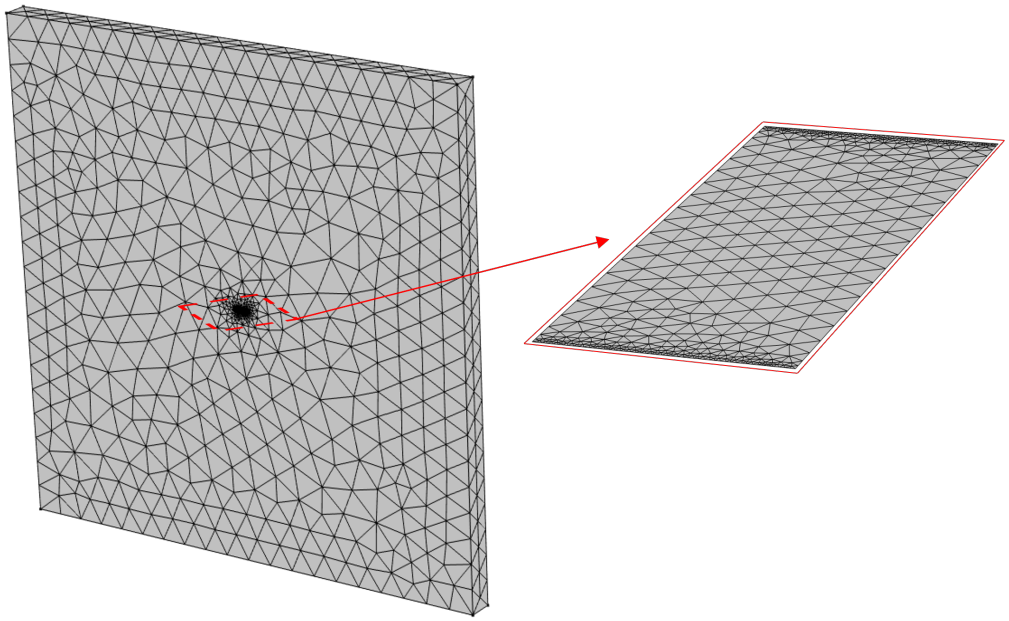

Fig. 4.6 Illustration of the 3D meshed air and tape domains used for the solution in COMSOL for the tape model solved by the $T-A$ formulation, ®2022 IEEE. Reprinted, with permission, from [2].

temperature. Then, the voltage is computed as the line integral of the electric field along the tape length.

4.2.3 Meshes

The mesh of the 2D air domain, is triangular and a distribution of 100 nodes is guaranteed in the tape for the magnetostatic model. The mesh counts 8200 elements. The 3D mesh for the $T-A$ model tape counts 10100 tetrahedral elements for the air domain and 2700 triangles for the tape, see Fig. 4.6. The $T-A$ model has been preliminary verified through a sensitivity mesh analysis. The node distribution on the tape domain has been parametrically refined from 10 nodes till 250, and the I_c and the temperature gradient $\Delta\theta$ has been observed till reaching a plateau trend. In Fig. 4.7, the I_c and the $\Delta\theta$ variations are reported as a function of the nodes on the tape edge. For both quantity, the selected grid is proved to provide values already in the asymptotic regime.

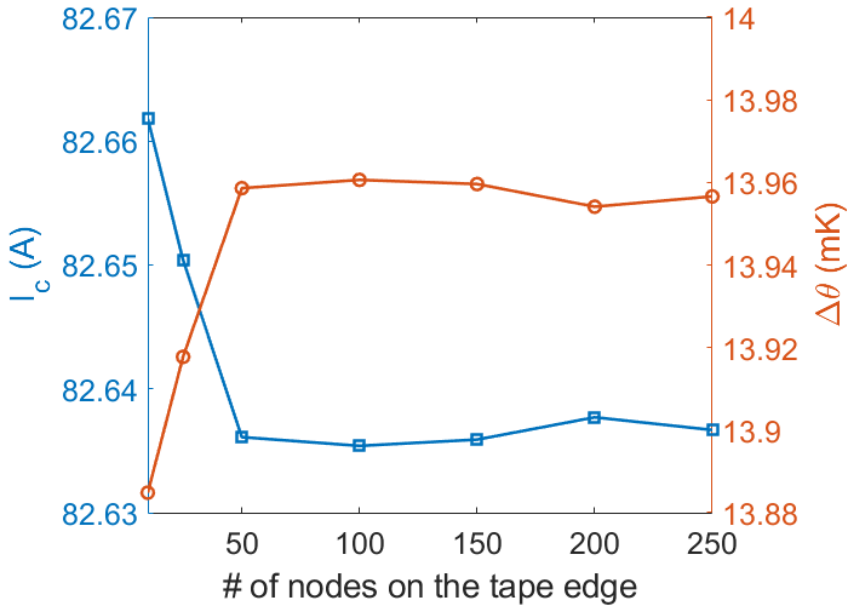

Fig. 4.7 Blue line with square marker: tape critical current I_c as a function of the number of nodes along the tape edge. Red line with circled marker: tape gradient temperature $\Delta\theta$ as a function of the number of nodes along the tape edge at the critical state, ®2022 IEEE. Reprinted, with permission, from [2].

4.2.4 Results

The critical current value calculated with the magnetostatic model at 77 K, self-field, was $I_{c,2D} = 82.3$ A and is represented by a yellow-filled green-circled marker in Fig. 4.8a. This value is very close to the nominal $I_c = 85$ A at 0-magnetic field as the self-magnetic field generated by a single tape is in the order of mT. The I_c computed from $T-A$ model is ∼82.6 A, with a relative error of 0.36% with respect the magnetostatic model. The relative error is about 1.35% compared to the measured value of ∼83.76 A. The calibrated n-value is 22, with an error of 13% with respect to the value extrapolated from experimental data, ∼25. The $V-I$ curves are reported in Fig. 4.8a.

The temperature increases about 20 mK when the current reaches the I_c, and it can rise of about 80 mK at $1.07\,I_c$∼90 A (when the tape transits to the normal state). In Fig. 4.8b, joule losses and the cooling power required for the liquid nitrogen are reported: the trend is in a very good agreement with the $V-I$ curve.

Additionally, simulations of the I_c value with an applied external field varying form 0.5 T to 5 T were performed and reported in Table 4.5. In Fig. 4.9, we plot

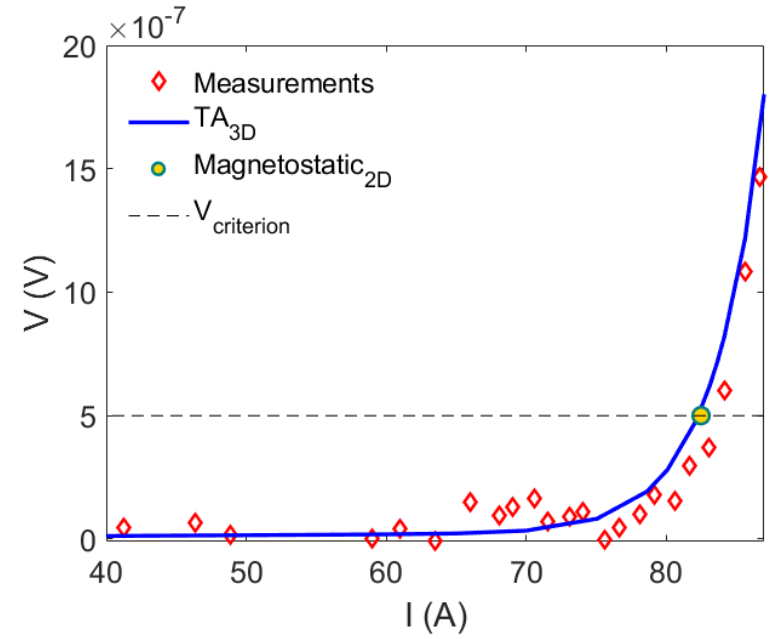

(a)

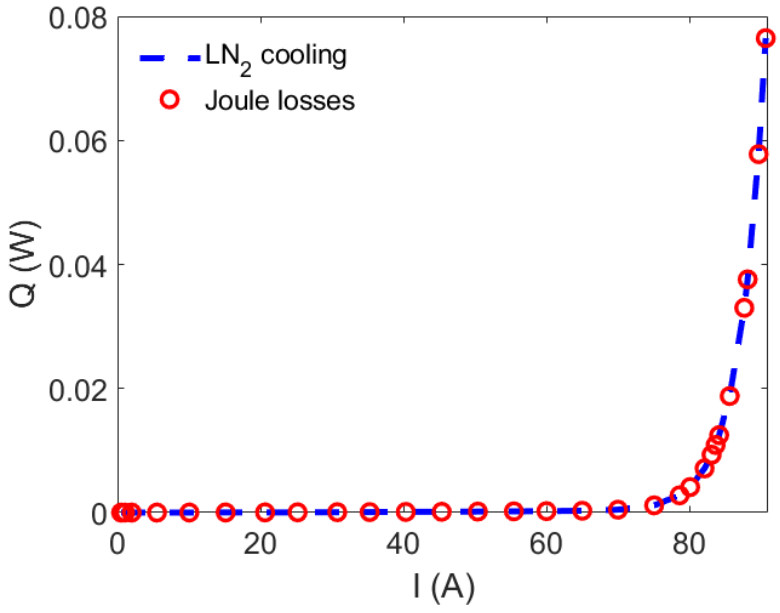

(b)

Fig. 4.8 (a) Single tape $V-I$ curve, in self field at 77 K: experimental data (red square), 3D $T-A$ simulation (blue solid line), 2D magnetostatic model (yellow circle). (b) Joule losses (red dotted line) and required cooling power (blue dashed line) vs current. ®2022 IEEE. Reprinted, with permission, from [2].

Table 4.5 I_c value as function of the external perpendicular magnetic field.

Magnetic Field B (T)	Magneto-static model I_c (A)	$T-A$ formulation I_c (A)
0.5	53.9	54.0
1	46.5	46.0
1.5	42.4	42.0
2	39.5	39.5
2.5	37.5	37.8
3	35.8	35.8
5	31.7	31.3

the prediction of $E-I$ curves ($T-A$ formulation 3D) as well as the critical current prediction (magnetostatic 2D) for different fields applied perpendicularly to the flat-wide face of the tape. Note that the $n-$value was kept at a constant value $n = 22$. The model results are in good agreement (at I_c) and, as expected, the I_c experiences a strong field dependence with an increasing amplitude of the field. At the maximum applied magnetic field (5 T, likely the maximum operating point for CCT working at 77 K with CORC®), the I_c reduces by 40%. No higher fields were explored since the irreversible field of ReBCO at 77 K is 8 T [12].

4.3 2-tapes CORC®

This section is dedicated to the demonstration that the current is able to properly redistribute among tapes, if any thermal perturbation suddenly happens. The $T-A$ formulation results are compared just with the H-formulation, since no experimental data are available. The CORC® geometry under study is constituted by 1 layer with 2 tapes, shown in Fig. 4.10a: the tape geometrical data is reported in Table 4.4. The CORC® is characterized by a core diameter of 5.2 mm and a pitch of 30 mm. In one of the tape, a heat pulse is imposed, with a consequent rise in temperature and the current flows in the other two tapes. There is no thermal contact between the two tapes.

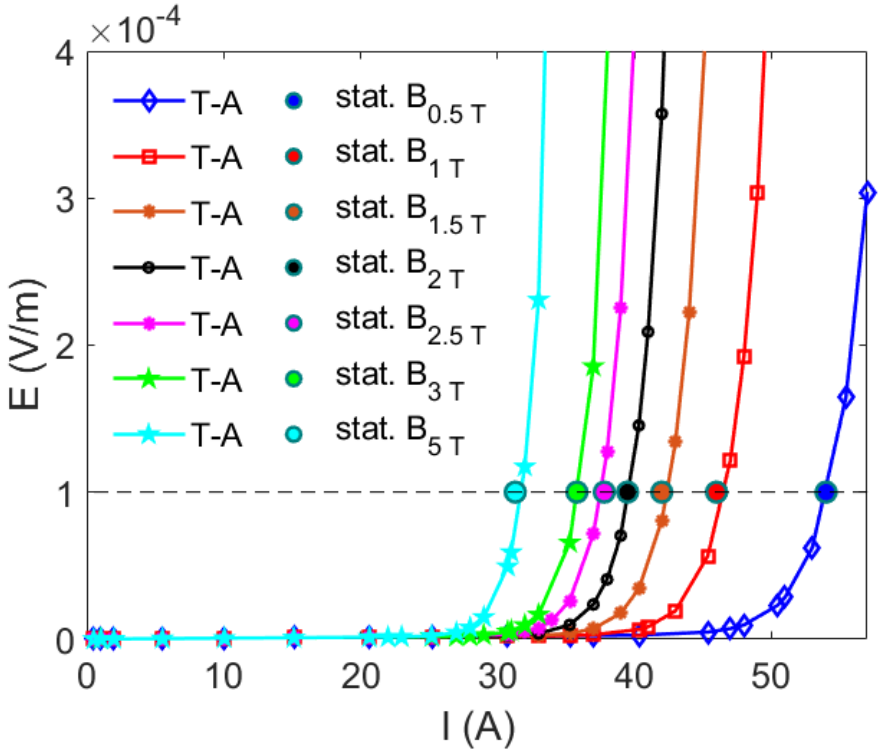

Fig. 4.9 Prediction of computed $E - I$ curves for the single tape at different transverse imposed external field, ®2022 IEEE. Reprinted, with permission, from [2].

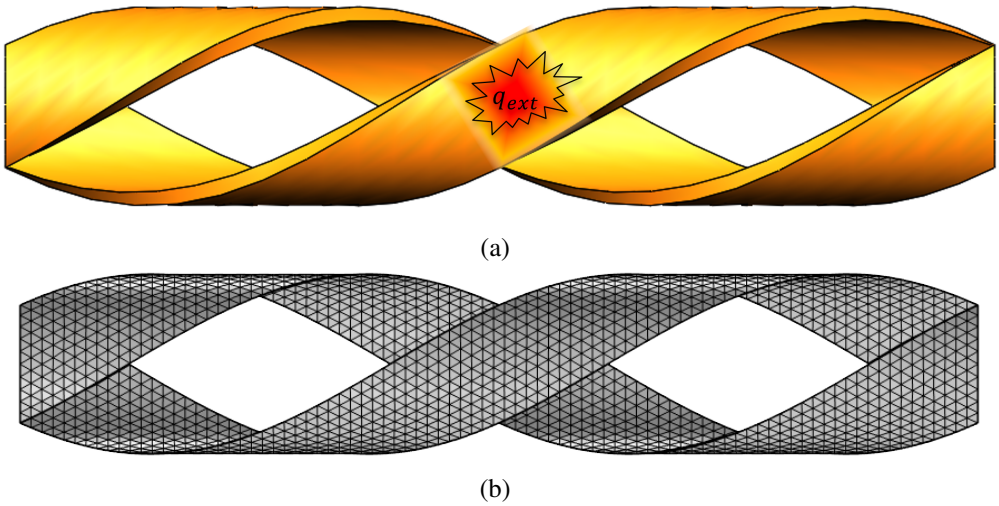

(a)

(b)

Fig. 4.10 (a) Sketch of CORC® cable geometry used for case study 2. (b) Mesh used for the current case, ®2022 IEEE. Reprinted, with permission, from [2].

4.3.1 Simulation set-up

The current ramps-up in 0.1 s reaching a flat top of $I_{ext} = 85$ A (each tape experiences $0.5I_{c0}$). Heat is deposited at the center of one of the tapes via a gaussian pulse starting at 0.12 s and placed at the center of the tape over a length of 2 mm, see Fig. 4.10a. The volumetric heat source q_{ext} has been computed to increase the temperature of about 10 K. The heat releases a thermal energy of $E_{ext} = 45$ mJ, without taking into account of joule losses.

4.3.2 Meshes

In the $T-A$ model, the 3D air domain has been discretized with an unstructured tetrahedral mesh (about 53000 tetrahedral) and the 2D CORC® tape surfaces with unstructured triangular mesh (about 3800 triangles), see Fig. 4.10b. In the H model, the mesh counts for a total number of elements of 66000: tapes have been meshed with a tetrahedral structured mesh counting for 3 element along the thickness and 60 element along the length. The air has been discretized with an unstructured tetrahedral mesh. The simulation ends at 1 s with a timestep $dt = 0.1$ ms, that it is refined during the heating time.

4.3.3 Results

The current is ramped up on the 2-tape CORC® , and it is equally split among the two tapes, see Fig. 4.11. At 0.12 s, the external heat source is switched on, and the tape starts to rise in temperature, with a consequent resistivity increase, so that the current flows in the other tape. At 0.17 s, the peak temperature of $\sim$86.5 K, see Fig. 4.12b, so that the current is increasing in the second tape. In Fig. 4.13, current and temperature maps are reported at different time to show how the current redistributes.
In Fig. 4.11, transport currents flowing in the two tape computed from $T-A$ model are reported and compared with a H-formulation. When the heating is starting, the $T-A$ is in good agreement with the H-formulation, and the current in the second tape is rising with the same rate. At the peak, and the recovery is faster in the $T-A$ formulation than in the H-formulation, with a maximum error of 8%. In Fig. 4.12a the external power and the cooling are compared: they are in perfect agreement.

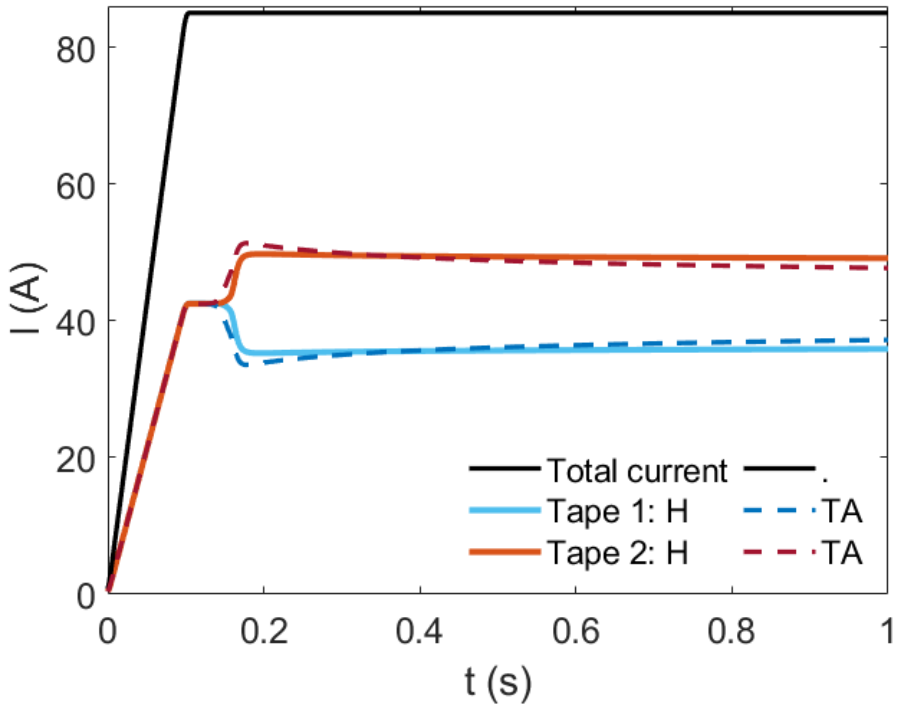

Fig. 4.11 2-tape CORC® current evolution: solid lines correspond to H-formulation results, dashed lines correspond to $T-A$ formulation results. ®2022 IEEE. Reprinted, with permission, from [2].

From Fig. 4.12b, the maximum temperature reached of the heated tape is reported for both the volume and thin shell module: the maximum error between them is $< 0.1\%$.

The $T-A$ counts for about 346000 degrees of freedom (DoFs), while the H-formulation for about 193000 DoFs: the former has a total computational time of about 1 h and 45 min, the latter for of about 2 h and 30 min, showing an advantage in saving time.

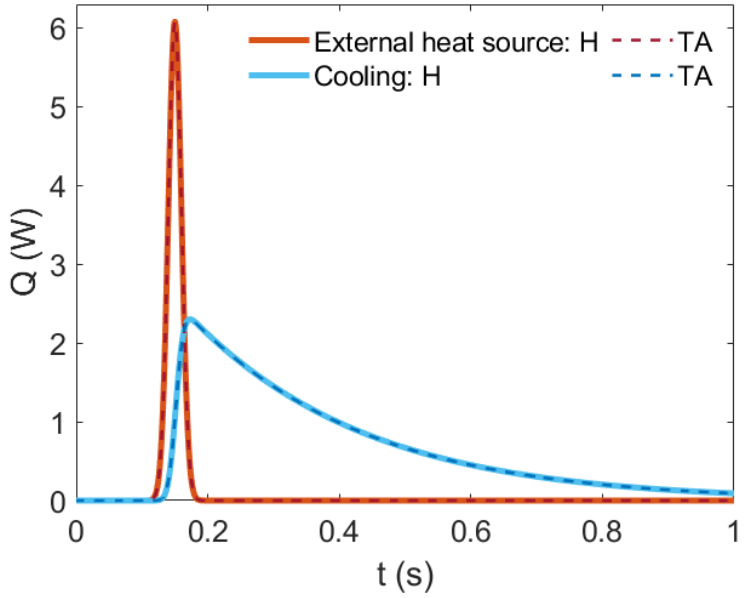

(a)

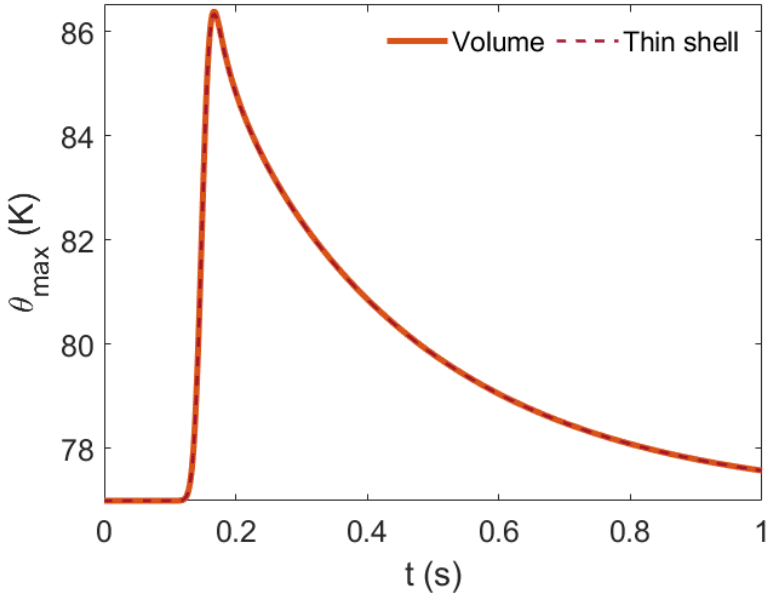

(b)

Fig. 4.12 (a) External heat source in red, and computed cooling power in blue. Solid lines correspond to 3D model coupled with H-formulation, dashed lines correspond to thin shell model coupled with $T-A$ formulation results. (b) Total Joule losses in 2-tapes CORC® : solid line is the volume model, the dashed line is the thin shell. ®2022 IEEE. Reprinted, with permission, from [2].

Fig. 4.13 Temperature, critical current density and current density norm maps at different timesteps in the 2-tapes CORC® computed in $T-A$ model. ®2022 IEEE. Reprinted, with permission, from [2].

Table 4.6 6-tape CORC® geometry parameters.

Parameters	Value	Units
YBCO thickness	1.6	μm
Silver thickness	1.6	μm
Copper thickness	5	μm
Hastelloy thickness	20	μm
Tape thickness	45.2	μm
Core diameter	2.76	mm
Cable pitch	5.7	mm
CORC® diameter within the termination	4.7	mm

4.4 6-tapes CORC®

The $T-A$ model has been validated with more complex geometry constituted by a 6-tape CORC® cable, operating at 77 K, test at the LBNL. The CORC® cable under study is composed of 3 layers with 2 tapes per layer, as shown in Fig. 3.5b, having a length of 0.5 m. Table 4.6 summarizes the main geometrical parameters of the CORC® under study.

4.4.1 Experimental set-up

The experimental setup is the same utilized for the CORC® cable manufactured for testing the Vacuum Pressure Impregnation (VPI) process [202]. From the cable manufacturer, the expected nominal critical current for a straight non-twisted cable and without taking into account of the self-field effects, is $I_c = 378$ A [42]. From experience, however, it was observed that the nominal of $I_c = 378$ A normally is reduced by $20-30\%$ due to the self-field effects generated by the twisting of the CORC® and to the presence of the terminations, leading to an expected I_c value that lies withing the range of $260-300$ A. The measured I_c for the straight CORC® is indeed 262.5 A, evaluated at the average electric field of 100 μV/m. The termination is 63.5 mm long and the voltage taps is set at 75 mm from the termination, see Fig. 4.14a. Further reduction of I_c occurs in the terminations, since the tapes are spreading out and the inner radius is larger (see Fig. 4.14b). At the terminations,

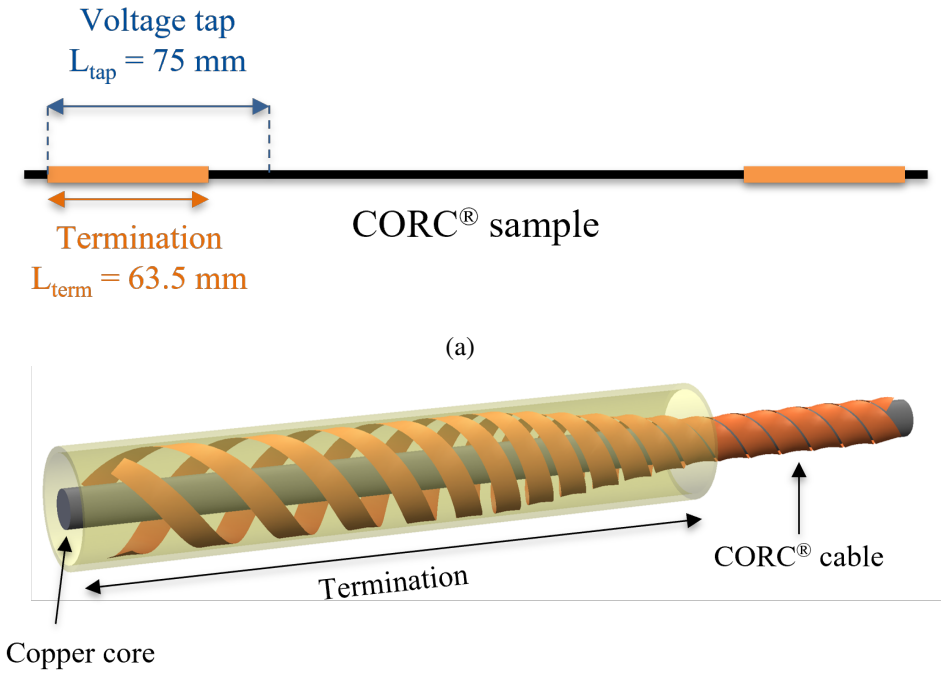

Fig. 4.14 (a) Experimental set up. (b) Detail of CORC® cable within the termination. ®2022 IEEE. Reprinted, with permission, from [2].

self-field effects is more pronounced with respect to the center of the CORC® wire with the nominal radius and resistive effects may occur.

4.4.2 Simulation set-up

The simulations aim at reproducing the $V-I$ curve experiments carried out in a bath of liquid nitrogen at 77 K in straight conditions. The current is ramped up and then wait for the stationary conditions. The tape critical current will decrease due to winding process. The degradation of 25% ($\psi = 0.75$) has been evaluated from Fig. 3.8 and the maximum strain $\approx -0.7\%$ from Eq. (3.40) (in good agreement with what has been computed and measured in [165]), so that the I_{c0} for each tape wounded on the CORC® is 63.75 A. Three sets of simulation have been carried out: first, a pitch of the main CORC® wire with the nominal winding radius at 77 K; then, a pitch of CORC® wire within the termination at 77 K, to account for the tapes spreading out and, finally, the last geometry at 80 K to consider a possible Joule effect in the termination.

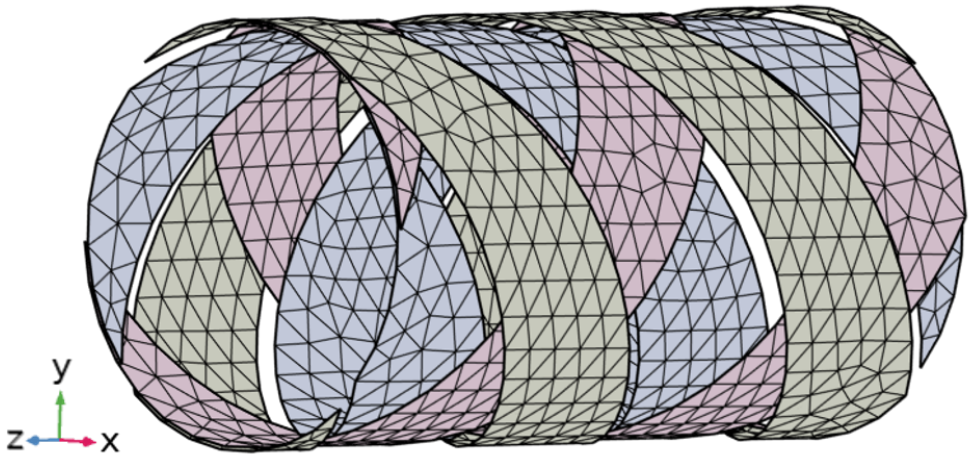

Fig. 4.15 Illustration of the 3D meshed CORC® cable with larger inner diameter used for the solution in COMSOL. ®2022 IEEE. Reprinted, with permission, from [2].

4.4.3 Mesh

The 3D air domain has been discretized with an unstructured tetrahedral mesh (about 25′000 tetrahedra) and the 2D CORC® tape surfaces with unstructured triangular mesh (about 38′00 triangles), see Fig. 4.15.

4.4.4 Results

In Fig. 4.16a, the norm of the current density distribution J_{abs} over the critical current density J_c in self-field is shown. The input current is 200 A (each tape experiences $\approx 0.5 I_{c0}$), so we are fully in the superconductive state. Even though the temperature is uniform at 77 K, it is possible to notice that the current distribution is not uniform: this is due to the non-uniform self-induced magnetic field by the cable in different tapes. This result is demonstrating that the model is able to properly calculate the current redistribution among tapes, not just for a thermal perturbation, but even for a magnetic disturbance. The magnetic field, of the order of few mT, is higher in the outermost layer and lower in the innermost layer since the former is subject to the magnetic field induced by the internal layer. Moreover, the magnetic field is stronger where tapes overlap. This reduces locally the critical current and thus increases the resistivity, with a consequent current redistribution and non-uniformity. That is guaranteed by the novel boundary condition adopted in

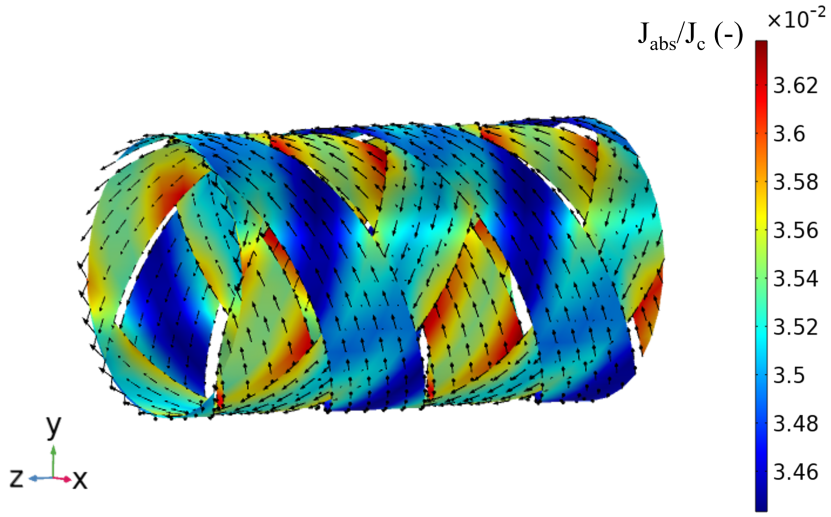

(a)

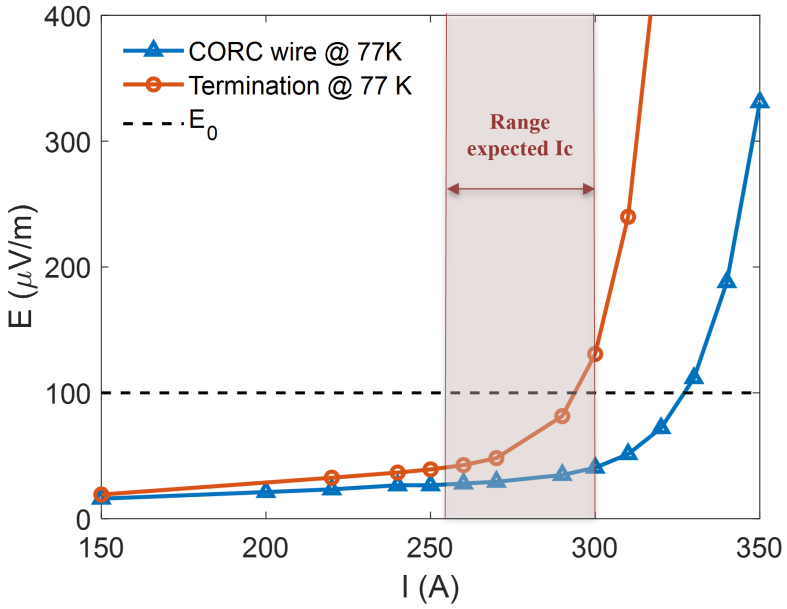

(b)

Fig. 4.16 6-tape CORC® cable in self field: (a) Magnitude of the current density norm J_{abs} over critical current density J_c when steady-state is reached: non-homogeneous current distribution among tapes; (b) Computed $E-I$ curves comparison: blue CORC® wire and red termination both at 77 K. ®2022 IEEE. Reprinted, with permission, from [2].

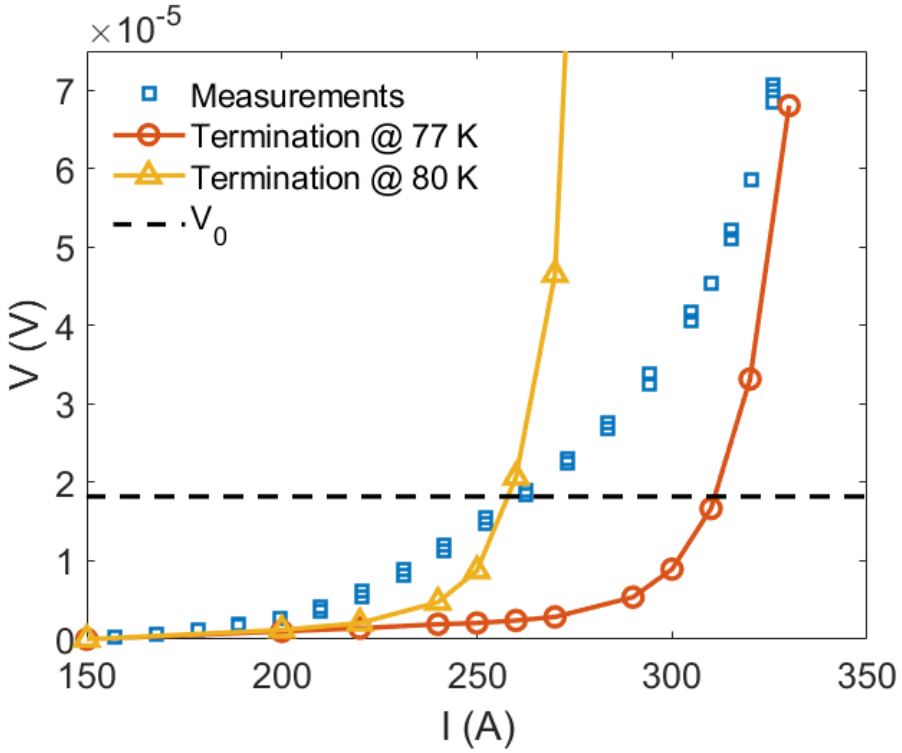

Fig. 4.17 $V-I$ curves comparison: measurements (blue square), computations within the termination at 77 K (red solid line), and computations within the termination at 80 K (yellow solid line). V_0 is the voltage criterion. ®2022 IEEE. Reprinted, with permission, from [2].

this study. In Fig. 4.16b the electric field E versus the current I curves of the main CORC® wire is compared with the $E-I$ curve of CORC® within the termination (wire with the larger winding radius) at 77 K. The I_c computed for the termination is well in line with the expectations from the manufacturers (292 A). While the $E-I$ curve, computed for the CORC® with its original radius, gave back a much higher critical current than expected (327 A). The critical current in the termination further reduces if a local heating is considered due to Joule effect in the termination – here the effect has been reproduced in a simplified way assuming a temperature of 80 K as boundary condition for the simulation. The value of the experimental voltage is reported in Fig. 4.17 as a function of the current, and compared with the value computed from the simulations. The computed voltage $V_{computed}$ is given by the sum of an average voltage drops in the termination and in the main cable as follows:

$$V_{computed} = \int_{L_{tap}} \mathbf{E}_{main} \cdot \mathrm{d}\mathbf{l} + \int_{L_{term}} \mathbf{E}_{term} \cdot \mathrm{d}\mathbf{l} \tag{4.2}$$

Table 4.7 12-tape CORC® geometry parameters, from [169].

Parameters	Value	Units
YBCO thickness	1.6	μm
Copper thickness	5	μm
Hastelloy thickness	30	μm
Tape thickness	42	μm
Tape width	2	mm
Core diameter	2.54	mm
Average cable pitch	5.54	mm

where $\mathbf{E}_{main}$ is the electric field computed for a pitch of CORC® wounded according to the nominal former diameter, L_{tap} corresponds to the length at which the tap is located (75 mm), $\mathbf{E}_{term}$ is the electric field computed for CORC® within the termination and L_{term} is the termination length (63.5 mm), see Fig. 4.14a. The experimental critical current in Fig. 4.17 (262.5 A) is in the expected range, but lower than the one computed with the termination at 77 K. When the termination is assumed at 80 K, which seems compatible with the temperature increase at the termination, the computed I_c is closer to the experimental value (258 A). Moreover, the discrepancy may be not only due to a higher temperature within the termination, but also a possible variation of the conductor properties: it might be possible that some tapes could be affected by defects reflecting in a smaller critical current also in the CORC® wire.

4.5 12-tapes CORC®

To further validate the stability and reliability of model, a geometry of 6-layers and 12-tapes CORC® straight cable (see Fig. 4.18a). The cable is operating at 76 K, and the results are compared with data available in literature from [39, 169]. The cable is composed of 2 mm wide tapes and 2.54 mm core inner diameter. Geometrical parameters are reported in Table 4.7.

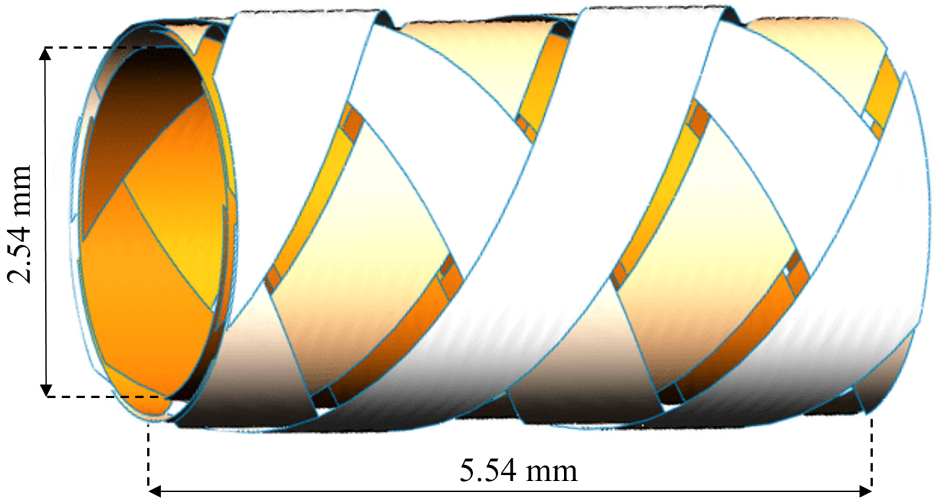

(a)

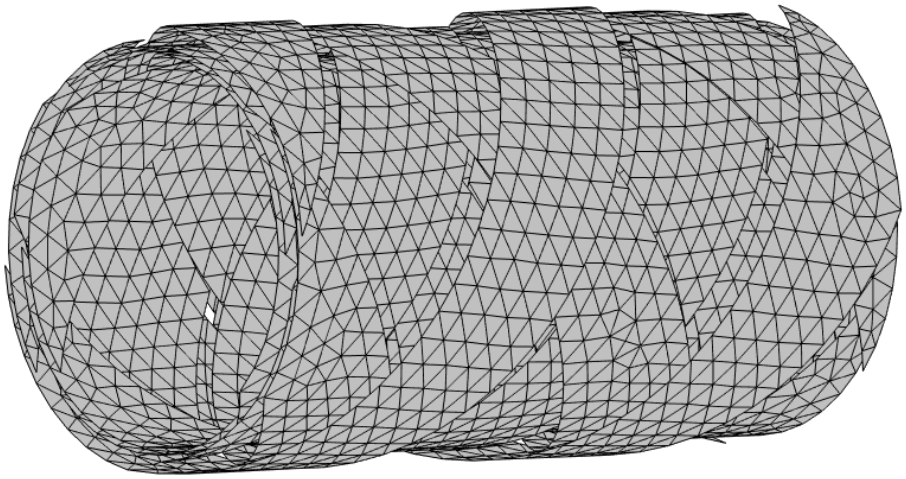

(b)

Fig. 4.18 (a) Sketch of the 3D studied geometry of the 12-tapes CORC® cable. and (b) Solved mesh for this case study.

4.5.1 Experimental set-up

The studied geometry is referred to wire W1 in [39], where experimental setup is also described. The YBCO tapes are from SuperPowewr Inc. characterized by 1.6 μm thickness of the superconducting layer and an average tape nominal critical current at 76 K is 60.2 A,without self-field correction. The nominal critical current from the wire is 722 A. Critical current measurements were performed ramping the current in small steps and settled on each plateau for 3 s to recorder the voltage. The terminations (average length 15 cm) give a resistive contribution of approximately 145 nΩ, subtracted to the measurements. The termination are 15 cm long and the cable between them is 49 cm. The measured I_c is $\approx$ 72% of the nominal value ($\approx$ 526 A), mostly due to the self-field and termination effect, and the measured n-value is 7.8 for the straight before bending.

4.5.2 Simulation set-up

In order to reproduce the experiments, also here the current is ramped up and then wait for the stationary conditions to compute the voltage drop. Due to the lack of information, the critical current parameters are assumed the same as in Table 3.2. The compressive strain ε_{w0} along the width is computed in [169], see Fig. 4.19 and used in this study. To take into account that the innermost layers have a smaller winding diameters, thus they are more compressed, the compressive strain ε_w has been increased according the layer inner diameter d:

$$\varepsilon_{wi} = \varepsilon_{w0} \cdot \frac{d_6}{d_i} \tag{4.3}$$

where the subscript i indicates the $i-$th layers and ε_{w0} is related to the sixth layer.

4.5.3 Mesh

The 3D air domain has been discretized with an unstructured tetrahedral mesh (about 70′000 tetrahedra) and the 2D CORC® tape surfaces with unstructured triangular mesh (about 11′000 triangles), see Fig. 4.18b. The total number of Dofs is $\approx$ 400′000. The simulation run in $\approx$ 1 h each ramp of current.

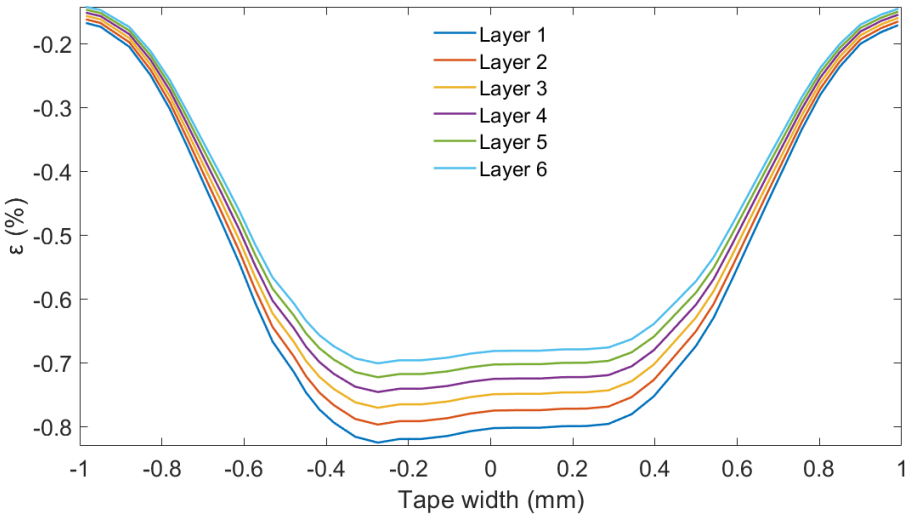

Fig. 4.19 Strain distribution along the tape width for the 6-layers CORC® from [169].

4.5.4 V-I results

In Fig. 4.20, the maps of the norm self-field are reported considered a transport current of 450 A. It is possible to notice, that the outermost layers are subject to the strongest magnetic field, which will reduce towards the center of the cable, see Fig. 4.20a. The outermost tapes, in fact, are shielding and protecting the innermost ones: this is one of the peculiarity of the CORC® cable, thanks to its round shape. Moreover, the magnetic field is stronger where tapes overlap. This non-homogeneity will reflect on the critical current density, thus on the current density distribution, which will reduce locally, with a consequent increase of resistivity. The map of the non-uniform current density in self-field at 450 A is reported in Fig. 4.21a. The cable is still in superconductive state. The temperature is not playing a significant role at this moment, it is almost uniform at 76 K. Nonetheless, the critical current density varies according to the magnetic field distribution among tapes, further demonstrating the capability of the model to redistribute the current in accordance to the operating conditions. The current density is denser in the innermost layer, since the critical current density will be higher. Fig. 4.21b, instead,shows the heat generated by possible joule losses and by conduction on overlapping tapes. The power, express in W/m^3, is negligible, since the cable is still superconductive. Nevertheless, some non-uniformity is visible: the inner tapes are subject to a slightly higher power, since their are carrying most of the current and because of the conduction from the

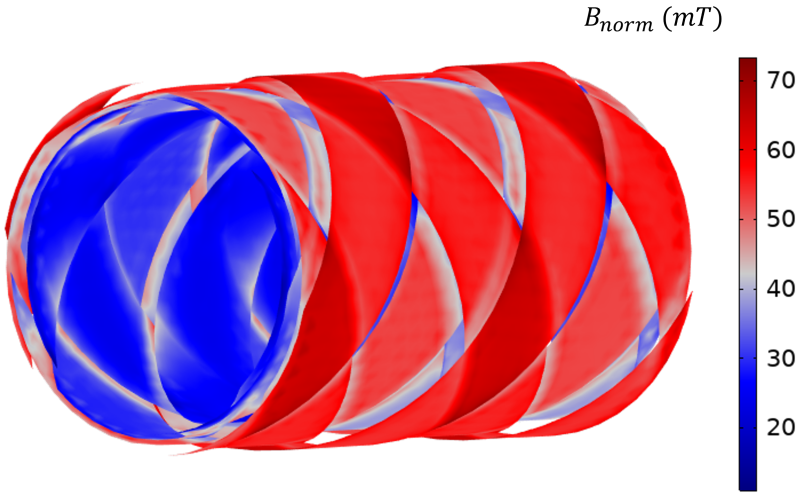

(a)

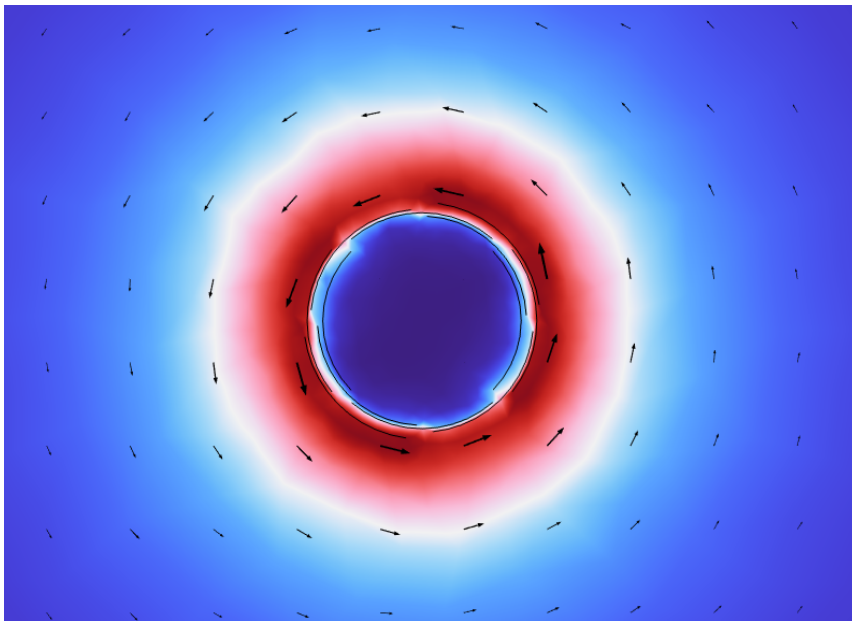

(b)

Fig. 4.20 Magnetic field norm in the 12-tapes layout in self field at transport current of 450 A: (a) zoom of the CORC® surface: the outermost layers are shielding and protecting the innermost ones; (b) front view of the cable.

other layers. Finally, in Fig. 4.22, the computed $E-I$ curve is compared to the measurements data. First, the voltage drop is computed as the surface integral of the electric field E on the entire tape surface divided the tape width w:

$$V = \frac{1}{w}\iint E \mathrm{d}S \tag{4.4}$$

Then, the total average electric field is computed as:

$$E = V/L_{tape} \tag{4.5}$$

where $L_{tape} \approx 9.83mm$ is the length of the tape edge. The critical current prediction is in perfect agreement with reference: the computed I_c is ≈ 527 A (0.2% of relative error). Nonetheless, the n-value is strongly overestimated: the computed n-value is 20. The model is providing feasible and stable results, in accordance with the physics of the problem. This discrepancy on the $E-I$ curve may be due the strong assumption of using the same parameter of the previous cases. The tapes are from the same manufacturer, nonetheless they are characterized by a lower critical current. Thus, the n-value or the other power law parameters might be different from Table 3.2, meaning that the scaling might not be generalized. Another explanation might be that there are some aspects of the physics of the problem that are unclear, and not considered in the model.

4.6 6-tapes bended CORC®

Finally, the bended cable 6-tapes CORC® cable has been simulated and the results of the proposed model have been compared to the experimental results, measured at the Lawrence Berkeley National Laboratory (LBNL). The $V-I$ curve is measured in a LN_2 bath at 77 K and in self-field conditions.

4.6.1 Experimental set-up

The sketch of the experimental setup is reported in Fig. 4.23a. Details can be found in [202]. Different bending radii and vacuum pressure impregnation procedures were performed to quantify the degradation of cable performances. In this study, the Sample 2b of [202] is considered. The wire was bended in an aluminum fixture in

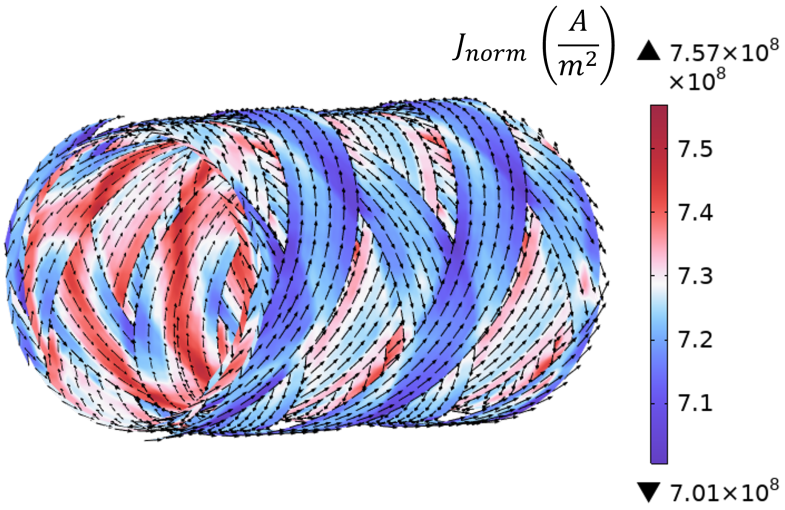

(a)

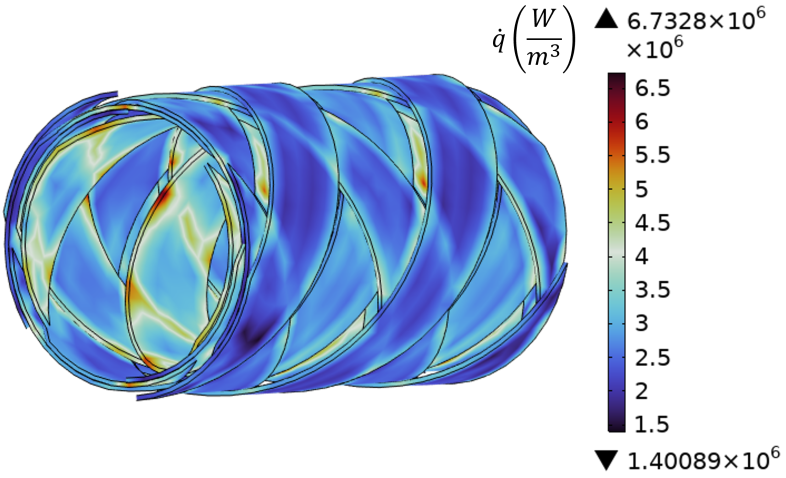

(b)

Fig. 4.21 12-tape CORC® cable in self field at transport current of 450 A: (a) Magnitude of the current density norm J_{norm}: non-homogeneous current distribution among tapes; (b) Dissipated heat due to joule losses and conduction among tapes.

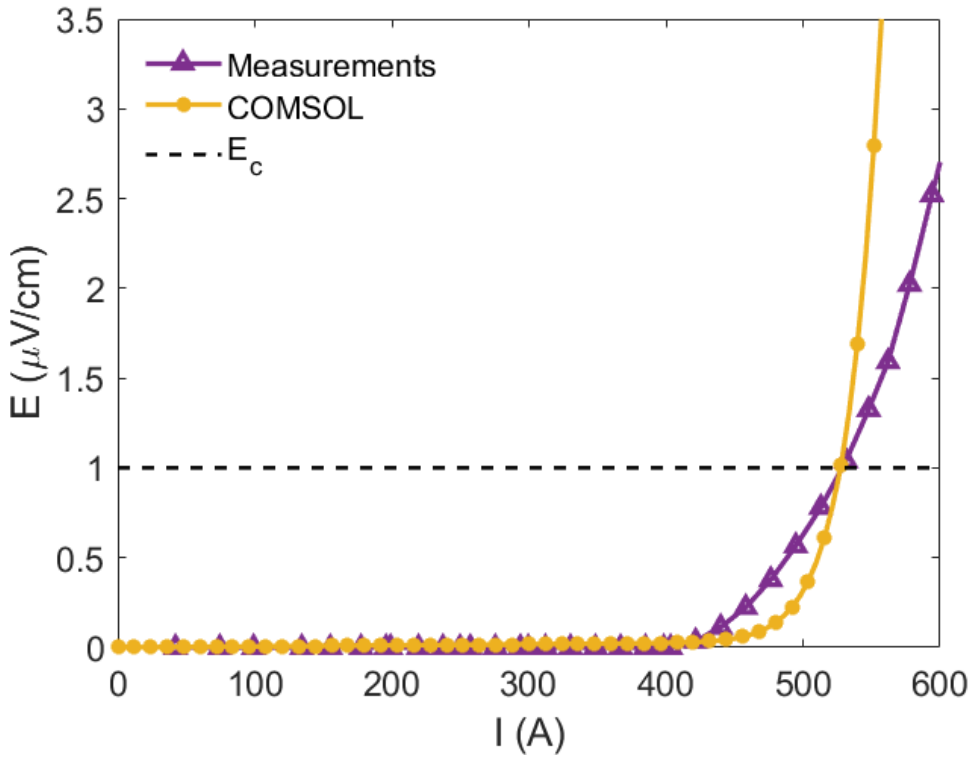

Fig. 4.22 12-tapes CORC® cables $E-I$ curves comparison: measurements (violet triangles) and COMSOL results (yellow line). E_c is the electric field criterion.

grooves of 4.5 mm diameter. Voltage taps were soldered to the wires at distances 5, 40 and 75 mm up from the bottom of the copper terminations. Tapered tapes in the terminations had been soldered to the copper tube to guarantee a proper current injection.

4.6.2 Simulation set-up

In the cable model, an environment temperature of 77 K is considered, the current is ramped up, and the voltage drop is computed once the steady-state condition is reached. The domain and the boundary conditions are sketched in Fig. 4.23b. The straight part as been simulated separately: leveraging on the periodicity of the geometry, just a pitch has been considered. The curved part has been simulated considering a pitch to avoid edge effects. The voltage drop V_{tot} has computed by the sum of voltages drop on the two domains:

$$V_{tot} = \int_{L_{str}} \mathbf{E}_{str} \cdot \mathrm{d}\mathbf{l} + \int_{L_{curve}} \mathbf{E}_{curve} \cdot \mathrm{d}\mathbf{l} \tag{4.6}$$

Where L is the cable length, E is the electric field, subscripts str and $curve$ are referred to the straight and the curve part, respectively. The mesh counts about 640k elements with an average quality of 0.6. The simulation of a single value of current might run for $\sim$1 h, when the current density is far from the critical condition. In the latter case, it requires $\sim$6.5 h.

4.6.3 V-I results

Fig. 4.24a reports the comparison between the measurements and the numerical model of the $V-I$ curve, as well as the critical current. The critical current value is well-captured from the model: the measured I_c is $\sim$218 A, while the computed is $\sim$217 A. Nonetheless, the total performance of the cable, specifically the n-value is largely overestimated in COMSOL. The measured n-value is $\sim$6.5, while the computed is $\sim$15. The main possible reason for this behavior is that since the cable is short, the termination may still play a significant role in the voltage drop. Moreover, a better strain evaluation through a proper mechanical model, which considers buckling of tapes, might explain this discrepancy. In Fig. 4.24b, the average electric field of the bended part E_{bended} and of a straight pitch $E_{straight}$ are compared: as expected, the

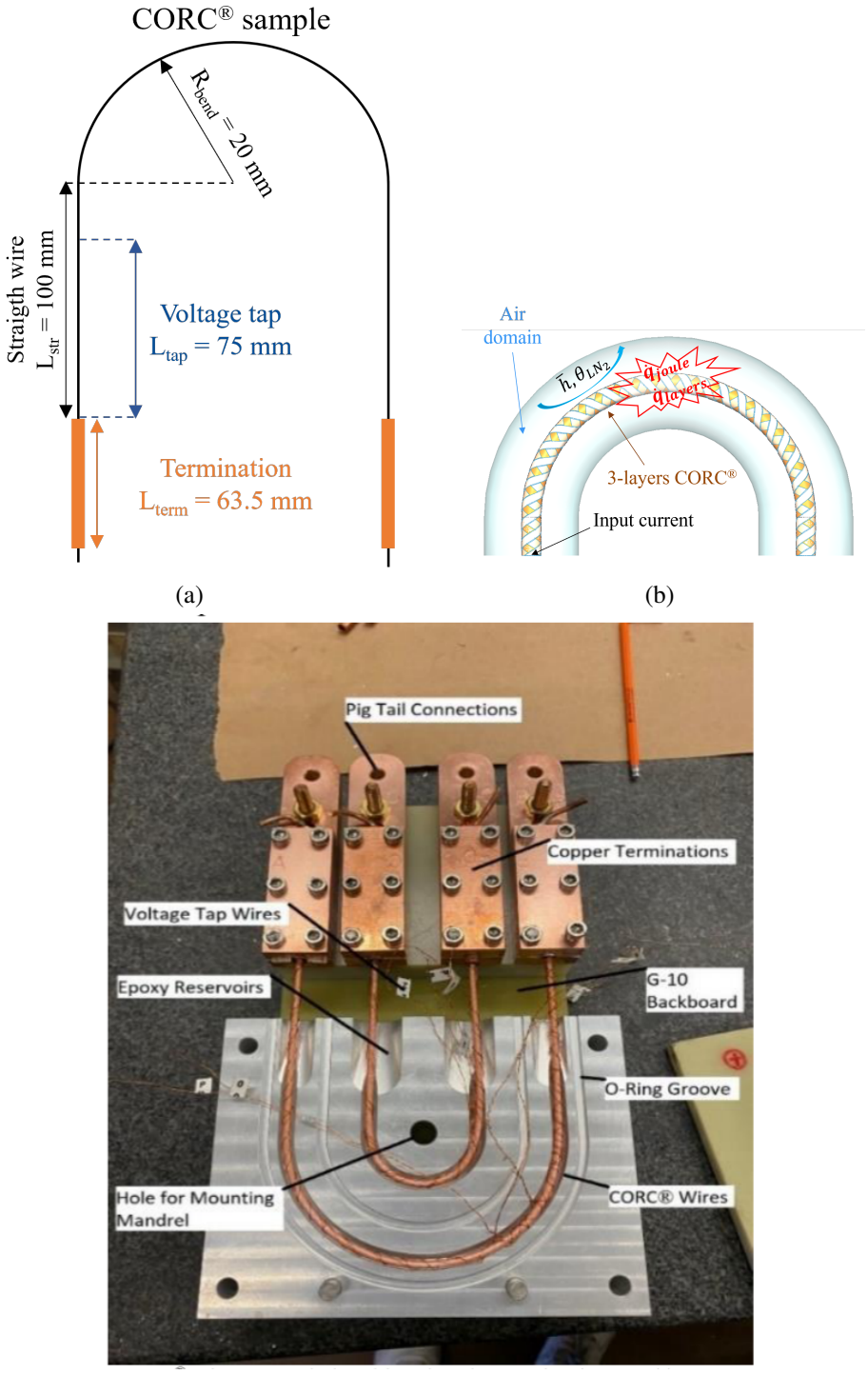

Fig. 4.23 Sketch of a) the experimental setup and b) the simulated domain and boundary conditions, ®2022 IEEE. Reprinted, with permission, from [142]. c) Picture of the experimental set-up carried out at the LBNL. ®2022 IEEE. Reprinted, with permission, from [202].

E_{bended} is higher due to the stronger deformation. The temperature increases about $\sim$10 mK when the current reaches the I_c, and it can rise of about 30 mK at 230 A (when the tape transits to the normal state). In Fig. 4.24c, the norm of the current density distribution J_{norm} in self-field is shown. The total input current is 150 A (each tape experiences $\sim 0.5 I_c$), so the tapes are fully in the superconductive state. The non-homogenous distribution of the current density is due to the self-induced magnetic field among different tapes. The magnetic field is stronger on the outermost layer and where tapes overlap, with a consequent reduction of the critical current density, increase of the resistivity, and therefore the redistribution of the current.

4.7 Drawbacks

For the first time, a multiphysics model can accurately simulate the thermal, electric and magnetic behaviors of CORC® cables and wires, including the current sharing among tapes by using a set of self-consistent boundary conditions adopted in strong form. The model is stable, and it is able to simulate different layouts and conditions, consistenly with the physics of the problem. Nonetheless, there some drawbacks to be considered:

- Computational cost: the number of Dofs significantly increases respect to the traditional $T-A$ formulation. The current sharing condition increase the number of unknown, since the current vector potential T along the edge is not explicit (usually imposed through a Dirichlet boundary condition), but the code need to compute it;
- Instability and convergence: complex geometry slows the convergence of the simulations, mainly due to the strong non-linearity, the periodic boundary conditions and the current sharing condition. To solve this problem, slow ramp of current and small time step are preferable, to avoid too large variation between to subsequent time instant. The initial step is the most complex one, therefore a very small initial time step helps the convergence. Moreover, since at the beginning some parameters are equal to zero, causing some numerical error, adding the machine precision value in those parameters helps to stabilize the simulation;

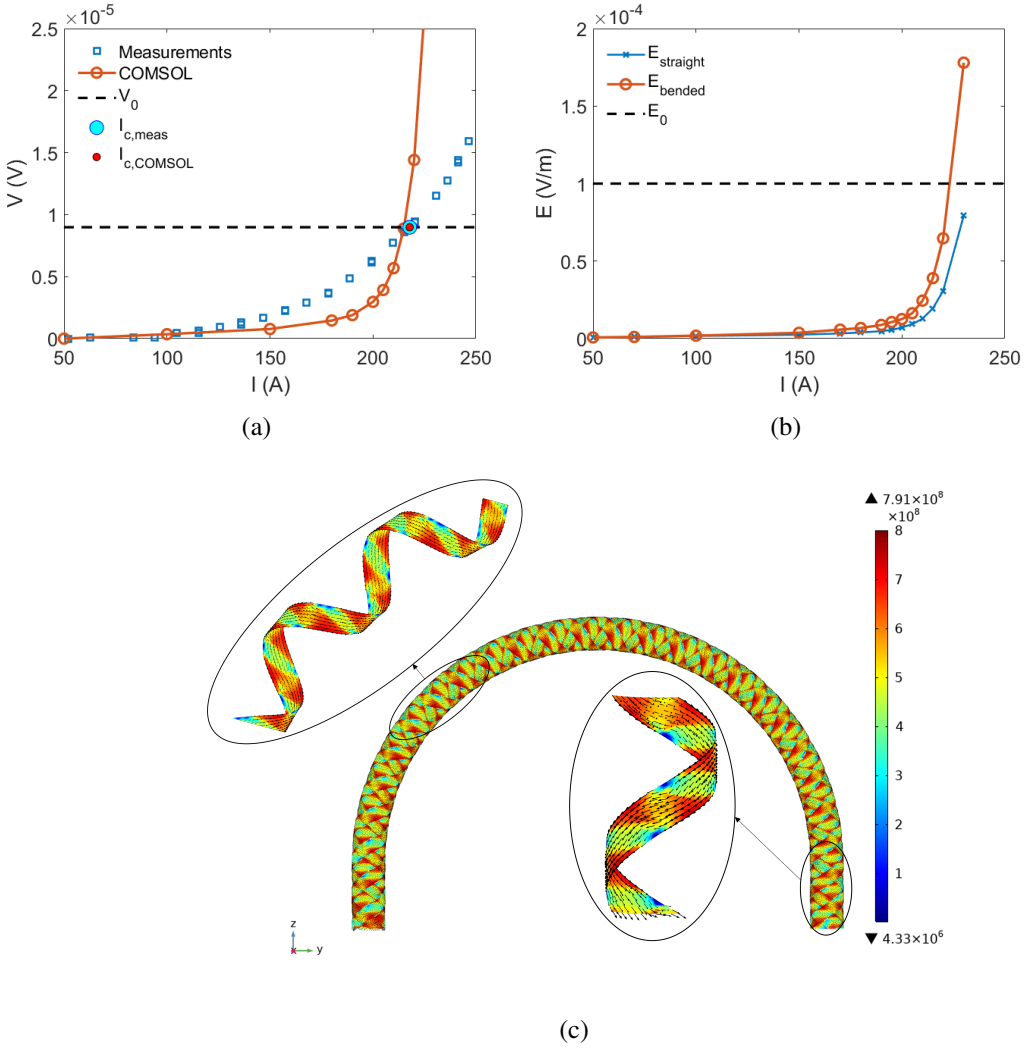

Fig. 4.24 a) Comparison between measured and numerically computed $V-I$ curves. Square dots referred to the experimental data, red solid line to the COMSOL simulation, the light blue circle is the measured I_c, and finally the red dot is the COMSOL I_c. b) Comparison between the average electric field of the bended part, red line, and of a straight pitch, blue line. c) Current density map at 150 A of total input current, ®2022 IEEE. Reprinted, with permission, from [142].

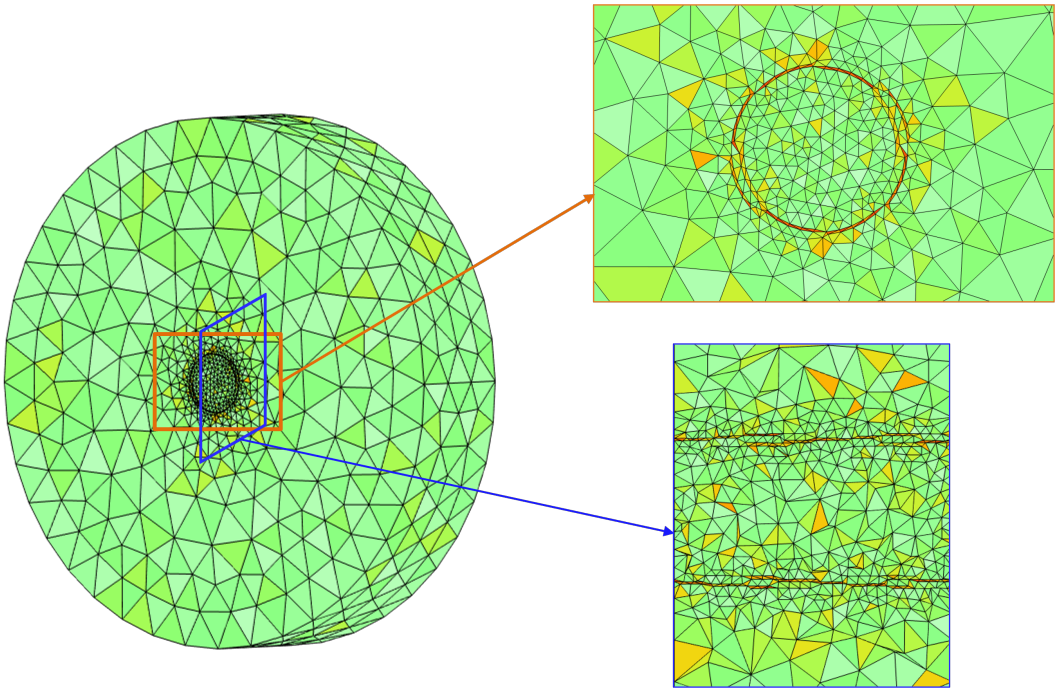

Fig. 4.25 Mesh skewness in a 12-tapes mesh: zoom in on the overlapping tape zone.

- Complexity of the implementation: the mapping of the T and the other variables, both for PBC and current sharing condition, makes the model set-up non trivial;
- Mesh creation: when the CORC® twist pitch is too small, any swept mesh can be built. Unstructured triangular mesh works well, but there is less control on air domain elements between overlapping layers. The smaller distance among them creates a tetrahedral elements on air domain with a very high aspect ratio, thus bad quality. Finer mesh is helpful, but with a consequent increase of computational time. A good quality mesher software might help the mesh creation. There are not specific requirements, but avoinding low quality tetrahedra elements in the air domain, see Fig. 4.25.

The general behaviour of the CORC® is well captured, especially the current sharing problem has been tackled. This list of drawbacks is the starting point for further improvements and possible directions to investigate as follow-up of this work.

Chapter 5

Discussion and perspectives

This last chapter is devoted to conclusions, including a summary of highlights and the main achievements of this Ph.D. activity, and eventual outlook of the presented work. The main focus is the development of a multiphysics numerical finite element model for the characterization of the critical current of Conductor-on-Round-Core cables.

This thesis considers the application of High Temperature Superconductors (HTS) materials for high-field magnet systems, e.g. particle accelerators and fusion magnets. They constitute the most viable option towards the development of high field magnets satisfying the requirements of high operating currents, high current densities, and compact coil layouts. Among HTS materials, Rare-Earth Barium Copper Oxide (ReBCO) are the most promising alternative for the high critical current density and high critical temperature. The capability of carrying much higher electrical current with respect to the LTS, guaranteeing at the same time a higher thermal stability, since the large temperature margin, results convenient for high deposition and fast-ramping applications. They have the possibility of operating at very high temperatures (up to 77 K) and they have excellent performances at low temperature, from 4.2 K to 20 K, able to generate magnets up to 20 T and above. ReBCO compounds are a family of ceramic multilayers materials commercially available as flat tapes of $4-12$ mm wide and $\approx 40-100$ μm thick. The superconductor layer of $1-2$ μm thickness is coated by a copper stabilizer and silver, and it is separated from the metal substrate with a buffer. The substrate improves the mechanical stability and properties of the tape. Beyond the very good characteristic of ReBCO coated conductors, cables and magnets needs to deal with the flat shape, the low thermal properties and the strong

anisotropy of the magnetic field orientation on the critical current. The strength of the Hastelloy layer, one of the most common used substrate, led toward the development of the Conductor-on-Round-Core (CORC®) design. This is the only round cable made of ReBCO coated conductor flat tapes wounded inwards onto small formers in multiple layers, alternatively clockwise and counter-clockwise, allowing mechanical and electromagnetic isotropy and reduction of AC losses. One of the key parameter to quantify the performance of a superconducting cables is the critical current I_c, the maximum current which can be transport without transitioning to the normal state. The I_c can degrade during production process and is strongly related to operation conditions. Dedicated experiments for the I_c characterization to quantify the degradation due to the winding process and operating conditions needs to proceed in parallel to the development of numerical models capable to reproduce and, in perspective, predict the cable performance. The complex geometry and shape of CORC® are tricky to reproduced correctly and study with numerical tools.
This work present a new full 3D multi-physics numerical model for the characterization of the critical current of HTS tapes, based on the hybrid $T-A$ formulation coupled with the heat equation, has been proposed here capable to reproduce the $V-I$ curve and I_c of CORC® , together with its validation. The model is implemented in COMSOL Multiphysics®. Due to the strain sensitivity of ReBCO tapes, the mechanical strain degrades the cable: a simplified evaluation of the strain map, based on pure geometrical assumptions, allow the quantification of I_c degradation, from data available in literature, due to the deformation in each element of the computational domain. Based on the definition of strain (the ratio among the elongation ΔL and the initial length L_0), three strain contributions have been considered: intrinsic strain, due to the winding of the tape on the copper core (available from literature); strain due to the bending, computed as the ratio of the displayed radius from the neutral radius; and, finally, shrinkage of the tape due to the bending, staring from volume conservation and the difference between the initial and the final thickness (before and after bending, respectively). In each element domain the total strain is obtained from superposition principle. The percentage of degradation of the tape critical current density due to the strain state has been extrapolated from literature. In addition, thermal effects are strong drivers of the behavior of HTS cables, multiphysics models combining the $T-A$ formulation to a thermal model in thin shells are already available in literature, mostly aimed to simulate quench behavior. Most of the time, no other heat sink takes into account the refrigeration

with the coolant, with a possible underestimation of cable performances. In this work, a thermal model takes into account the Joule losses (if any), the possible conduction among overlapping tapes and an active convective cooling of the cryogen is accounted for,and it is coupled to the electromagnetic module. Moreover, one of the main issues to tackle was the current distribution or re-distribution among multiple tape and layers in CORC® . The main novelty with respect to previous works is the model capability to compute and redistribute the current without any external circuital network, according to possible disturbance or defect on each tape (i.e., hot spot temperature or electromagnetic difference).The model relies on a multiscale approach starting from the homogenization of the tape properties that are then applied to the CORC® wires. The model has been verified and benchmarked against other established magnetic formulations, and it has been able to reproduce the $V-I$ characteristic curve and validated with respect experimental data obtained at Lawrence Berkeley National Laboratory (LBNL), when available.

Firstly, the single tape 2D model has been very validated under AC conditions, subjected to alternating transport current or magnetic field, against H-formulation, $A-H$-formulation, and the latest $A-H$ thin shell formulation. The model has been able to properly reproduced the same results of references as regards current distribution along the width and AC losses computed, with an average error 1.1%. Then, the same model has been used for the $V-I$ tape curve prediction, and extended to 3D dimension. Due to the translational symmetry, the problem is a 2D in principle, but the 3D model is necessary for more complex geometries, e.g. CORC® configuration. Here, it is used to verify the capability of reproducing the 2D results. The latter has been verified and benchmarked in self-field and for different applied field with a 2D magnetostatic model for the I_c prediction has been. The good agreement with reference proved the capability of the model to deal with the strong non-linearity of the problem. In self-field, the critical current value has a relative error about 1.35%, while just 0.36% with respect the magnetostatic model. To assess the ability of the current sharing condition to deal with external perturbances, it has been extended at CORC® geometry. To reduce the computational domain, the symmetry of the geometry has been exploited simulating the just the minimum computational domain, a single pitch of the cable. Periodic boundary conditions have been applied to avoid edge-effects. The current distribution and redistribution among tapes is computed self-consistently though the novel boundary condition, here called *current sharing condition*. This capability has been proved though a

benchmark with a 3D model based on H-formulation in a simple CORC® geometry. A single layer 2-tapes CORC® is modelled, in which one of the tapes has perturbed with a heat pulse. The comparison showed a good agreement with the reference. When the heating is starting and the temperature rises, the transport current rises in the second tape with the same rate on both formulation. The recovery is faster in the $T-A$ formulation with a maximum error of 8%. The thermal results are in perfect agreement with relative errors of the order of 0.1%. Pushing forward the capability of the model to deal with more complex geometry, a 6-tape CORC® model have been used to computed the $V-I$ curves, validated through experimental data. The 3-layers (6-tapes) straight CORC® wire $V-I$ curve is sharper than the measured one. Considering the tapering of tapes within the terminations and possible joule heat (which can be non-negligible on such short sample), dissipated again from the copper of the termination, pointed out how the measured I_c value is strongly affected by these parameters, not considered in the numerical model as first. The current injection is a well-know issue for CORC® conductors, for which research are trying to find a solution for low resistance joints. The last validation on the same tape reported in this work is 6-tapes bended CORC® wire, in self-field immersed in LN_2 bath, validated with measurements from LBNL. While, the I_c is well-captured, the n-value is largely overestimated (computed $V-I$ curve is again steeper than the measured one). Mainly, it is due to the strong influence of termination affecting the measurements, also in this case, and the too simplified strain evaluation. Finally, a further demonstration of the stability and reliability of the model has been obtained simulating a 6-layers CORC® , with $12-$tapes total. The critical current was perfectly captured by the simulation, with a relative error of 0.2%. This CORC® was composed of tapes from the same manufacturer, but with a lower initial critical current. Nonetheless, due to lack of information, the same scaling of the critical current has been use for the simulation. The entire $E-I$ curve is still sharper than the reference, but the numerical results are consistent with the physics of the problem. The discrepancy shows that the scaling of the critical current density might be generalized or that some aspects of the physics that are unclear and not considered. The model still needs more validation for different cable layout configurations and scenarios. In conclusion, the implemented model allows the prediction of transport performance and behavior of CORC® cables, consistent replication of the physics and, in perspective, it could help for improving the termination development.

5.1 Future perspectives

The main outcome of this research activity is the development of comprehensive multiphysics 3D model for CORC® like conductors. The model accurately describe the thermal, electric and magnetic behaviors of CORC® cables and wires, and, for the first time, the current sharing among tapes is included. Nevertheless, there are some improvements that needs to be implemented and exploring other direction which can help the characterization of CORC® critical current, for which this section is devoted. Firstly, the convergence and the complex implementation on the software are two major drawbacks to consider on simulation side. While, considering the high computation cost other path can be considered, not only for a single wire or cable, but in perspective of characterizing an entire magnet or coil composed of multiple CORC® . How the weakest zone can be defined?
The Artificial Intelligence (AI) or surrogate models might be a feasible answer to decreasing the computing cost and number of simulations necessary to predict the behavior of a CORC® cable. The goal is to use a black box model to define a small length of cable (cwhich we may called "CORC® cable element") as a function of the number of ReBCO tapes per layer, the number of layers, and the bending radius (parameters which strongly influence the cable performances). The neural network should be trained providing as input the magnetic field in which the HTS cable is submerged, the operating temperature, and the critical current validated by previous numerical simulations or experimental data, and the critical current is computed as an output. Once a "CORC® cable element" has been characterized, it can be used as a "spatial element" to discretize an entire component, as a CCT coil or CORC® -CICC, so that it could be possible to define the most critical point at different operating condition, saving time, memory and computational cost. The characterization of a magnet, defining critical zones and operating conditions, can help in designing more performant and reliable coils.

References

[1] S. Viarengo, F. Freschi, D. Placido, and L. Savoldi. Current distribution modeling in the open-source opensc2tool for the multi-physics analysis of hts and lts cables. *IEEE Transactions on Applied Superconductivity*, 32, 9 2022.

[2] Sofia Viarengo, Lucas Brouwer, Paolo Ferracin, Fabio Freschi, Nicolo Riva, Laura Savoldi, and Xiaorong Wang. A new coupled electrodynamic t - a and thermal model for the critical current characterization of high-temperature superconducting tapes and cables. *IEEE Access*, 11:107548–107561, 2023.

[3] H. Kamerlingh Onnes. *Further Experiments with Liquid Helium. D. On the Change of the Electrical Resistance of Pure Metals at very low Temperatures, etc. V. The Disappearance of the resistance of mercury*, pages 264–266. Springer Netherlands, Dordrecht, 1991.

[4] Neil Mitchell, Jinxing Zheng, Christian Vorpahl, Valentina Corato, Charlie Sanabria, Michael Segal, Brandon Sorbom, Robert Slade, Greg Brittles, Rod Bateman, Yasuyuki Miyoshi, Nobuya Banno, Kazuyoshi Saito, Anna Kario, Herman Ten Kate, Pierluigi Bruzzone, Rainer Wesche, Thierry Schild, Nikolay Bykovskiy, Alexey Dudarev, Matthias Mentink, Franco Julio Mangiarotti, Kamil Sedlak, David Evans, Danko C. Van Der Laan, Jeremy D. Weiss, Min Liao, and Gen Liu. Superconductors for fusion: A roadmap, 10 2021.

[5] W. Meissner and R. Ochsenfeld. Ein neuer effekt bei eintritt der supraleitfähigkeit. *Naturwissenschaften*, 21(44):787–788, November 1933.

[6] Micheal Tinkham. *Introduction to superconductivity*. Dover Publication, second edition edition, 2004.

[7] J. G. Bednorz and K. A. Muller. Possible high tc superconductivity in the ba-la-cu-o system. *Z. Phys. B*, 64:189–193, 1986.

[8] Nicolò Riva. *Quench behavior of high-temperature superconductor tapes for power applications: a strategy toward resilience*. PhD thesis, EPFL, 2019.

[9] Tim Mulder. *Advancing ReBCO-CORC Wire and Cable-in-Conduit Conductor Technology for Superconducting Magnets*. PhD thesis, University of Twente, 2022.

[10] Marco Bonura and Carmine Senatore. High-field thermal transport properties of rebco coated conductors. *Superconductor Science and Technology*, 28, 2 2015.

[11] Pia Jensen Ray. *Structural investigation of $La_{2-x}Sr_xCuO_{4+y}$: following a staging as a function of temperature*. Niels Bohr Institute, Copenhagen University, 2015.

[12] D. C. Larbalestier, J. Jiang, U. P. Trociewitz, F. Kametani, C. Scheuerlein, M. Dalban-Canassy, M. Matras, P. Chen, N. C. Craig, P. J. Lee, and E. E. Hellstrom. Isotropic round-wire multifilament cuprate superconductor for generation of magnetic fields above 30 t. *Nature Materials*, 13:375–381, 2014.

[13] W. Denis Markiewicz, David C. Larbalestier, Hubertus W. Weijers, Adam J. Voran, Ken W. Pickard, William R. Sheppard, Jan Jaroszynski, Aixia Xu, Robert P. Walsh, Jun Lu, Andrew V. Gavrilin, and Patrick D. Noyes. Design of a superconducting 32 t magnet with rebco high field coils. *IEEE Transactions on Applied Superconductivity*, 22, 2012.

[14] Jeroen Van Nugteren, Glyn Kirby, Jaakko Murtomaki, Gijs Derijk, Lucio Rossi, and Antti Stenvall. Toward rebco 20 t+ dipoles for accelerators. *IEEE Transactions on Applied Superconductivity*, 28, 6 2018.

[15] Yukikazu Iwasa. Hts magnets: Stability; protection; cryogenics; economics; current stability/protection activities at fbml. *Cryogenics*, 43:303–316, 3 2003.

[16] David Larbalestier, Alex Gurevich, D Matthew Feldmann, and Anatoly Polyanskii. High-t c superconducting materials for electric power applications. *Nature*, 414:368–377, 2001.

[17] Kenneth H. Sandhage, Gilbert N. Riley, and William L. Carter. Critical issues in the OPIT processing of high-Jc BSCCO superconductors. *JOM*, 43(3):21–25, March 1991.

[18] M. K. Wu, J. R. Ashburn, C. J. Torng, P. H. Hor, R. L. Meng, L. Gao, Z. J. Huang, Y. Q. Wang, and C. W. Chu. Superconductivity at 93 k in a new mixed-phase yb-ba-cu-o compound system at ambient pressure. *Physical Review Letters*, 58:908–910, 1987.

[19] Carmine Senatore. High temperature superconductors: From the materials to magnet technology, 2022.

[20] D. C. Van Der Laan, J. W. Ekin, C. C. Clickner, and T. C. Stauffer. Delamination strength of ybco coated conductors under transverse tensile stress. *Superconductor Science and Technology*, 20:765–770, 8 2007.

[21] Makoto Takayasu, Luisa Chiesa, Leslie Bromberg, and Joseph V. Minervini. Hts twisted stacked-tape cable conductor. *Superconductor Science and Technology*, 25, 1 2012.

[22] W. Goldacker, A. Frank, R. Heller, S. I. Schlachter, B. Ringsdorf, K. P. Weiss, C. Schmidt, and S. Schuller. Roebel assembled coated conductors (racc): Preparation, properties and progress. *IEEE Transactions on Applied Superconductivity*, 17:3398–3401, 6 2007.

[23] D. C. Van Der Laan, X. F. Lu, and L. F. Goodrich. Compact gdba2cu3o7-δ coated conductor cables for electric power transmission and magnet applications. *Superconductor Science and Technology*, 24, 4 2011.

[24] K. Yagotintsev, V. A. Anvar, P. Gao, M. J. Dhalle, T. J. Haugan, D. C. Van Der Laan, J. D. Weiss, M. S.A. Hossain, and A. Nijhuis. Ac loss and contact resistance in rebco corc®, roebel, and stacked tape cables. *Superconductor Science and Technology*, 33, 8 2020.

[25] Mahesh Paidpilli and Venkat Selvamanickam. Development of re-ba-cu-o superconductors in the u.s. for ultra-high field magnets. *Superconductor Science and Technology*, 35, 4 2022.

[26] Makoto Takayasu, Franco J. Mangiarotti, Luisa Chiesa, Leslie Bromberg, and Joseph V. Minervini. Conductor characterization of ybco twisted stacked-tape cables. *IEEE Transactions on Applied Superconductivity*, 23, 2013.

[27] G. Celentano, G. De Marzi, F. Fabbri, L. Muzzi, G. Tomassetti, A. Anemona, S. Chiarelli, M. Seri, A. Bragagni, and A. Della Corte. Design of an industrially feasible twisted-stack hts cable-in-conduit conductor for fusion application. *IEEE Transactions on Applied Superconductivity*, 24, 2014.

[28] L. Muzzi, A. Augieri, G. Celentano, S. Chiarelli, A. Della Corte, G. De Marzi, A. Di Zenobio, L. Giannini, M. Marchetti, A. Masi, G. Messina, A. Rufoloni, S. Turtu, A. Vannozzi, A. Bragagni, M. Seri, M. Arabi, A. Anemona, and A. Formichetti. Design and feasibility assessment of an hts sector shaped high-current conductor for fusion coils. *IEEE Transactions on Applied Superconductivity*, 33, 8 2023.

[29] D. Uglietti, N. Bykovsky, K. Sedlak, B. Stepanov, R. Wesche, and P. Bruzzone. Test of 60 ka coated conductor cable prototypes for fusion magnets. *Superconductor Science and Technology*, 28, 11 2015.

[30] N. Yanagi, S. Ito, Y. Terazaki, Y. Seino, S. Hamaguchi, H. Tamura, J. Miyazawa, T. Mito, H. Hashizume, and A. Sagara. Design and development of high-temperature superconducting magnet system with joint-winding for the helical fusion reactor. *Nuclear Fusion*, 55, 5 2015.

[31] Michael J. Wolf, Walter H. Fietz, Christoph M. Bayer, Sonja I. Schlachter, Reinhard Heller, and Klaus Peter Weiss. Hts croco: A stacked hts conductor optimized for high currents and long-length production. *IEEE Transactions on Applied Superconductivity*, 26:19–24, 3 2016.

[32] Yinshun Wang, Shiirav Baasansuren, Chi Xue, and Takayo Hasegawa. Development of a quasi-isotropic strand stacked by 2g wires. *IEEE Transactions on Applied Superconductivity*, 26, 6 2016.

[33] Zachary S. Hartwig, Rui F. Vieira, Brandon N. Sorbom, Rodney A. Badcock, Marta Bajko, William K. Beck, Bernardo Castaldo, Christopher L. Craighill, Michael Davies, Jose Estrada, Vincent Fry, Theodore Golfinopoulos, Amanda E. Hubbard, James H. Irby, Sergey Kuznetsov, Christopher J. Lammi, Philip C. Michael, Theodore Mouratidis, Richard A. Murray, Andrew T. Pfeiffer, Samuel Z. Pierson, Alexi Radovinsky, Michael D. Rowell, Erica E. Salazar, Michael Segal, Peter W. Stahle, Makoto Takayasu, Thomas L. Toland, and Lihua Zhou. Viper: An industrially scalable high-current high-temperature superconductor cable. *Superconductor Science and Technology*, 33, 11 2020.

[34] Ludwig Roebel. Germanpatent, bbccompany, 1912.

[35] W. Goldacker, R. Nast, G. Kotzyba, S. I. Schlachter, A. Frank, B. Ringsdorf, C. Schmidt, and P. Komarek. High current dybco-roebel assembled coated conductor (racc). *Journal of Physics: Conference Series*, 43:901–904, 6 2006.

[36] Nikolay Bykovskiy. *HTS high current cable for fusion application*. PhD thesis, EPFL, 2017.

[37] Jeroen Van Nugteren. *High Temperature Superconductor Accelerator Magnets*. PhD thesis, University of Twente, 2016.

[38] D. C. Van Der Laan. Yba2cu3o7-δ coated conductor cabling for low ac-loss and high-field magnet applications. *Superconductor Science and Technology*, 22, 2009.

[39] Jeremy D. Weiss, Tim Mulder, Herman J. Ten Kate, and Danko C. Van Der Laan. Introduction of corc® wires: Highly flexible, round high-temperature superconducting wires for magnet and power transmission applications. *Superconductor Science and Technology*, 30, 1 2017.

[40] Zichuan Guo, Jinggang Qin, R. Lubkemann, Keyang Wang, Huan Jin, Guanyu Xiao, Jiangang Li, Chao Zhou, and Arend Nijhuis. Ac loss and contact resistance in highly flexible rebco cable for fusion applications. *Superconductivity*, 2, 6 2022.

[41] Guanyu Xiao, Huan Jin, Chao Zhou, Hongjun Ma, Donghu Wang, Fang Liu, Huajun Liu, Arend Nijhuis, and Arnaud Devred. Performance of highly flexible sub-cable for rebco cable-in-conduit conductor at 5.8 t applied field. *Superconductivity*, 3, 9 2022.

[42] D. C. Van Der Laan, J. D. Weiss, and D. M. McRae. Status of corc® cables and wires for use in high-field magnets and power systems a decade after their introduction, 2 2019.

[43] Xiaorong Wang, Dmytro Abraimov, DIego Arbelaez, Timothy J. Bogdanof, Lucas Brouwer, Shlomo Caspi, Daniel R. DIetderich, Joseph DImarco, Ashleigh Francis, Laura Garcia Fajardo, William B. Ghiorso, Stephen A. Gourlay, Hugh C. Higley, Maxim Marchevsky, Maxwell A. Maruszewski, Cory S. Myers, Soren O. Prestemon, Tengming Shen, Jordan Taylor, Reed Teyber, Marcos Turqueti, Danko Van Der Laan, and Jeremy D. Weiss. Development and performance of a 2.9 tesla dipole magnet using high-temperature superconducting CORC® wires. *Superconductor Science and Technology*, 34, 1 2021.

[44] Tim Mulder, Jeremy Weiss, Danko Van Der Laan, Alexey Dudarev, and Herman Ten Kate. Recent progress in the development of corc cable-in-conduit conductors. *IEEE Transactions on Applied Superconductivity*, 30, 6 2020.

[45] F. Scurti, J. D. Weiss, D. C. Van Der Laan, and J. Schwartz. Smart conductor on round core (corc®) wire via integrated optical fibers. *Superconductor Science and Technology*, 34, 3 2021.

[46] Jeremy Weiss et al. Current progress of high-temperature superconducting CORC® magnet cable and wire development, 2017.

[47] L Bottura, C Rosso, and M Breschi. A general model for thermal, hydraulic and electric analysis of superconducting cables q. *Cryogenics*, 40, 2000.

[48] Rui Kang, Davide Uglietti, Rainer Wesche, Kamil Sedlak, Pierluigi Bruzzone, and Yuntao Song. Quench simulation of rebco cable-in-conduit conductor with twisted stacked-tape cable. *IEEE Transactions on Applied Superconductivity*, 30, 1 2020.

[49] Monika Lewandowska, Aleksandra Dembkowska, Reinhard Heller, and Michael Wolf. Thermal-hydraulic analysis of an hts demo tf coil. *Cryogenics*, 96:125–132, 12 2018.

[50] Andrea Zappatore, Walter H. Fietz, Reinhard Heller, Laura Savoldi, Michael J. Wolf, and Roberto Zanino. A critical assessment of thermal-hydraulic modeling of hts twisted-stacked-tape cable conductors for fusion applications. *Superconductor Science and Technology*, 32, 7 2019.

[51] M. Ciotti, A. Nijhuis, P. L. Ribani, L. Savoldi Richard, and R. Zanino. Thelma code electromagnetic model of iter superconducting cables and application to the enea stability experiment. *Superconductor Science and Technology*, 19:987–997, 10 2006.

[52] L. Savoldi Richard, F. Casella, B. Fiori, and R. Zanino. The 4c code for the cryogenic circuit conductor and coil modeling in iter. *Cryogenics*, 50:167–176, 3 2010.

[53] E. P.A. van Lanen and A. Nijhuis. Jackpot: A novel model to study the influence of current non-uniformity and cabling patterns in cable-in-conduit conductors. *Cryogenics*, 50:139–148, 3 2010.

[54] A. Zappatore, R. Heller, L. Savoldi, M. J. Wolf, and R. Zanino. A new model for the analysis of quench in hts cable-in-conduit conductors based on the twisted-stacked-tape cable concept for fusion applications. *Superconductor Science and Technology*, 33, 6 2020.

[55] Laura Savoldi, Daniele Placido, and Sofia Viarengo. Thermal-hydraulic analysis of superconducting cables for energy applications with a novel open object-oriented software: Opensc2. *Cryogenics*, 124, 6 2022.

[56] Luca Bottura, Marco Breschi, and Laura Savoldi. Does the shift to hts magnets for compact fusion reactors call for the development of a new generation of numerical tools?, 2023.

[57] Ernst Helmut Brandt. Superconductors of finite thickness in a perpendicular magnetic field: Strips and slabs. *Physical Review B*, 1996.

[58] Leonid Prigozhin. Analysis of critical-state problems in type-ii superconductivity. *IEEE TRANSACTIONS ON APPLIED SUPERCONDUCTIVITY*, 7, 1997.

[59] V.M. Vinokur, P.H. Kes, and A.E. Koshelev. Flux pinning and creep in very anistropic high temperature superconductors. *Physica C: Superconductivity*, 168(1):29–39, 1990.

[60] David Larbalestier. Critical Currents and Magnet Applications of High-Tc Superconductors. *Physics Today*, 44(6):74–82, 06 1991.

[61] Naoyuki Amemiya, Kengo Miyamoto, Nobuya Banno, and Osami Tsukamoto. Numerical analysis of ac losses in high tc superconductors based on e-j characteristics represented with n-value, 1997.

[62] M. Tsuda, T. Susa, T. Ohyama, A. Ishiyama, S. Kohayashi, and S. Haseyama. Electromagnetic behavior on high-temperature superconducting bulk ybco exposed to time-varying magnetic field. *IEEE Transactions on Applied Superconductivity*, 10(1):894–897, 2000.

[63] D. V. Shantsev, M. E. Gaevski, R. A. Suris, A. V. Bobyl, V. E. Gasumyants, and O. L. Shalaev. Temperature and magnetic-field dependence of the conductivity of $yba_2cu_3o_{7-\delta}$ films in the vicinity of the superconducting transition: Effect of T_c inhomogeneity. *Phys. Rev. B*, 60:12485–12494, Nov 1999.

[64] Francesco Grilli, Roberto Brambilla, Luciano F. Martini, Frédéric Sirois, Doan N. Nguyen, and Stephen P. Ashworth. Current density distribution in multiple ybco coated conductors by coupled integral equations. *IEEE Transactions on Applied Superconductivity*, 19:2859–2862, 6 2009.

[65] E. Pardo. Modeling of ac loss in coils made of thin tapes under dc bias current. *IEEE Transactions on Applied Superconductivity*, 24, 6 2014.

[66] Andrea Musso. *Analysis of electrodynamic transient in high temperature superconducting tapes and coils*. PhD thesis, Università di Bologna, 2021.

[67] A. M. Campbell. A new method of determining the critical state in superconductors. *Superconductor Science and Technology*, 20:292–295, 3 2007.

[68] M. P. Philippe, M. D. Ainslie, L. Wéra, J. F. Fagnard, A. R. Dennis, Y. H. Shi, D. A. Cardwell, B. Vanderheyden, and P. Vanderbemden. Influence of soft ferromagnetic sections on the magnetic flux density profile of a large grain, bulk y-ba-cu-o superconductor. *Superconductor Science and Technology*, 28, 9 2015.

[69] C. Lacroix and F. Sirois. Concept of a current flow diverter for accelerating the normal zone propagation velocity in 2g hts coated conductors. *Superconductor Science and Technology*, 27, 2014.

[70] E. Härö and A. Stenvall. Reducing modeling domain to speed-up quench simulations of hts coils. *IEEE Transactions on Applied Superconductivity*, 24, 2014.

[71] Erkki Haro, Antti Stenvall, Jeroen Van Nugteren, and Glyn Kirby. Modeling of minimum energy required to quench an hts magnet with a strip heater. *IEEE Transactions on Applied Superconductivity*, 25, 12 2015.

[72] Tiina Salmi. *Optimization of quench protection heater performance in high-field accelerator magnets through computational and experimental analysis*. PhD thesis, Tampere University of Technology, 2015.

[73] N. Riva, R. S. Granetz, R. Vieira, A. Hubbard, A. T. Pfeiffer, P. Harris, C. Chamberlain, Z. S. Hartwig, A. Watterson, D. Anderson, and R. Volberg. Development of the first non-planar rebco stellarator coil using viper cable. *Superconductor Science and Technology*, 36, 10 2023.

[74] Masahiro Nii, Naoyuki Amemiya, and Taketsune Nakamura. Three-dimensional model for numerical electromagnetic field analyses of coated superconductors and its application to roebel cables. *Superconductor Science and Technology*, 25, 11 2012.

[75] Francesco Grilli, Roberto Brambilla, Frédéric Sirois, Antti Stenvall, and Steeve Memiaghe. Development of a three-dimensional finite-element model for high-temperature superconductors based on the h-formulation. *Cryogenics*, 53:142–147, 1 2013.

[76] H. Zhang, J. Zhu, W. Yuan, M. Qiu, S. Fu, S. Rao, W. Yang, and M. Zhang. Electromagnetic analysis of ybco superconducting cables with high current transporting for electric devices. *IEEE Transactions on Applied Superconductivity*, 26, 10 2016.

[77] Victor M.R. Zermeno, Francesco Grilli, and Frederic Sirois. A full 3d time-dependent electromagnetic model for roebel cables. *Superconductor Science and Technology*, 26, 5 2013.

[78] V. Zermeño, F. Sirois, M. Takayasu, M. Vojenciak, A. Kario, and F. Grilli. A self-consistent model for estimating the critical current of superconducting devices. *Superconductor Science and Technology*, 28, 8 2015.

[79] F. Gömöry and B. Klinok. Self-field critical current of a conductor with an elliptical cross-section. *Superconductor Science and Technology*, 19:732–737, 8 2006.

[80] T. Mulder, D. Van Der Laan, J. D. Weiss, A. Dudarev, M. Dhallé, and H. H.J. Ten Kate. Design and preparation of two rebco-corc® cable-in-conduit conductors for fusion and detector magnets. *IOP Conference Series: Materials Science and Engineering*, 279, 12 2017.

[81] Carmine Senatore, Christian Barth, Marco Bonura, Miloslav Kulich, and Giorgio Mondonico. Field and temperature scaling of the critical current density in commercial rebco coated conductors. *Superconductor Science and Technology*, 29, 1 2016.

[82] Y B Kim, C F Hempstead, and A R Strnad. Critical persistent currents in hard superconductors, 1962.

[83] D Dimos, P Chaudhari, J Mannhart, and F K Legoues. Orientation dependence of grain-boundary critical currents in $yba_2cu_3o_7 - \delta$ bicrystals. *Physical Review Letters*, 61, 1988.

[84] D. Matthew Feldmann, Terry G. Holesinger, Ron Feenstra, and David C. Larbalestier. A review of the influence of grain boundary geometry on the electromagnetic properties of polycrystalline yba2cu3o7-x films. *Journal of the American Ceramic Society*, 91:1869–1882, 6 2008.

[85] Y. Iijima, N. Tanabe, O. Kohno, and Y. Ikeno. In-plane aligned yba2cu3o7-x thin films deposited on polycrystalline metallic substrates. *Applied Physics Letters*, 60:769–771, 1992.

[86] A. Goyal, D. P. Norton, J. D. Budai, M. Paranthaman, E. D. Specht, D. M. Kroeger, D. K. Christen, Q. He, B. Saffian, F. A. List, D. F. Lee, P. M. Martin, C. E. Klabunde, E. Hartfield, and V. K. Sikka. High critical current density superconducting tapes by epitaxial deposition of yba2cu3ox thick films on biaxially textured metals. *Applied Physics Letters*, 69:1795–1797, 9 1996.

[87] C. P. Wang, K. B. Do, M. R. Beasley, T. H. Geballe, and R. H. Hammond. Deposition of in-plane textured mgo on amorphous si3n4 substrates by ion-beam-assisted deposition and comparisons with ion-beam-assisted deposited yttria-stabilized-zirconia, 11 1997.

[88] B Ma, M Li, Y A Jee, R E Koritala, B L Fisher, and U Balachandran. Inclined-substrate deposition of biaxially textured magnesium oxide thin films for ybco coated conductors. *Physica C*, 366:270–276, 2016.

[89] Patrick Pahlke, Max Sieger, Paul Chekhonin, Werner Skrotzki, Jens Hanisch, Alexander Usoskin, Jan Stromer, Ludwig Schultz, and Ruben Huhne. Local orientation variations in ybco films on technical substrates-a combined sem and ebsd study. *IEEE Transactions on Applied Superconductivity*, 26, 4 2016.

[90] Amit Goyal, M. Parans Paranthaman, and U. Schoop. The RABiTS Approach: Using Rolling-Assisted Biaxially Textured Substrates for High-Performance YBCO Superconductors. *MRS Bulletin*, 29(8):552–561, aug 2004.

[91] P C Chou, Q Zhong, Q L Li, K Abazajian, A Ignatiev, C Y Wang, E E Deal, and J G Chen. Optimization of jc of ybco thin films prepared by photo-assisted mocvd through statistical robust design, 1995.

[92] A. Gupta, R. Jagannathan, E. I. Cooper, E. A. Giess, J. I. Landman, and B. W. Hussey. Superconducting oxide films with high transition temperature prepared from metal trifluoroacetate precursors. *Applied Physics Letters*, 52:2077–2079, 1988.

[93] K Hasegawa, K Fujino, H Mukai, M Konishi, K Hayashi, K Sato, S Honjo, Y Sato6, H Ishii, and Y Iwata. Biaxially aligne ybco film tapes fabricated by all pulsed laser deposition. *IEEE Transactions on Applied Superconductivity*, 4:487–493, 1996.

[94] Vladimir Matias, E. John Rowley, Yates Coulter, B. Maiorov, Terry Holesinger, Chris Yung, Viktor Glyantsev, and Brian Moeckly. Ybco films grown by reactive co-evaporation on simplified ibad-mgo coated conductor templates. *Superconductor Science and Technology*, 23, 2010.

[95] C. Barth, G. Mondonico, and C. Senatore. Electro-mechanical properties of rebco coated conductors from various industrial manufacturers at 77 k, self-field and 4.2 k, 19 t. *Superconductor Science and Technology*, 28, 4 2015.

[96] K. Tsuchiya, A. Kikuchi, A. Terashima, K. Norimoto, M. Uchida, M. Tawada, M. Masuzawa, N. Ohuchi, X. Wang, T. Takao, and S. Fujita. Critical current measurement of commercial rebco conductors at 4.2 k. *Cryogenics*, 85:1–7, 7 2017.

[97] Kiyosumi Tsuchiya, Xudong Wang, Shinji Fujita, Ataru Ichinose, Kyohei Yamada, Akio Terashima, and Akihiro Kikuchi. Superconducting properties of commercial rebco-coated conductors with artificial pinning centers. *Superconductor Science and Technology*, 34, 10 2021.

[98] Guangyu Jiang, Yue Zhao, Jiamin Zhu, Yiming Hong, Chunsheng Chen, Sikan Chen, Yue Wu, Shuiliang Zhen, Linpeng Yao, Zhiyong Hong, Zhijian Jin, and Yutaka Yamada. Recent development and mass production of high j e 2g-hts

tapes by using thin hastelloy substrate at shanghai superconductor technology. *Superconductor Science and Technology*, 33, 7 2020.

[99] Naoyuki Amemiya, Satoshi Kasai, Keiji Yoda, Zhenan Jiang, George A. Levin, Paul N. Barnes, and Charles E. Oberly. Ac loss reduction of ybco coated conductors by multifilamentary structure. *Superconductor Science and Technology*, 17:1464–1471, 12 2004.

[100] Tetsuya Ito, Masataka Iwakuma, Shun Miura, Teruo Izumi, Kazuhisa Adachi, Takato Machi, and Akira Ibi. Difference of ac losses between nonstriated and striated tape and applicability of temperature scaling law to stacked striated tape. *IEEE Transactions on Applied Superconductivity*, 28, 4 2018.

[101] A. C. Wulff, A. B. Abrahamsen, and A. R. Insinga. Multifilamentary coated conductors for ultra-high magnetic field applications, 5 2021.

[102] J. Šouc, F. Gömöry, J. Kováč, R. Nast, A. Jung, M. Vojenčiak, F. Grilli, and W. Goldacker. Low ac loss cable produced from transposed striated cc tapes. *Superconductor Science and Technology*, 26, 7 2013.

[103] M. Vojenčiak, A. Kario, B. Ringsdorf, R. Nast, D. C. Van Der Laan, J. Scheiter, A. Jung, B. Runtsch, F. Gömöry, and W. Goldacker. Magnetization ac loss reduction in hts corc® cables made of striated coated conductors. *Superconductor Science and Technology*, 28, 9 2015.

[104] Wenrong Li, Jie Sheng, Jinxing Zheng, Yue Wu, Chunjiang Guo, Zhuyong Li, and Zhijian Jin. Study on reducing magnetization loss in corc cables by laser cutting technology. *IEEE Transactions on Applied Superconductivity*, 31, 6 2021.

[105] Naoyuki Amemiya, Mao Shigemasa, Akira Takahashi, Ning Wang, Yusuke Sogabe, Satoshi Yamano, and Hisaki Sakamoto. Effective reduction of magnetisation losses in copper-plated multifilament coated conductors using spiral geometry. *Superconductor Science and Technology*, 35, 2 2022.

[106] Zuoguang Li, Zhan Zhang, Shaoqing Wei, Peng Gao, Yuhu Bu, Donghu Wang, Guanyu Xiao, Jiahao Wan, Huan Jin, Jinggang Qin, and Chao Zhou. Performance study of rebco multi-filament tapes/corc cables prepared by reel-to-reel mechanical incision. *Cryogenics*, 139:103799, 2024.

[107] Wei Pi, Anpeng Shu, Yukang Shen, Qiyue Wang, Heng Zhang, Yinshun Wang, and Qingmei Shi. Magnetic field angle dependence of critical current in rebco tapes produced by different techniques. *IEEE Transactions on Applied Superconductivity*, pages 1–6, 2 2024.

[108] J. F. Maguire, F. Schmidt, S. Bratt, T. E. Welsh, J. Yuan, A. Allais, and F. Hamber. Development and demonstration of a hts power cable to operate in the long island power authority transmission grid. *IEEE Transactions on Applied Superconductivity*, 17:2034–2037, 6 2007.

[109] Peifeng Gao, Jiali Mao, Jiaxiang Chen, Xingzhe Wang, and Youhe Zhou. Electromechanical degradation of rebco coated conductor tapes under combined tension and torsion loading. *International Journal of Mechanical Sciences*, 223, 6 2022.

[110] D. C. Van Der Laan, D. Abraimov, A. A. Polyanskii, D. C. Larbalestier, J. F. Douglas, R. Semerad, and M. Bauer. Anisotropic in-plane reversible strain effect in $y_{0.5}gd_{0.5}ba_2cu_3o_{7-\delta}$ coated conductors. *Superconductor Science and Technology*, 24, 11 2011.

[111] Hyung Seop Shin, Ki Hyun Kim, John Ryan C. Dizon, Tae Young Kim, Rock Kil Ko, and Sang Soo Oh. The strain effect on critical current in ybco coated conductors with different stabilizing layers. *Superconductor Science and Technology*, 18, 12 2005.

[112] Guanyu Xiao, Chao Zhou, Jinggang Qin, Huan Jin, Haihong Liu, and Chuanyi Zhao. Critical current degradation behaviour of various rebco tapes under uniaxial strain. *Fusion Engineering and Design*, 190, 5 2023.

[113] D. C. Van Der Laan and J. W. Ekin. Large intrinsic effect of axial strain on the critical current of high-temperature superconductors for electric power applications. *Applied Physics Letters*, 90, 2007.

[114] D. C. Van Der Laan, J. W. Ekin, J. F. Douglas, C. C. Clickner, T. C. Stauffer, and L. F. Goodrich. Effect of strain, magnetic field and field angle on the critical current density of $yba_2cu_3o_{7-\delta}$ coated conductors. *Superconductor Science and Technology*, 23, 2010.

[115] Michinaka Sugano, Kouji Shikimachi, Naoki Hirano, and Shigeo Nagaya. The reversible strain effect on critical current over a wide range of temperatures and magnetic fields for ybco coated conductors. *Superconductor Science and Technology*, 23:085013, 8 2010.

[116] C. Zhou, K. A. Yagotintsev, P. Gao, T. J. Haugan, D. C. Van Der Laan, and A. Nijhuis. Critical current of various rebco tapes under uniaxial strain. *IEEE Transactions on Applied Superconductivity*, 26, 6 2016.

[117] Simon Otten, Anna Kario, Andrea Kling, and Wilfried Goldacker. Bending properties of different rebco coated conductor tapes and roebel cables at t = 77 k. *Superconductor Science and Technology*, 29, 10 2016.

[118] Rui He, Yunfei Tan, Ziyi Huang, Yiming Xie, Guangda Wang, Yifan Wang, Qiong Wu, and Junwen Wei. Bending and uniaxial tensile strain effects on the critical current of rebco coated conductor tapes. *Cryogenics*, 116, 6 2021.

[119] Y. Zhang, D. W. Hazelton, R. Kelley, M. Kasahara, R. Nakasaki, H. Sakamoto, and A. Polyanskii. Stress-strain relationship, critical strain (stress) and irreversible strain (stress) of ibad-mocvd-based 2g hts wires under uniaxial tension. *IEEE Transactions on Applied Superconductivity*, 26, 6 2016.

[120] Tomoaki Takao, Sho Koizuka, Kazuki Oi, Atsushi Ishiyama, Junko Kato, Takato Machi, Koichi Nakao, and Yu Shiohara. Characteristics of compressive strain and superconducting property in ybco coated conductor. *IEEE Transactions on Applied Superconductivity*, 17:3517–3519, 6 2007.

[121] Xiaorong Wang, Diego Arbelaez, Shlomo Caspi, Soren O. Prestemon, Gian Luca Sabbi, and Tengming Shen. Strain distribution in rebco-coated conductors bent with the constant-perimeter geometry. *IEEE Transactions on Applied Superconductivity*, 27, 12 2017.

[122] D. Uglietti. A review of commercial high temperature superconducting materials for large magnets: From wires and tapes to cables and conductors. *Superconductor Science and Technology*, 32, 4 2019.

[123] R. Grabovickic, J.W. Lue, M.J. Gouge, J.A. Demko, and R.C. Duckworth. Measurements of temperature dependence of the stability and quench propagation of a 20-cm-long rabits y-ba-cu-o tape. *IEEE Transactions on Applied Superconductivity*, 13(2):1726–1730, 2003.

[124] N. Bykovskiy, H. Bajas, O. Dicuonzo, P. Bruzzone, and K. Sedlak. Experimental study of stability, quench propagation and detection methods on 15 ka sub-scale hts fusion conductors in sultan. *Superconductor Science and Technology*, 36, 3 2023.

[125] D. C. Van Der Laan, J. F. Douglas, C. C. Clickner, T. C. Stauffer, L. F. Goodrich, and H. J.N. Van Eck. Evidence that the reversible strain effect on critical current density and flux pinning in bi2sr2ca 2cu3ox tapes is caused entirely by the pressure dependence of the critical temperature. *Superconductor Science and Technology*, 24, 2011.

[126] Bennie ten Haken, Andrt Beuink, and Herman H J ten Kate. Small and repetitive axial strain reducing the critical current in bscco/ag superconductors. *IEEE TRANSACTIONS ON APPLIED SUPERCONDUCTIVITY*, 7, 1997.

[127] D. C. Van Der Laan, J. D. Weiss, P. Noyes, U. P. Trociewitz, A. Godeke, D. Abraimov, and D. C. Larbalestier. Record current density of 344 a mm-2 at 4.2 k and 17 t in corc® accelerator magnet cables. *Superconductor Science and Technology*, 29, 4 2016.

[128] Tim Mulder, Jeremy Weiss, Danko Van Der Laan, Marc Dhallé, and Herman Ten Kate. Development of rebco-corc wires with current densities of 400-600 a/mm2 at 10 t and 4.2 k. *IEEE Transactions on Applied Superconductivity*, 28, 4 2018.

[129] Advanced conductor and technology, 2011.

[130] G. P. Willering, D. C. Van Der Laan, H. W. Weijers, P. D. Noyes, G. E. Miller, and Y. Viouchkov. Effect of variations in terminal contact resistances on the current distribution in high-temperature superconducting cables. *Superconductor Science and Technology*, 28, 3 2015.

[131] Danko Van Der Laan, Fraser Douglas, Xifeng Lu, Ulf Trociewitz, and David Larbalestier. Conductor on round core (corc) cable development for accelerator magnets, 2014.

[132] van der Laan. Application data (60) provisional application no. 61 / 835 , 472 , filed on, 2013.

[133] D. C. Van Der Laan, J. D. Weiss, C. H. Kim, L. Graber, and S. Pamidi. Development of corc® cables for helium gas cooled power transmission and fault current limiting applications. *Superconductor Science and Technology*, 31, 7 2018.

[134] Jeremy D. Weiss, Chul Kim, Sastry Pamidi, and Danko C. Van Der Laan. Hybrid superconducting fault current limiting corc® wires with millisecond response time. *Superconductor Science and Technology*, 32, 2 2019.

[135] Nathaly Castaneda, Paolo Ferracin, Cyrus Funkhouser, Eduard Galstyan, Hugh C. Higley, Sri Ram Korupolu, Goran Majkic, Hoang Nguyen, Soren O. Prestemon, Venkat Selvamanickam, Huy Truong, and Xiaorong Wang. A 6-around-1 cable using high-temperature superconducting star® wires for magnet applications. *Superconductor Science and Technology*, 37, 3 2024.

[136] P. Rodriguez-Fernandez, A. J. Creely, M. J. Greenwald, D. Brunner, S. B. Ballinger, C. P. Chrobak, D. T. Garnier, R. Granetz, Z. S. Hartwig, N. T. Howard, J. W. Hughes, J. H. Irby, V. A. Izzo, A. Q. Kuang, Y. Lin, E. S. Marmar, R. T. Mumgaard, C. Rea, M. L. Reinke, V. Riccardo, J. E. Rice, S. D. Scott, B. N. Sorbom, J. A. Stillerman, R. Sweeney, R. A. Tinguely, D. G. Whyte, J. C. Wright, and D. V. Yuryev. Overview of the sparc physics basis towards the exploration of burning-plasma regimes in high-field, compact tokamaks. *Nuclear Fusion*, 62, 9 2022.

[137] V. Corato, C. Vorpahl, K. Sedlak, V. A. Anvar, J. Bennet, M. E. Biancolini, F. Bonne, R. Bonifetto, D. P. Boso, A. Brighenti, P. Bruzzone, G. Celentano, A. della Corte, G. De Marzi, V. D'Auria, F. Dematté, A. Dembkowska, O. Dicuonzo, C. Fiamozzi Zignani, W. H. Fietz, C. Frittitta, L. Giannini, F. Giorgetti, R. Guarino, R. Heller, C. Hoa, M. Huguet, G. Jiolat, M. Kumar, B. Lacroix, M. Lewandowska, N. Misiara, L. Morici, L. Muzzi, D. S. Nickel, S. Nicollet, A. Nijhuis, F. Nunio, C. Portafaix, X. Sarasola, L. Savoldi, I. Tiseanu, G. Tomassetti, A. Torre, S. Turtù, D. Uglietti, R. Vallcorba, K. P. Weiss, R. Wesche, M. J. Wolf, K. Yagotintsev, L. Zani, R. Zanino, and A. Zappatore. The demo magnet system – status and future challenges. *Fusion Engineering and Design*, 174, 1 2022.

[138] D.I. Meyer and R. Flasck. A new configuration for a dipole magnet for use in high energy physics applications. *Nuclear Instruments and Methods*, 80(2):339–341, 1970.

[139] S. Caspi, F. Borgnolutti, L. Brouwer, D. Cheng, R. D. Dietderich, H. Felice, A. Godeke, R. Hafalia, M. Martchevskii, S. Prestemon, E. Rochepault,

C. Swenson, and X. Wang. Canted-cosine-theta magnet (cct)-a concept for high field accelerator magnets. *IEEE Transactions on Applied Superconductivity*, 24, 2014.

[140] Xiaorong Wang, Shlomo Caspi, Daniel R. Dietderich, William B. Ghiorso, Stephen A. Gourlay, Hugh C. Higley, Andy Lin, Soren O. Prestemon, Danko Van Der Laan, and Jeremy D. Weiss. A viable dipole magnet concept with rebco corc® wires and further development needs for high-field magnet applications. *Superconductor Science and Technology*, 31, 3 2018.

[141] Lucas Nathan Brouwer. *Canted-Cosine-Theta Superconducting Accelerator Magnets for High Energy Physics and Ion Beam Cancer Therapy*. PhD thesis, University of California, Berkeley, 2015.

[142] S. Viarengo, F. Freschi, and L. Savoldi. Corc cables: Numerical characterization of the critical current after bending. *IEEE Transactions on Applied Superconductivity*, 34:1–5, 8 2024.

[143] Huiming Zhang, Min Zhang, and Weijia Yuan. An efficient 3d finite element method model based on the t-a formulation for superconducting coated conductors. *Superconductor Science and Technology*, 30, 2 2017.

[144] M. U. Fareed, M. Kapolka, B. C. Robert, M. Clegg, and H. S. Ruiz. 3d fem modeling of corc commercial cables with bean's like magnetization currents and its ac-losses behavior. *IEEE Transactions on Applied Superconductivity*, 32, 6 2022.

[145] J. Zhao, S. Y. Gao, B. H. Wu, X. S. Yang, B. Shen, W. Chen, and Y. Zhao. Effect of winding methods: transport ac losses in corc coils. *Superconductor Science and Technology*, 35, 11 2022.

[146] Yueyin Wang, Yinshun Wang, Defu Wei, Tie Guo, Yiran Meng, Jiuke Wang, and Changtao Kan. Ac losses of a like-corc conductor using accelerated 3d t-a model. *Physica C: Superconductivity and its Applications*, 579, 12 2020.

[147] Mengyuan Tian, Jiabin Yang, Boyang Shen, Yavuz Ozturk, Jun Ma, Chao Li, Jintao Hu, Haigening Wei, Junshi Li, and Tim Coombs. Analysis on the effect of superconductor layer thickness on the ac loss of conductor on round core (corc) cables. *IEEE Transactions on Applied Superconductivity*, 31, 11 2021.

[148] Yawei Wang, Min Zhang, Francesco Grilli, Zixuan Zhu, and Weijia Yuan. Study of the magnetization loss of corc® cables using a 3d t-a formulation. *Superconductor Science and Technology*, 32, 2 2019.

[149] Reed Teyber, Maxim Marchevsky, Aurora Cecilia Araujo Martinez, Soren Prestemon, Jeremy Weiss, and Danko Van Der Laan. Numerical investigation of current distributions around defects in high temperature superconducting corc®cables. *Superconductor Science and Technology*, 35, 9 2022.

[150] Xianhao Li, Li Ren, Ying Xu, Jing Shi, Xiaogang Chen, Guilun Chen, Yuejin Tang, and Jingdong Li. Calculation of corc cable loss using a coupled electromagnetic-thermal t-a formulation model. *IEEE Transactions on Applied Superconductivity*, 31, 6 2021.

[151] Xianhao Li, Li Ren, Ying Xu, Jiajie Long, Jing Shi, Guilun Chen, Yi Yue, and Yuejin Tang. Study on the influence of thermal and magnetic field on corc cable properties by a 2d model. *IEEE Transactions on Applied Superconductivity*, 31, 11 2021.

[152] Sijian Wang, Huadong Yong, and Youhe Zhou. Calculations of the ac losses in superconducting cables and coils: Neumann boundary conditions of the t-a formulation. *Superconductor Science and Technology*, 35, 6 2022.

[153] Boyang Shen, Xiaoyuan Chen, Lin Fu, Mingshun Zhang, Yu Chen, Jie Sheng, Zhen Huang, Wei Wang, Yujia Zhai, Yupeng Yuan, Wafa Ali Soomro, Youguang Guo, Xingming Bian, Hongwei Liu, Yavuz Ozturk, Mengyuan Tian, Luning Hao, Jintao Hu, Haigening Wei, Adil Shah, Ismail Patel, Jiabin Yang, and Tim Coombs. A simplified model of the field dependence for hts conductor on round core (corc) cables. *IEEE Transactions on Applied Superconductivity*, 31, 11 2021.

[154] Zixuan Zhu. *Advanced 3D and 2D Modelling of HTS CORC Cable based on the T-A Formulation for the Propulsion System of Hybrid-Electric Aircraft*. PhD thesis, University of Bath, 2020.

[155] Roberto Brambilla, Francesco Grilli, and Luciano Martini. Development of an edge-element model for ac loss computation of high-temperature superconductors. *Superconductor Science and Technology*, 20:16–24, 1 2007.

[156] Z. Hong, A. M. Campbell, and T. A. Coombs. Numerical solution of critical state in superconductivity by finite element software. *Superconductor Science and Technology*, 19:1246–1252, 11 2006.

[157] M. U. Fareed, M. Kapolka, B. C. Robert, M. Clegg, and H. S. Ruiz. 3d modelling and validation of the optimal pitch in commercial corc cables. *IOP Conference Series: Materials Science and Engineering*, 1241:012030, 5 2022.

[158] Y. Ichiki and H. Ohsaki. Numerical analysis of ac losses in ybco coated conductor in external magnetic field. In *Physica C: Superconductivity and its Applications*, volume 412-414, pages 1015–1020, 10 2004.

[159] Katsutoku Takeuchi, Naoyuki Amemiya, Taketsune Nakamura, Osamu Maruyama, and Takeshi Ohkuma. Model for electromagnetic field analysis of superconducting power transmission cable comprising spiraled coated conductors. *Superconductor Science and Technology*, 24(8):085014, jul 2011.

[160] Takashi Mifune, Naoki Tominaga, Yusuke Sogabe, Yudai Mizobata, Masahiro Yasunaga, Akihiro Ida, Takeshi Iwashita, and Naoyuki Amemiya. Large-scale electromagnetic field analyses of coils wound with coated conductors

using a current-vector-potential formulation with a thin-strip approximation. *Superconductor Science and Technology*, 32(9):094002, jul 2019.

[161] Yawei Wang, Jinxing Zheng, Zixuan Zhu, Min Zhang, and Weijia Yuan. Quench behavior of high temperature superconductor (re)ba 2 cu 3 o x corc cable, 2019.

[162] Zixuan Zhu, Yawei Wang, Dong Xing, Xiaoze Pei, Min Zhang, and Weijia Yuan. Quench of a single-layer rebco corc cable with non-uniform terminal contact resistance. *IEEE Transactions on Applied Superconductivity*, 29, 8 2019.

[163] Ashok Kb, Rijo Jacob Thomas, Jose Prakash Mathai, and Arend Nijhuis. Analytical and numerical investigations on the degradation of rebco based superconducting tapes under bending. *IEEE Transactions on Applied Superconductivity*, 31, 10 2021.

[164] Keyang Wang, Wurui Ta, and Yuanwen Gao. The winding mechanical behavior of conductor on round core cables. *Physica C: Superconductivity and its Applications*, 553:65–71, 10 2018.

[165] Federica Pierro, Zijia Zhao, Casey M. Owen, Christopher Colcord, Luisa Chiesa, Hugh C. Higley, Xiaorong Wang, and Soren O. Prestemon. Finite-element analysis of the strain distribution due to bending in a rebco coated conductor for canted cosine theta dipole magnet applications. *IEEE Transactions on Applied Superconductivity*, 29, 8 2019.

[166] K. B. Ashok, R. J. Thomas, M. Jose Prakash, and A. Nijhuis. Performance limits in rebco tape for variation in winding parameters of corc® cable and wire. *Physica C: Superconductivity and its Applications*, 582, 3 2021.

[167] K. B. Ashok, Rijo Jacob Thomas, Jose Prakash Mathai, and Arend Nijhuis. Influence of combined tension and torsion on the performance of rebco superconducting tapes. *IEEE Transactions on Applied Superconductivity*, 33, 4 2023.

[168] S Y Gao, S J Shi, X S Yang, B Y Shen, X B Hu, Y P Zhu, B H Wu, and Y Zhao. Hts conductor coil by in-situ winding technology for large-scale high-field magnet. *Superconductor Science and Technology*, 36:115029, 11 2023.

[169] V. A. Anvar, K. Ilin, K. A. Yagotintsev, B. Monachan, K. B. Ashok, B. A. Kortman, B. Pellen, T. J. Haugan, J. D. Weiss, D. C. Van Der Laan, R. J. Thomas, M. Jose Prakash, M. S.A. Hossain, and A. Nijhuis. Bending of corc® cables and wires: Finite element parametric study and experimental validation. *Superconductor Science and Technology*, 31, 10 2018.

[170] Jiangtao Yan, Keyang Wang, Yuanwen Gao, Youhe Zhou, and Arend Nijhuis. Investigating the effect of transverse compressive loads on the electromagnetic

performance of superconducting corc® cables. *Superconductor Science and Technology*, 35, 11 2022.

[171] K. Wang, Y. W. Gao, V. A. Anvar, K. Radcliff, J. D. Weiss, D. C. van der Laan, Y. H. Zhou, and A. Nijhuis. Prediction of strain, inter-layer interaction and critical current in corc® wires under axial strain by t-a modeling. *Superconductor Science and Technology*, 35, 10 2022.

[172] Christian Messe, Nicolò Riva, Sofia Viarengo, Gregory Giard, and Frédéric Sirois. Belfem: a special purpose finite element code for the magnetodynamic modeling of high-temperature superconducting tapes. *Superconductor Science and Technology*, 36, 11 2023.

[173] Fabio Freschi, Laura Savoldi, and Sofia Viarengo. Nonlinear magneto-quasistatic simulation of superconducting tapes with $a-\psi$ algebraic formulation. *IEEE Transactions on Magnetics*, 2023.

[174] Mehmet Burak Ozakin and Serkan Aksoy. Application of magneto-quasistatic approximation in the finite difference time domain method. *IEEE Transactions on Magnetics*, 52, 8 2016.

[175] Alexandre Arsenault, Bruno De Sousa Alves, Gregory Giard, and Frederic Sirois. Magnetodynamic $h-\phi$ formulation for improving the convergence and speed of numerical simulations of superconducting materials. *IEEE Transactions on Applied Superconductivity*, 33, 10 2023.

[176] N. Riva, A. Halbach, M. Lyly, C. Messe, J. Ruuskanen, and V. Lahtinen. H-o formulation in sparselizard combined with domain decomposition methods for modeling superconducting tapes, stacks, and twisted wires. *IEEE Transactions on Applied Superconductivity*, 33, 8 2023.

[177] M. Pellikka, S. Suuriniemi, L. Kettunen, and C. Geuzaine. Homology and cohomology computation in finite element modeling. *SIAM Journal on Scientific Computing*, 35, 2013.

[178] Julien Dular, Mane Harutyunyan, Lorenzo Bortot, Sebastian Schops, Benoit Vanderheyden, and Christophe Geuzaine. On the stability of mixed finite-element formulations for high-temperature superconductors. *IEEE Transactions on Applied Superconductivity*, 31, 9 2021.

[179] Alexandre Arsenault, Bruno De Sousa Alves, and Frederic Sirois. Comsol implementation of the h-ø-formulation with thin cuts for modeling superconductors with transport currents. *IEEE Transactions on Applied Superconductivity*, 31, 9 2021.

[180] E. Tonti. *The Mathematical Structure of Classical and Relativis- tic Physics: A General Classification Diagram*. Birkhäuser, New York, NY, 2013.

[181] X. Zhang, Z. Zhong, J. Geng, B. Shen, J. Ma, C. Li, H. Zhang, Q. Dong, and T. A. Coombs. Study of critical current and n-values of 2g hts tapes: Their magnetic field-angular dependence. *Journal of Superconductivity and Novel Magnetism*, 31:3847–3854, 12 2018.

[182] Arup K. Ghosh. V-i transition and n-value of multifilamentary lts and hts wires and cables. *Physica C: Superconductivity and its Applications*, 401:15–21, 1 2004.

[183] Bright Chimezie Robert, Muhammad Umar Fareed, and Harold Steven Ruiz. How to choose the superconducting material law for the modelling of 2g-hts coils. *Materials*, 12, 2019.

[184] A. Badía-Majós and C. López. Modelling current voltage characteristics of practical superconductors. *Superconductor Science and Technology*, 28, 2 2015.

[185] Kailash Prasad Thakur, Ashish Raj, Ernst Helmut Brandt, Jozef Kvitkovic, and Sastry V. Pamidi. Frequency-dependent critical current and transport ac loss of superconductor strip and roebel cable. *Superconductor Science and Technology*, 24, 6 2011.

[186] X. Zhang, Z. Zhong, H. S. Ruiz, J. Geng, and T. A. Coombs. General approach for the determination of the magneto-angular dependence of the critical current of ybco coated conductors. *Superconductor Science and Technology*, 30, 2 2017.

[187] G. Blatter, M. Y. Feigel'man, L. D. Landau, Y. B. Geshkenbein, A. I Larkin, and V. M. Vinokur. Vortices in high-temperature superconductors. *Review on Modern Physics*, 66:1125 – 1388, 1994.

[188] Qianfu Wang, Ping Jiang, Meng Li, Yaoyao Zhao, Shudong Zhang, Xuefeng Zhang, and Yimin Chen. Temperature dependence of transport critical current density for rebco superconducting tapes deposited by mocvd. *Superconductor Science and Technology*, 37, 1 2024.

[189] Jérôme Fleiter and Amalia Ballarino. In-field electrical resistance at 4.2 k of rebco splices. *IEEE Transactions on Applied Superconductivity*, 27, 6 2017.

[190] Marco Casali. *Experimental Analysis and Numerical Simulation of Quench in Superconducting HTS Tapes and Coils*. PhD thesis, Università di Bologna, 2015.

[191] Francesco Grilli, Frederic Sirois, Victor M.R. Zermeno, and Michal Vojenciak. Self-consistent modeling of the ic of hts devices: How accurate do models really need to be? *IEEE Transactions on Applied Superconductivity*, 24, 12 2014.

[192] X. Wang, D. R. Dietderich, A. Godeke, S. A. Gourlay, M. Marchevsky, S. O. Prestemon, and G. L. Sabbi. Performance correlation between $yba_2cu_3o_7 - \delta$ coils and short samples for coil technology development. *Superconductor Science and Technology*, 29, 4 2016.

[193] T. L. Bergam, A. S. Lavine, F. P. Incropera, and D. P. Dewitt. *Introduction to heat transfer*. John Wiley and Sons, Inc., 2001.

[194] K. Ilin, K. A. Yagotintsev, C. Zhou, P. Gao, J. Kosse, S. J. Otten, W. A.J. Wessel, T. J. Haugan, D. C. Van Der Laan, and A. Nijhuis. Experiments and fe modeling of stress-strain state in rebco tape under tensile, torsional and transverse load. *Superconductor Science and Technology*, 28, 5 2015.

[195] Marco Casali, Marco Breschi, and Pier Luigi Ribani. Two-dimensional anisotropic model of ybco coated conductors. *IEEE Transactions on Applied Superconductivity*, 25, 2 2015.

[196] Alberto Tenconi Andrea Cavagnino Francesco Laviano Silvio Vaschetto Eng Marco Biasion and Giacomo AY Galantini. Politecnico di torino preliminary design and simulation of a superconducting synchronous machine for aircraft applications, 2021.

[197] Yufan Yan, Timing Qu, and Francesco Grilli. Numerical modeling of ac loss in hts coated conductors and roebel cable using t-a formulation and comparison with h formulation. *IEEE Access*, 9:49649–49659, 2021.

[198] Mark Ainslie, Francesco Grilli, Loïc Quéval, Enric Pardo, Fernando Perez-Mendez, Ratu Mataira, Antonio Morandi, Asef Ghabeli, Chris Bumby, and Roberto Brambilla. A new benchmark problem for electromagnetic modelling of superconductors: The high-t csuperconducting dynamo. *Superconductor Science and Technology*, 33, 10 2020.

[199] Edgar Berrospe-Juarez, Víctor M.R. Zermeño, Frederic Trillaud, and Francesco Grilli. Real-time simulation of large-scale hts systems: Multi-scale and homogeneous models using the t-a formulation. *Superconductor Science and Technology*, 32, 4 2019.

[200] W. T. Norris. Calculation of hysteresis losses in hard super-conductors carrying ac: isolated conductors and edges of thin sheets. *Journal of Physics D: Applied Physics*, 489, 1970.

[201] Lorenzo Bortot, Bernhard Auchmann, Idoia Cortes Garcia, Herbert De Gersem, Michal MacIejewski, Matthias Mentink, Sebastian Schops, Jeroen Van Nugteren, and Arjan P. Verweij. A coupled a-h formulation for magneto-thermal transients in high-temperature superconducting magnets. *IEEE Transactions on Applied Superconductivity*, 30, 8 2020.

[202] J. Stern, J. Swanson, T. Bogdanof, M. Krutulis, J. Weiss, D. Van Der Laan, X. Wang, and L. Chiesa. Developing a vacuum pressure impregnation procedure for corc wires. *IEEE Transactions on Applied Superconductivity*, 32, 9 2022.

[203] Comsol multiphysics reference manual, 1998.

Appendix A

Implementation in COMSOL

This appendix is devoted to the explanation of the implementation of the proposed $T-A$ model in COMSOL Multiphysics® [203]. The 2-tapes CORC® geometry is considered for the description for sake of simplicity. The software has a built-in physics for the A-formulation, so called *Magnetic Fields* module, while the equations of the T-formulation need to be self-implemented through the *General Form Boundary PDE* module. The *Heat Transfer in Shells* is also a built-in physics in COMSOL. The model is intended to full a 3D, due to the intrinsic three-dimensionality of CORC® geometry, and non- stationary, to help the convergence of the simulation. The CORC® $(2, 6, 12$-tapes) is imported from a CAD generator while the air is built in COMSOL. The air domain should be large enough to zero the magnetic field at the end of the domain: usually, at least one order of magnitude larger then the characteristic length of the conductor domain is considered in literature. Note that, if we want to impose a transport current, the conductor domain should not fluctuate on the air (that can be the case if just an external magnetic field is applied), but the edges needs to intersect the air domain, see Fig. A.1. Then the A is solved for the all domain, and the T and the temperature θ for the conducting domain. For the implementation of the T-formulation, we open from *Physics* $\rightarrow$ *General Form Boundary PDE*. The dependent variable, called u in this module, has the dimension of a magnetic field A/m, see Section 3.1.4, while the source term is expressed in V/m^2, see Fig. A.2. The elements for this physics are linear. Under the tab *Component* $\rightarrow$ *Definition*, a new *Variable* tab is open, where the equation reported in Section 3.1.4 are implemented, see Fig. A.3. The variable uT is the tangential gradient of the vector $\mathbf{T}$, while n are the normal to the tape surface. x, y and z indicates

(a) (b)

Fig. A.1 COMSOL geometry for a 2-tapes CORC® uses as sample for model implementation. (a) Cross section, (b) view in perspective.

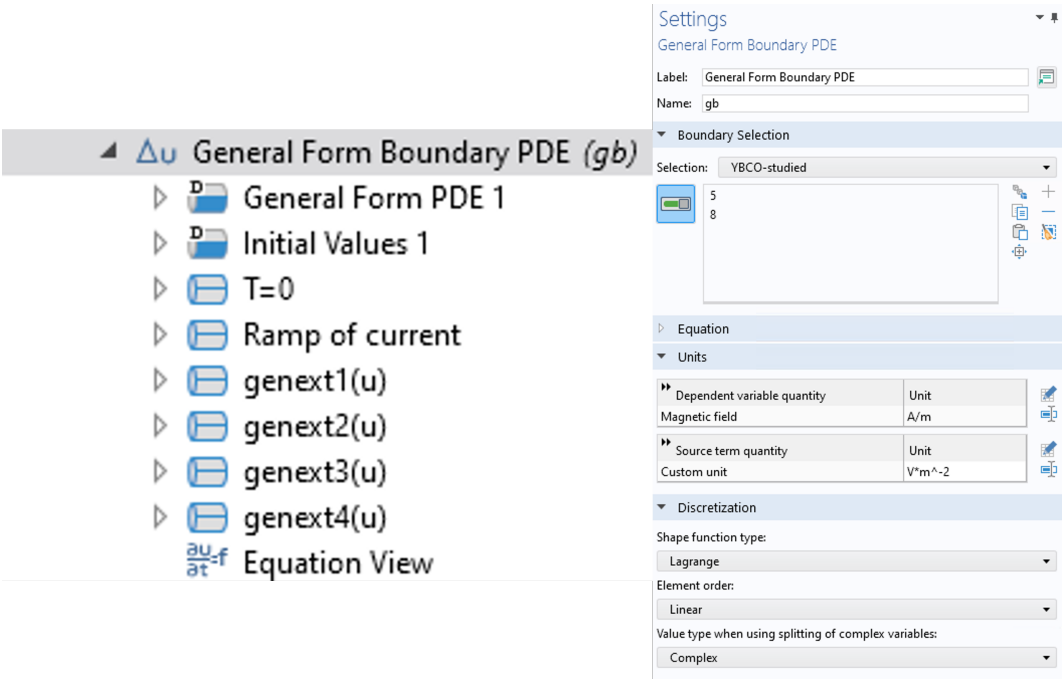

Fig. A.2 *General Form Boundary PDE* module and its settings.

Name	Expression	Unit	Description
Jx	uTy*nz-uTz*ny	A/m²	Current density, x component
Jy	-uTx*nz+uTz*nx	A/m²	Current density, y component
Jz	uTx*ny-uTy*nx	A/m²	Current density, z component
condeq	(1/rhoelcopper(T)*Acopper+1/rhoelsilver(T)*Asilver+1/rhoelsc*AcrossSC+1/rhoelhastelloy(T)*Ahastelloy)/Acrosstot	S/m	Equivalent electrical conductivity
Ex	1/condeq*Jx	V/m	Electric field, x component
Ey	1/condeq*Jy	V/m	Electric field, y component
Ez	1/condeq*Jz	V/m	Electric field, z component
Jnorm	sqrt(Jx^2+Jy^2+Jz^2+eps)	A/m²	norm of J
Enorm	sqrt(Ex^2+Ey^2+Ez^2+eps)	V/m	norm of E
Jcrit	phi_s*Jc0*Jct(T)*Jcb(Bpar,Bver)	A/m²	Critical current density
rhoelsc	rhoelSC(Jnorm,Jcrit)	Ω·m	SC electrical resistivity
Bver	abs(mf.Bx*nx+mf.By*ny+mf.Bz*nz+eps)	T	B perpendicular to the tape surface
Bpar	sqrt((abs(mf.By*nz-mf.Bz*ny))^2+(abs(mf.Bz*nx-mf.Bx*nz))^2+(abs(mf.Bx*ny-mf.By*nx))^2+eps)	T	B parallele to the tape surface
straintot	strain_x+strain_y+strain_w		Total strain map
phi_s	strain_deg(straintot)		Strain degradation

Fig. A.3 Implementation of T governing equations

the respective direction. All the components of J are computed as the curl of the T. The electric field E is calculated from Ohm's law (3.7). The critical current is temperature, magnetic field amplitude and strain dependent. The degradation due to the strain, instead, is first computed as described in Section 3.3.4, and extrapolated from Fig. 3.8 imported as table. Curvilinear coordinates have been adopted to respect the anisotropic properties, helical pattern of the twisting tapes and to proper compute the strain along the CORC® , see Fig. A.4. Once the total strain is computed from superposition principle, the ψ parameter is exported from the table. The temperature and the magnetic field dependence are considered through (3.33) and (3.30), which are implemented as analytical formulae. These variables are computed from the other two coupled physics. Once the J_c is computed, it is used for the analytical evaluation of the electrical resistivity of ReBCO through the power law. Then, the equivalent electrical conductivity is computed as stated in (3.41). The electrical resistivity of the others materials are temperature-dependent: these properties have been imported as tables. Note that, *eps* is added to some variables: *eps* is the machine precision number ($2.2204 \cdot 10^{-16}$), small enough to not influence the results, but different from zero. This stratagem avoids to have any division by zero, thus the onset of Not-a-Number (NaN), especially for initializing the problem. Then, the novel boundary condition is implemented for the imposition the current, allowing the re-distribution among tapes accordingly their temperature, magnetic field and strain conditions. In one edge the $T = 0$ and the total current is imposed in the last edge as $T = I_{tot}/thickness$, then the T is imposed equal and uniform among two subsequent edges (Fig. A.5). In order to do that, we utilized the *General Extrusion* feature in *Component* $\rightarrow$ *Definition* $\rightarrow$ *General Extrusion*.

The *General Extrusion* operator allows to map a variable from a *source* entity to a *destination* one and allowing operations such as translating, rotating, mirroring or scaling the mapped variables. In this case, the variable of interest is the current vector potential T and we want to force them to be the same via a rotation.

To map the T from the red edge in Fig. A.5 to the blue one:

$$genext1 = \begin{cases} x = x\cos(\alpha) - y\sin(\alpha) \\ y = x\sin(\alpha) + y\cos(\alpha) \end{cases} \tag{A.1}$$

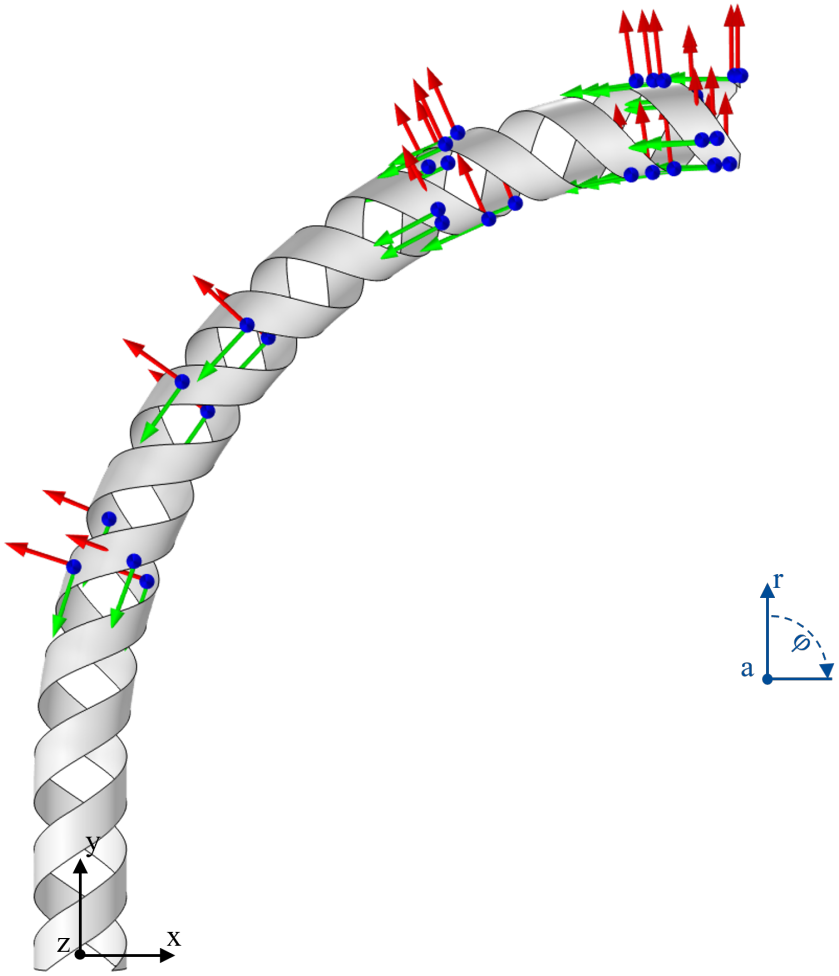

Fig. A.4 Representation of curvilinear coordinates for the evaluation of strain on the tape surface along the CORC® geometry. The references cartesian coordinates are skecthed in black, while the cylindrical system for the analytical computation of the strain is reported in dark blue.

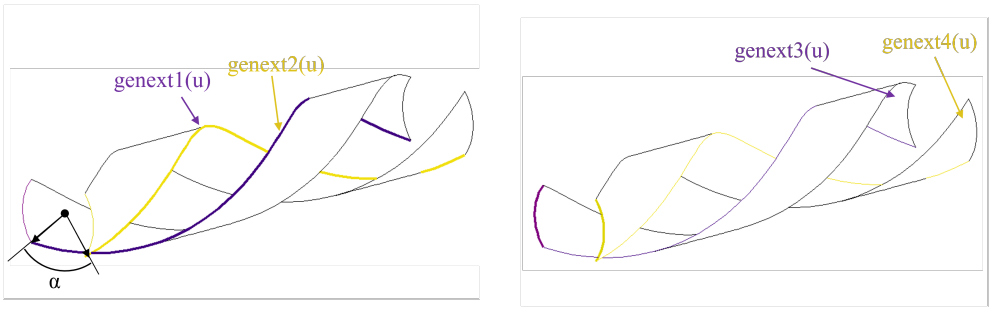

(a) (b)

Fig. A.5 (a)Representation of the novel boundary condition application in COMSOL. (b) Periodic boundary conditions for *General Form Boundary PDE*.

Where α is the angle between the two edges. To map the T from the blue edge to the red one, the angle has to be considered in the opposite direction as in (A.2).

$$genext2 = \begin{cases} x = x\cos(-\alpha) - y\sin(-\alpha) \\ y = x\sin(-\alpha) + y\cos(-\alpha) \end{cases} \tag{A.2}$$

Then, the mapped T, express as $genext1(u)$ (where u is the name of variable in COMSOL), is imposed to the blue edge as a Dirichlet boundary condition, and viceversa for $genext2(u)$. If a triangular unstructured is used for mesh the domain, select in the *Mesh search method* $\rightarrow$ *Closest point*. Moreover, in *Constraints settings* in *Applied reaction terms on:* the *All physics (symmetric)* is used.The same method has been applied for the imposition of the periodic boundary conditions (PBC), see Fig. A.5. To imposed PBC, just one edge needs to be mapped in *General Extrusion* and then applied to the corresponding edge as Dirichlet boundary condition. Since the geometry is twisting the mapping is simply:

$$genext(3-4) = \begin{cases} x = x \\ y = y \end{cases} \tag{A.3}$$

The *Magnetic Fields* physics has an easier implementation. The element order is keep as quadratic elements, and it is solved for all the computational domain (air + CORC®). The air properties are built-in in COMSOL. The driver parameter is the current density computed in *General Form Boundary PDE*. This is imposed through the so-called *Surface Current* boundary condition on the conducting domain: the

Fig. A.6 Imposition of *Surface Current* boundary condition in *Magnetic Fields*.

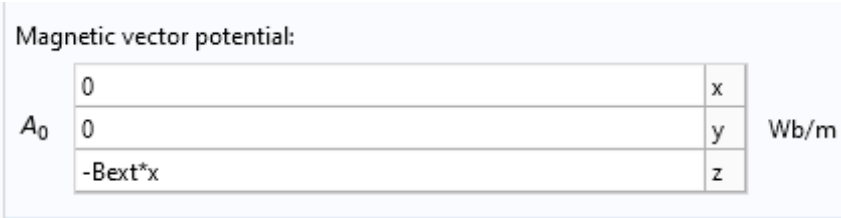

Fig. A.7 Example of imposition of *Magnetic Potential* boundary condition in *Magnetic Fields*. To imposed a magnetic field along the y-direction, the corresponding $A_z = -\frac{dB_x}{dz}$.

components of J are scaled at the tape thickness, Fig. A.6. If we want to imposed a magnetic field, there are two methods:

- directly impose a magnetic field A/m with a *Magnetic field* boundary condition;
- directly impose a the magnetic potential Wb/m with a *Magnetic potential* boundary condition computed from (3.9);

The second method is the one applied here: imposing the dependent variable A, rather than the magnetic field H, makes the solution easier and faster to compute. Finally, the heat transfer module is again built-in physics in the software. All the properties of interest are computed in *Components* $\rightarrow$ *Definition* $\rightarrow$ *Variable*. The thermophysical properties are computed as stated in Section 3.3.1, while the equation for the Nusselt Number and the heat transfer coefficient in Section 3.3.3, see Fig. A.8. The thermal conductivity is anisotropic along the axial and transversal direction of the tape surface. All boundaries are adiabatic. The heat deposited is imposed through the *Heat Source* setting in W/m^3. The cooling can be imposed as a negative heat sink or through *Heat Flux, Interface* setting selecting a *Convective Heat Flux* type, in which the heat transfer coefficient and the coolant temperature need to be defined. When all the physics is implemented, the mesh has to be built. For short cable twist

Name	Expression	Unit	Description
ktot	(kcopper(T)*Acopper+ksilver(T)*Asilver+khastelloy(T)*Ah...	W/(m·K)	Equivalent axial thermal conductivity
rhotot	(rhocu*Acopper+rhosilver*Asilver+rhohastelloy*Ahastello...	kg/m^3	Equivalent density
cptot	(cpcopper(T)*rhocu*Acopper*1[m]+cpsilver(T)*rhosilver*...	J/(kg·K)	Equivalent specific heat
ktras	1/((1/kcopper(T)*Acopper+1/ksilver(T)*Asilver+1/khastell...	W/(m·K)	Equivalent transversal thermal conductivity
Power	Jx*Ex+Jy*Ey+Jz*Ez	W/m^3	Power generated
cooling	-HTC*abs(T-T0)*Astape/Vtape/2	W/m^3	Cooling power
HTC	kln*Nu/Lc	W/(m^2·K)	Heat transfer coefficient
Nu	(0.6+(0.387*Ra(T)^(1/6))/(1+(0.559/Pr)^(9/16))^(8/27))^2		Nusselt number

Fig. A.8 *Heat Transfer in Shells* module and its settings.

pitches, it's not possible to use sweeping methods. Typically, unstructured triangular mesh is used of the SC surface domain and unstructured tetrahedral mesh for the volumetric air domain. The size of the mesh needs to be refined enough to guarantee accurate results and affordable time computational. Note that, since in *Magnetic Field* the PBC are already implemented, the source face has to be meshed first, and then copy (through the setting *Copy mesh*) to the destination face. Consider to reduce the size of the mesh when multiple layers are simulated, to reduce the aspect ratio of the air elements among two layers. The problem is fully coupled and all the settings parameters are kept as default. To help the initialization of the problem, in *Solution* $1 \rightarrow$ *Fully Coupled* $1 \rightarrow$ *Time-Dependent Solver* $1 \rightarrow$ *Time Stepping* the initial step is set at a very small number (order of magnitude of 10^{-10}), and the maximum time step *dt* is fixed at the chosen *dt*. Then, modified the relative tolerance according the desired accuracy of the output (10^{-4} is typically a good tolerance).

List of Figures

List of Tables